ΠΑΝΕΠΙΣΤΗΜΙΟ ΙΩΑΝΝΙΝΩΝ

ΤΜΗΜΑ ΦΥΣΙΚΗΣ

ΜΕΤΑΠΤΥΧΙΑΚΗ ΕΡΓΑΣΙΑ

Μπέτσου Χρυσούλα

Μελέτη της αντίδρασης $^{6}Li + p \rightarrow {}^{3}He + {}^{4}He$ με το τηλεσκόπιο DINEX

Ιωάννινα, 2015

Περίληψη

Η εργασία αυτή αναφέρεται στην μελέτη της αντίδρασης ^{6}Li + p → ^{3}He + ^{4}He με το τηλεσκόπιο DINEX σε αντίστροφη κινηματική, σε ενέργειες κοντά στο φράγμα Coulomb και συγκεκριμένα στις ενέργειες 2.7 ,3.3, 4.2 και 4.8 MeV/u. Το πειραματικό μέρος της μελέτης πραγματοποιήθηκε στο Instituto Nazionali di Fisica Nucleare Laboratori Nazionali del Sud in Catania (INFN-LNS) στην Ιταλία. Δέσμες ιόντων ^{6}Li αφού είχαν επιταχυνθεί στις παραπάνω ενέργειες, προσέκρουσαν σε στόχο CH_2 πάχους περίπου 300 μg/cm^2. Τα προϊόντα της αντίδρασης ανιχνεύτηκαν από ένα τηλεσκόπιο του ανιχνευτικού συστήματος DINEX τοποθετημένου σε απόσταση 15.5 cm από τον στόχο, καλύπτοντας ένα εύρος γωνιών από θ_{lab} =16˚ μέχρι 34˚. Το τηλεσκόπιο αποτελούνταν από έναν ανιχνευτή ΔΕ και δύο ανιχνευτές Ε. Ο ΔΕ ανιχνευτής είναι ένας μικρολωριδιακός ανιχνευτής διπλής όψης (DSSSD), πάχους 48μm και διαστάσεων 5x5 cm με 16 οριζόντια και 16 κάθετες λωρίδες (strip). Οι ανιχνευτές Ε είναι ανιχνευτές πυριτίου πάχους 530 μm. Ο ΔΕ ανιχνευτής απορρόφησε ένα μέρος της ενέργειας των προϊόντων της αντίδρασης που τελικά σταμάτησαν στον της τεχνικής ΔΕ-Ε.

Η ανάλυση των φασμάτων του ανιχνευτή Ε επέτρεψε την ταυτοποίησή των προϊόντων μέσω πραγματοποιήθηκε μέσω του κώδικα PAW. Με βάση την κινηματική των αντιδράσεων από το Nuclear Reaction Video Project (NRV) και την απώλεια ενέργειας των ιόντων μέσα στους ανιχνευτές από το πρόγραμμα Lise++, ταυτοποιήθηκαν τα προϊόντα που προέκυψαν από την αντίδραση.

Η ενεργειακή βαθμονόμηση των ΔΕ και Ε ανιχνευτών πραγματοποιήθηκε μέσω των μετρήσεων της ελαστικής σκέδασης των ιόντων του ^{6}Li σε φύλλα χρυσού πάχους 180 μg/cm^2 και σε φύλλα άνθρακα πάχους 240 μg/cm^2 σε ενέργειες των 25 και 29 MeV. Η στερεά γωνία για κάθε strip προσδιορίστηκε μέσω των μετρήσεων ελαστικής σκέδασης του ^{6}Li σε φύλλα χρυσού πάχους 180 μg/cm^2 σε ενέργεια 25 MeV , μία από τις χαμηλότερες ενέργειες όπου η σκέδαση μπορεί να θεωρηθεί ως Rutherford. Η ροή της δέσμης καταγράφηκε στο Faraday cup και η ακρίβεια της έντασης της επιβεβαιώθηκε μέσω της σκέδασης Rutherford του ^{6}Li στο υδρογόνο, όπως καταγράφηκε από το φασματόμετρο MAGNEX.

Οι διαφορικές ενεργές διατομές των ^{3}He και ^{4}He υπολογίστηκαν και για τις 4 ενέργειες στο γωνιακό εύρος από θ_{lab} =16˚ μέχρι 34˚. Τόσο το ^{3}He όσο και το ^{4}He ταυτοποιήθηκαν επαρκώς μέσω της τεχνικής ΔΕ-Ε. Το ^{4}He δεν διακρίνονταν καθαρά στο φάσμα, καθώς βρίσκονταν πάνω σε ένα συνεχές υπόβαθρο από σωμάτια άλφα, προερχόμενα από αντιδράσεις διάσπασης με το υδρογόνο και τον άνθρακα, αλλά και από αντιδράσεις σύντηξης με τον άνθρακα. Για αυτό τον λόγο, το υπόβαθρο έπρεπε να αφαιρεθεί, αυξάνοντας έτσι την σχετική αβεβαιότητα στον υπολογισμό των διαφορικών ενεργών διατομών του ^{4}He. Από την άλλη μεριά, το ^{3}He διακρίνονταν καθαρά στο φάσμα χωρίς να χρειάζεται να αφαιρεθεί κάποιο υπόβαθρο και έτσι η αβεβαιότητα στον υπολογισμό των διαφορικών ενεργών διατομών του ήταν μικρή.

Οι διαφορικές ενεργές διατομές συγκρίθηκαν με αποτελέσματα προηγούμενων μετρήσεων καθώς και με θεωρητικούς υπολογισμούς. Στην ενέργεια των 16 MeV, η ασυμφωνία μεταξύ

των δύο προηγούμενων μετρήσεων (Lin et al., Elwyn et al.) αποκαταστάθηκε εν μέρει με τα τωρινά αποτελέσματα. Η καλή συμφωνία των δεδομένων με την θεωρία οδήγησε σε χρήσιμα συμπεράσματα για τον μηχανισμό της αντίδρασης. Επιπλέον, οι διαφορικές ενεργές διατομές αναλύθηκαν σε ένα άθροισμα πολυωνύμων Legendre $\sum_{l=0}^{l} B_l P_l\left(\cos(\theta)\right)$ και υπολογίστηκαν οι ενεργές διατομές της αντίδρασης μέσω του τύπου $\sigma = 4\pi B_0$,όπου B_0 είναι η σταθερά μηδενικής τάξης Legendre. Τελικά, οι ενεργές διατομές της αντίδρασης ως συνάρτηση της ενέργειας συγκρίθηκαν με προηγούμενα αποτελέσματα όπου αποκαταστάθηκαν κάποιες ασυμφωνίες ενώ αποκαλύφθηκε ένας πιθανός συντονισμός σε ενέργεια Ep=3.7 MeV.

UNIVERSITY OF IOANNINA

PHYSICS DEPARTMENT

MSc Thesis

Betsou Chrysoula

Study of the reaction $^{6}Li + p \rightarrow {}^{3}He + {}^{4}He$ with DINEX telescope

Ioannina, 2015

Acknowledgements

I would like to thank all of those who have supported and assisted me during my graduate studies.

First of all, I would like to express my deepest gratitude to my professor, Professor Athena Pakou, for her support during my studies, for her guidance and patience, for suggesting the subject and for introducing me to the world of experimental nuclear physics.

In addition, I would like to thank all the members of the review committee for their useful and enlightening advices: the supervisor Associate Professor X. Aslanoglou, the Associate Professor E. Stiliaris and the Assistant Professor N. Nicolis.

I would like to extend my warm thanks to the head of the MAGNEX group Professor F. Cappuzzello and his group for their efforts running the experiment and for his generous hospitality during our stay in Catania, as well as Professor I. Martel and his group from the Huelva University for running the experiment and making available the DINEX telescope.

Moreover, I would like to thank Professor K. Rusek, Associate Professor N. Keeley and the Assistant Professor N. Nicolis for the theoretical support.

I warmly thank the PhD candidate Vasilis Soukeras and the PhD candidate Onoufrios Sgouros for their support and advices for this thesis.

Last but not least, I would like to thank my parents and my sister for their love and their support during my studies.

Contents

Extended Summary

This master thesis refers to the study of the reaction $^{6}Li + p \rightarrow {}^{3}He + {}^{4}He$ with the DINEX telescope in inverse kinematics at near barrier energies, namely 2.7, 3.3, 4.2 and 4.8 MeV/u. The experiment was performed at Instituto Nazionali di Fisica Nucleare Laboratori Nazionali del Sud in Catania (INFN-LNS), Italy. Beams of ^{6}Li were accelerated at the above energies and impinged on a ~ 300 μg/cm^2 CH_2 target. The reaction products were recorded with one telescope of the DINEX array and an angular distribution was performed. The telescope was set at a distance of 15.5 cm far from the target, allocating an angular range of θ_{lab} =16˚ to 34˚. The DINEX telescope was consisted of one ΔE detector and two E detectors. The ΔE stage of the telescope was a DSSSD silicon detector, 48 μm thick, with an active area of 5x5 cm and 16 vertical and 16 horizontal strips. The E stage was a silicon pad detector, 530 μm thick. The ΔE stage of the telescope absorbed a part of the recoil ion energy, allowing a Z separation via the ΔE - E technique.

The data analysis was performed at Ioannina using the program PAW, while the identification of the peaks was performed taking into account the kinematical prediction from the Nuclear Reaction Video Project (NRV) and the energy losses from the Lise++ program.

For the energy calibration of ΔE and E detectors the elastic scattering measurements performed with a gold foil 180 μg/cm^2 thick and with a carbon foil 240 μg/cm^2 thick, at bombarding energies 29 MeV and 25 MeV. The solid angle for each strip was determined with an elastic scattering measurement performed with a gold foil 180 μg/cm^2 thick at one of the lower energies, namely 25 MeV, where the scattering could be considered as pure Rutherford. The flux of the beam was recorded in the Faraday cup and the accuracy of the flux intensity measurement was confirmed via the Rutherford scattering of ^{6}Li on hydrogen, recorded in MAGNEX.

Angular distribution measurements were performed at the 4 energies by detecting both reaction products ^{3}He and ^{4}He in the laboratory angles θ_{lab} =16˚ to 34˚, which correspond to a wide angular range in the center of mass frame ($\theta_{c.m.}$~ 40˚ to 140˚). The ^{3}He and ^{4}He were well resolved via the ΔE - E technique. The ^{4}He peak was sitting on the top of a continuous background originating from breakup processes on hydrogen and carbon as well as from fusion reactions on carbon. This background had to be subtracted increasing the associated uncertainty to the ^{4}He cross sections. On the other hand ^{3}He was clearly distinguished, no background was subtracted and the uncertainty to these cross sections was kept low. The so obtained differential cross sections were compared with previous measurements and with theoretical calculations. Previous inconsistencies at 16 MeV presented between the previous data sets were partly clarified with the present results, while a good consistency of data and theory gave ground to useful conclusions for the reaction mechanism. Finally, the differential cross sections were fitted to a sum of Legendre polynomials $\sum_{l=0}^{l} B_l P_l\left(\cos(\theta)\right)$ and total reaction cross sections were estimated at the above energies according to the formula

$\sigma = 4\pi B_0$, where B_0 is the zero order Legendre coefficient. Subsequently the results were compared with some sets of previous excitation function measurements. The new results disclose previous inconsistencies and predict a possible new resonance at Ep=3.7 MeV

Introduction

This work is part of the curriculum of the Postgraduate Program of the Department of Physics, University of Ioannina. The research area belongs to the basic direction of Nuclear Physics and particularly in the area of Nuclear Reactions with consequences in the area of Nuclear Astrophysics.

In this work, the angular distribution of the p(^{6}Li, ^{3}He)^{4}He reaction has been studied at energies 2.7, 3.3, 4.2 and 4.8 MeV/u. The significance of the ^{6}Li(p, ^{3}He)^{4}He reaction has been demonstrated for a long time in several experimental studies in relation with controlled thermonuclear reactors based on the use of advanced ion fuels [1-11]. Also, this reaction is used in fundamental astrophysical problems like the understanding of the Bing Bang nucleosynthesis, and "lithium depletion" either in the sun or in other galactic stars [12-15].

Total cross sections and angular distributions of the reaction, as well as the values of the "astrophysical S-function", have been measured at the energy range E_p=0.1-0.7 MeV by T. Shinozuka et al. [16] and by J. U. Kwon et al. [17]. Chia- Shiou Lin et al. [18] have measured the excitation curve and the angular distribution of the reaction at proton energies from 1.0 to 2.6 MeV. For the measurements, they have used a coincidence method between the two reaction products ^{3}He and ^{4}He in order to obtain clear spectra without backgrounds. In addition, at this energy range, angular distribution measurements have been performed by J. B. Marion et al. [19], and by A.J. Elwyn et al. [20] who have also calculated the reaction's total cross section, thermonuclear reaction rate parameters and astrophysical S factors. J. P. Johnston et al. [21], as well as A. Tumino et al. [15,22] have studied this reaction and they have carried out angular distribution measurements at proton energies from 2 MeV down to astrophysical energies. Temmer [23] and S. N. Abramovich et al. [24] have performed measurements of reaction cross section at the energy range from 2.0 to 5.0 MeV/u. Moreover, J. M. F. Jeronymo et al. [25] has studied the excitation curve and the angular distributions of the reaction at the same energy range as above. U. Fasoli et al. [26] have studied angular distribution curves taken between 3.0 and 5.6 MeV/u but the differential cross sections, which have been also fitted to a series of polynomial Legendre, have been expressed in arbitrary units. Furthermore, C. B. Gould et al. [27] have calculated the absolute cross sections at the energy range from 3 to 12 MeV, while at bigger proton energies, measurements of the reaction's differential cross sections have been performed by K. Schenk et al. [28] and by Michael F. Werby et al. [29].

The ^{6}Li(p, ^{3}He)^{4}He reaction is studied in this work as a complementary part of The LIPMAGNEX experiment which includes recent measurements of elastic scattering and breakup modes [30-31] with the MAGNEX spectrometer [32-34] in inverse kinematics. These measurements with the MAGNEX spectrometer are part of the research program of the group of the Nuclear Physics Laboratory (NPL) which is relative to the optical potential and various reaction channels of weakly bound nuclei at near-barrier energies and the consequences on coupling effects. In this respect, the present results will be used in future work on a global understanding of the optical potential and relevant reaction mechanisms.

Also, due to the fact that the previous measurements didn't agree so well and several inconsistencies occurred, these data serve to clarify the experimental situation at these energies [18-21,23-28]. The experimental data were collected in the Instituto Nazionali di Fisica Nucleare- Laboratori Nazionali del Sud in Catania (INFN-LNS), Italy and the analysis of the data was performed at the NPL- Ioannina. The results are discussed in the present work which includes the following chapters:

- Chapter 1: It includes a brief description of the theory for direct and compound mechanism reactions as well as for Rutherford scattering. It also includes, briefly, how the Coulomb barrier is calculated and some elements for semiconductors and finally Double Sided Silicon Strip Detectors (DSSSD) and DINEX telescope used in this work.

- Chapter 2: It includes a description of the experimental setup, the energy calibration and the determination of solid angle of the used telescope.

- Chapter 3: It includes the data reduction and particularly the determination of the angular distribution and the reaction cross section.

- Chapter 4: It includes the Summary with the conclusions of this study.

This work also contains an appendix with:

- the error calculation of solid angle

- the error calculation of differential cross section

- a program for the calculation of the Coulomb barrier

- a program for the conversion of the differential cross section from the laboratory system to the center of mass frame

- Tables related to the energy calibration of the detectors and to the differential cross section.

1. Theory

1.1 Introduction to Nuclear Reactions

A nuclear reaction is the result of the bombarding of a nucleus- target (stationary) with a beam of nucleus-projectile, such as charged particles (p, alpha particles or heavier nuclei), photons or n, which have a particular kinetic energy. In order for the reaction to take place, the projectile and the target need to approach each other at distances of the order of the nuclear dimensions (10^{-15} m), since the nuclear force reaches only a distance of 10^{-15}m. The energy must be high enough to overcome the electromagnetic repulsion between the protons. This energy "barrier" is called the Coulomb barrier and it is analyzed below in chapter 1.6. This collision between the two nuclei can cause the scattering of the projectile, the absorption of the projectile or a change in the nuclear composition and/or the energy state of the interacting nuclei. The products of the nuclear reaction can be either in their ground state or in an excited state. A typical nuclear reaction can be written as:

$\alpha + X \rightarrow Y + b + Q$ or $X(\alpha,b)Y$

where α is the accelerated projectile, X is the target nucleus, and Y, b are the reaction products while Q is the released or absorbed energy during the reaction. Usually, Y is a heavy product that stops in the target and is not directly observed, while b is a light particle that can be detected and measured. If Q>0 (the total mass of the products is less than the mass of the projectile and the target), then the reaction is called exothermic (energy releases), while if Q<0 (the total mass of the products is greater than the mass of the projectile and the target) the reaction is called endothermic (energy is absorbed).

Two nuclei can interact between each other with the processes described below:

- the **elastic scattering process**, where the outgoing particles are the same with the incident particles (where X=Y and α=b and Q=0) and they are in their ground states, such as

$n + {}^{208}Pb \rightarrow n + {}^{208}Pb$

- the **inelastic scattering process**, where the outgoing particles are the same with the incident particles (where $Y=X^*$ or/and $b=\alpha^*$ and Q≠0) and the Y or/and b are in excited states (from which they will decay by γ emission) , such as

${}^{12}C + {}^{208}Pb \rightarrow {}^{12}C^* + {}^{208}Pb^*$

Elastic and inelastic scattering processes can be initiated either due to Coulomb or due to strong interactions.

- the **nuclear reactions**, where $A + a \rightarrow B + b$ with Q≠0. The nuclear reactions are characterized by the strong interaction, which is responsible for the nuclear force. The nuclear reactions can be distinguished into the following categories, based on the mechanism that governs the process itself:

- **the direct reactions**, where we have interchange of few nucleons between target and projectile due to their interaction with the potential (nuclear or Coulomb) of the nucleus-target and the whole process of the interaction lasts about 10^{-22} sec.

- **the compound nucleus mechanisms**, where the projectile is absorbed by the target, creating temporarily a compound nucleus, which is in an excited state and which finally decays with the evaporation of particles The whole process lasts more than the direct reactions (10^{-16}sec). The compound nucleus "forgets" the form of it's production.

- **the resonance reactions**, which are between the direct reactions and the compound nucleus mechanisms, where the incoming particles forms a 'quasi-bound' state before the outgoing particle is ejected. [35-39,42]

1.2 The Q value of a reaction

The Q value is the available energy for a reaction to take place. It is the subtraction of the ground state masses of the exit channel from the masses of the entrance channel. It is written according to the equation (1.1):

$$Q = \left(m_a + m_X - m_b - m_Y\right)c^2 \qquad (1.1)$$

or it can be written as the difference between the final kinetic energy and the initial kinetic energy:

$$Q = T_{final} - T_{initial} = T_b + T_Y - T_a - T_X \qquad (1.2)$$

If Q>0 then the reaction is called exothermic and energy is released as kinetic energy of the reaction products, while if Q<0 then the reaction is called endothermic and energy is absorbed (the initial kinetic energy is converted into nuclear mass or binding energy). [35,39,42]

1.3 Rutherford Scattering

From the scattering theory we will refer to Rutherford scattering which is pertinent to this work.

When the projectile approaches the target nucleus, in a nuclear reaction, a repulsive Coulomb force acts between them, as both the projectile and the target are positive charged. When only the Coulomb force is active, then we have the Rutherford scattering. If there is no interaction between them, the projectile would traverse a straight path which would have a distance b from the nucleus target. This distance between the projectile's path and the target nucleus is

called the *impact parameter* b. However, the projectile follows an hyperbolic path due to the repulsive Coulomb force and r is the minimum distance that it can approach from the target.

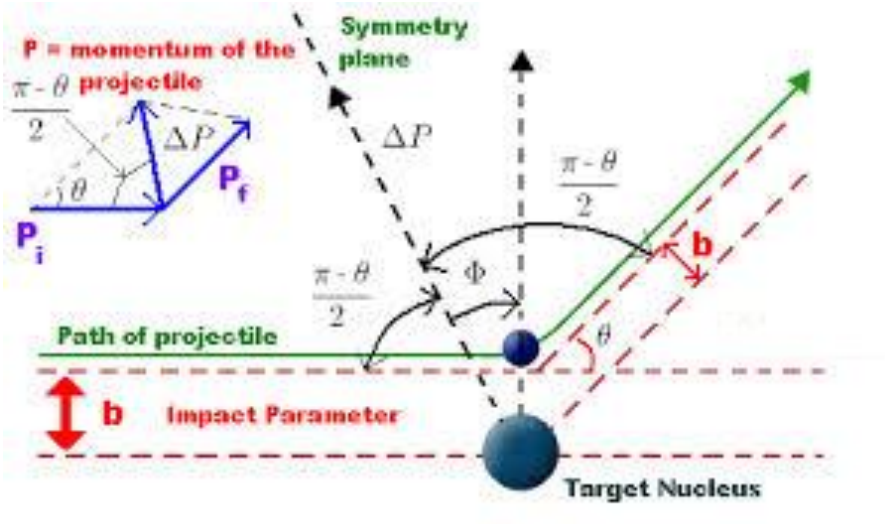

FIG. 1.1: The Rutherford scattering of the positive charged projectile from the positive charged target.

As it can be seen in Figure 1.1, θ is the scattering angle of the projectile.

The momentum of the projectile changes from $\mathbf{p_1}$ to $\mathbf{p_2}$ due to the impulse $\int \mathbf{F}\,dt$ by the target:

$$\Delta\mathbf{p} = \mathbf{p}_2 - p_1 = \int \mathbf{F}\,dt \qquad (1.3)$$

The target is considered stationary so the kinetic energy from the projectile is conserved, as well as its momentum:

$$p_1 = p_2 = mv \qquad (1.4)$$

where v is the velocity of the projectile. According to Figure 1.1, using the law of sins:

$$\frac{\Delta p}{\sin\theta} = \frac{mv}{\sin\frac{\pi-\theta}{2}} \qquad (1.5)$$

Since

$\sin\frac{1}{2}(\pi-\theta) = \cos\frac{\theta}{2}$ and $\sin\theta = 2\sin\frac{\theta}{2}\cos\frac{\theta}{2}$ the equation (1.5) will be:

$$\Delta p = 2mv\sin\frac{\theta}{2} \qquad (1.6)$$

The impulse can also be written as below, as it is in the same direction with the $\Delta\mathbf{p}$:

$$\left|\int F\ dt\ \right| = \int F\cos\varphi\ dt \qquad (1.7)$$

Then the equation (1.3) from the (1.6) and (1.7) is:

$$2mv\sin\frac{\theta}{2} = \int_{-\infty}^{+\infty} F\cos\varphi dt \Rightarrow 2mv\sin\frac{\theta}{2} = \int_{-(\pi-\theta)/2}^{+(\pi-\theta)/2} F\cos\varphi\frac{dt}{d\varphi}d\varphi \qquad (1.8)$$

It is known that the quantity $\frac{d\varphi}{dt}$ is the angular velocity of the projectile, and the angular momentum is conserved, so:

$$m\omega r^2 = const. = mr^2\frac{d\varphi}{dt} = mvb \Rightarrow \frac{dt}{d\varphi} = \frac{r^2}{vb} \qquad (1.9)$$

so the (1.8) equation is:

$$2mv^2 b\sin\frac{\theta}{2} = \int_{-(\pi-\theta)/2}^{+(\pi-\theta)/2} Fr^2\cos\varphi d\varphi \qquad (1.10)$$

Also, it is known that the only force which interacts between the projectile and the target is the Coulomb force: $F = \frac{1}{4\pi\varepsilon_o}\frac{Z_1Z_2e^2}{r^2}$ (1.11)

so the (1.10) equation results that:

$$2mv^2 b\sin\frac{\theta}{2} = \int_{-(\pi-\theta)/2}^{+(\pi-\theta)/2}\frac{1}{4\pi\varepsilon_o}\frac{Z_1Z_2e^2}{r^2}r^2\cos\varphi d\varphi \Rightarrow \frac{8\pi\varepsilon_o mv^2 b}{Z_1Z_2e^2}\sin\frac{\theta}{2} = \int_{-(\pi-\theta)/2}^{+(\pi-\theta)/2}\cos\varphi d\varphi \Rightarrow$$

$$\Rightarrow \frac{8\pi\varepsilon_o mv^2 b}{Z_1Z_2e^2}\sin\frac{\theta}{2} = 2\cos\frac{\theta}{2} \Rightarrow \tan\frac{\theta}{2} = \frac{2Z_1Z_2e^2}{8\pi\varepsilon_o mv^2 b} = \frac{Z_1Z_2e^2}{4\pi\varepsilon_o mv^2 b} \qquad (1.12)$$

The equation (1.12) for the *scattering angle*, can also be written as a function of the kinetic energy of the projectile:

$$\tan\frac{\theta}{2} = \frac{Z_1Z_2e^2}{8\pi\varepsilon_o Eb} \qquad (1.13)$$

However, at the closest approach r_o where the velocity of the projectile is v=0 as the projectile strikes directly the target (b=0), the conservation of the projectile's energy gives:

$$\frac{1}{2}mv^2 = \frac{1}{4\pi\varepsilon_o}\frac{Z_1Z_2e^2}{r_o} \Rightarrow r_o = \frac{Z_1Z_2e^2}{2\pi\varepsilon_o mv^2} = \frac{Z_1Z_2e^2}{4\pi\varepsilon_o E} \qquad (1.14)$$

where E is the beam energy, and thus the scattering angle equation (1.13) becomes:

$$\tan\frac{\theta}{2}=\frac{r_o}{2b} \qquad (1.15)$$

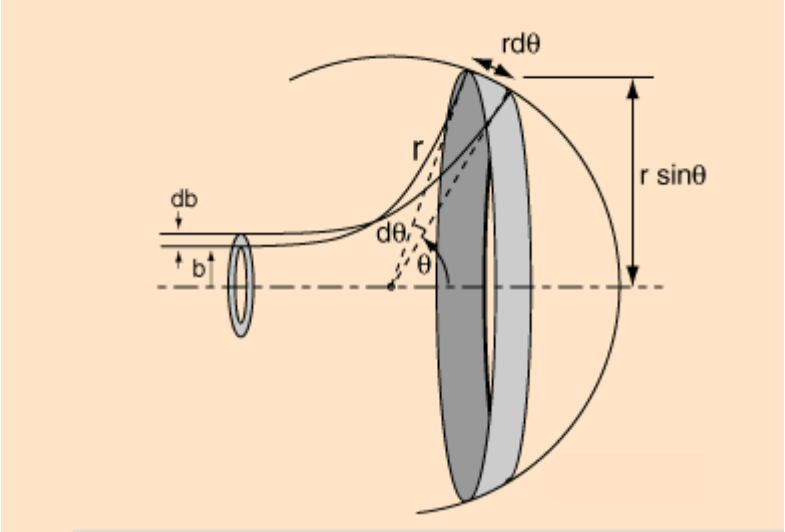

FIG. 1.2: Schematic representation of incident beam particles in the area dσ which are scattered into the solid angle dΩ.

Considering that I_o is the flux of the beam of the incident particles, then the flux which passes through the annulus with radii b and b+db (according to the Figure 1.2), is written as:

$$dI=2\pi I_o b\,db \qquad (1.16)$$

then if we differentiate the equation (1.15):

$$db=-\frac{r_o}{4\sin^2\left(\theta/2\right)}d\theta \qquad (1.17)$$

and combining the equations (1.16) and (1.17), we have:

$$dI=\frac{1}{4}\pi I_o r_o^2\frac{\cos\left(\frac{\theta}{2}\right)}{\sin^3\left(\frac{\theta}{2}\right)}d\Omega \qquad (1.18)$$

The flux is scattered into the area between θ and θ+dθ angles which corresponds to the solid angle $d\Omega=2\pi\sin\theta d\theta$, and finally the differential cross section for the Rutherford scattering is given from the formula (1.19):

$$\frac{d\sigma}{d\Omega}=\frac{1}{I_o}\frac{dI}{d\Omega}=\left(\frac{r_o}{4}\right)^2\frac{1}{\sin^4\left(\frac{\theta}{2}\right)}=\left(\frac{Z_1Z_2e^2}{2mv^2}\right)^2\frac{1}{\sin^4\left(\frac{\theta}{2}\right)}\Rightarrow$$

$$\frac{d\sigma}{d\Omega}=\left(\frac{Z_1Z_2e^2}{4E}\right)^2\frac{1}{\sin^4\left(\frac{\theta}{2}\right)} \qquad (1.19)$$

where E is the beam energy. [35,37,41,42]

1.4 Direct reactions

The direct reaction is a reaction where the nuclei are instantaneously in touch and immediately they separate. This means that, the duration of the direct reaction is the time which needs the incident particle after it has encountered the target nucleus to traverse the nuclear field (10^{-22} sec). It is a fast reaction mechanism and proceeds directly from the initial state to the final state without the forming of an intermediate compound state. There are different types of direct reactions such as the *elastic scattering*, the *inelastic scattering*, the *transfer reactions* (*stripping reaction* and *pick-up reaction*) and the *knockout reactions*.

The most simple direct reaction is performed in the *elastic scattering* where the incident particle and the target are elastically scattered, without loss of energy. The incident particle interacts with the target nucleus as a whole and the optical potential is used for the description of the interaction. The optical potential is written as:

$$U(r) = V(r) + iW(r) \qquad (1.20)$$

where the real part of the potential describes the elastic scattering of the incident projectile by the nucleus target ,while the imaginary part describes the absorption, which is the process that removes flux from the incident channel.

Another direct reaction is performed in the *inelastic scattering* where the projectile interacts with the target- nucleus, gives to it some of its energy and raises it to an excited state. In the most simple inelastic scattering, the projectile interacts with one single nucleon of the target-nucleus and drives it to a higher energy state. Also, in the inelastic scattering the projectile can interact with more than one nucleons of the target which are raised to excited states. These excited states usually have a collective character. [38]

Another type of direct reactions are the *nucleon transfer reactions*. In these reactions one or more nucleons or a cluster of nucleons can be transferred from the projectile to the target or from the target to the projectile. The transfer reactions are divided into the *stripping reactions* and into the *pick-up reactions*.

In the *stripping reactions* (Figure 1.3), the projectile loses one or more nucleons while it approaches the target and these nucleons are captured by the target. An example of a *stripping reaction* is a (d, p) process in which a deuteron indicates on the nucleus target. The deuteron is a stable particle and it is consisted of a proton and a neutron. After the indication of the deuteron on the target, the neutron is stripped from the deuteron and is captured by the target. In the exit channel the reaction products are the proton and the target-nucleus with one more neutron. Another stripping reaction is the ^{208}Pb(^{17}O,^{16}O)^{209}Pb. [39] A stripping reaction can be written according to the formula: $a + A \rightarrow B + b$, where $B = A + x$ and $b = a - x$ and x is one or more nucleons.

The *pick-up reactions* (Figure 1.4) are the opposite of the stripping reactions. While the projectile is getting closer to the target, the target loses one or more nucleons which are finally captured by the projectile. An example of a pick-up reaction is the ^{40}Ca(^{3}He,^{4}He)^{39}Ca. [36] One pick-up reaction can be written as: $a + A \rightarrow B + b$, where $B = A - x$ and $b = a + x$ and x is one or more nucleons.

The *knock-out reactions* (Figure 1.5) are another case of direct reactions. The projectile collides with the target and a nucleon or a group of nucleons from the target are ejected separately. The projectile remains unchanged, so in the final state of the reaction three particles are observed. One example of a knock-out reaction is the: ${}_{1}^{1}\mathrm{H} + {}_{7}^{15}\mathrm{N} \rightarrow {}_{1}^{1}\mathrm{H} + {}_{7}^{14}\mathrm{N} + \mathrm{n}$, where the final state has three particles. [35-39]

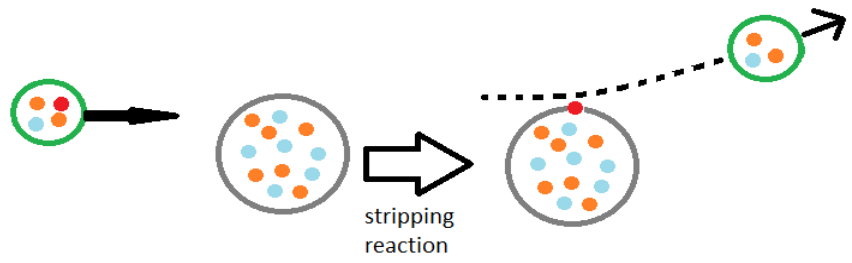

FIG. 1.3: Schematic view of a stripping reaction.

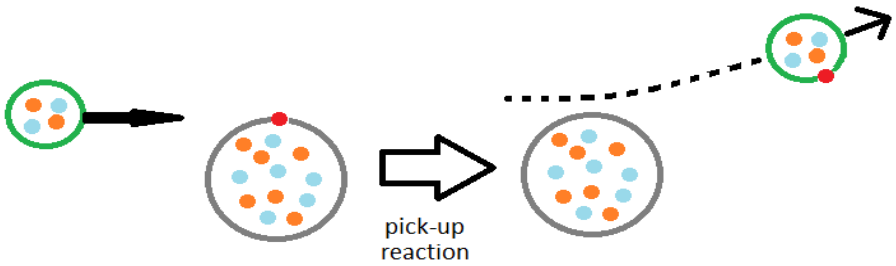

FIG. 1.4: Schematic view of a pick-up reaction.

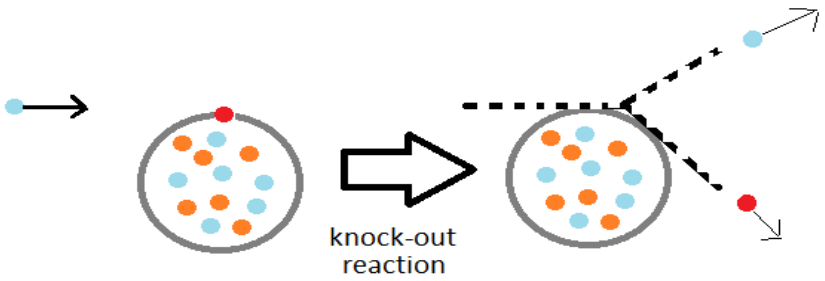

FIG. 1.5: Schematic view of a knock-out reaction.

1.5 Compound nucleus mechanism

In a compound nucleus mechanism, the projectile collides with the target nucleus, and during that collision, the nucleons from the projectile have enough time to interact with the nucleons from the target, by coming into contact many times. During that time, a compound nucleus is formed and it is excited. A nuclear compound mechanism can be written according to the formula:

$a + X \rightarrow C^{*} \rightarrow Y + b$

where a is the projectile, X is the nucleus target, C^{*} is the excited compound nucleus, Y and b are the reaction products. This compound nucleus stays united until the incident energy is shared among all the nucleons of which it is consisted. The compound nucleus lives long enough in order a statistical equilibrium to be achieved. As the interactions between the nucleons increase randomly, there is a statistical distribution in energies and the probability of the escape of one or more nucleons from the compound system increases, until, in fact, one or more nucleons escape (after it has gained enough energy), just like the molecules which evaporate from a hot liquid, and the residual nucleus reaches its ground state by gamma emission. Due to the many interactions between the nucleons, the identities of the original nucleus are lost, which means that the compound nucleus has forgotten the entrance channel from where it comes from and as a result it can decay in a variety of different channels. This memory loss of the formation process indicates that the decay of the compound nucleus is completely independent from its formation. This is known as the Bohr independence hypothesis. According to the independence hypothesis, for the determination of a compound nucleus the only things that are needed are its energy, its angular momentum and its parity, and not the way it is formed. [35-38] The verification of the independence hypothesis was tested by Ghoshal et al. (1950) who measured the cross sections of $^{63}Cu(p,n)^{63}Zn$ and $^{60}Ni(\alpha,n)^{63}Zn$ from 12-40 MeV and from 3-31 MeV respectively ,which lead to the compound nucleus ^{64}Zn. They found out that the cross sections coming from these different reactions have similar characteristics, which indeed verified that the way the compound nucleus decays does not depend on the mode of its formation.[35]

1.5.1 Cross section for a compound nucleus reaction

The compound nucleus may decay in several exit channels and due to the fact that its decay is independent from the way of its formation, the reaction cross section is calculated as below. If the cross section for forming the compound nucleus C coming from the incident channel a + X is σ_α, and the decay of the compound nucleus C to a particular exit channel β with reaction products Y + b is characterized by the relative probability W_β per unit time and the width $\Gamma_\beta = \hbar W_\beta$,then the reaction cross section is given according to the equation:

$$\sigma_{\beta\alpha} = \sigma_\alpha \frac{\Gamma_\beta}{\Gamma} \qquad (1.21)$$

where $\sigma_{\beta\alpha}$ is the reaction cross section from the entrance channel α to the exit channel β, Γ is the total width of the decay which means it is the sum of all the widths of the possible exit channels (α,β,γ,...):

$$\Gamma = \Gamma_\alpha + \Gamma_\beta + \Gamma_\gamma + ... \qquad (1.22)$$

and $\frac{\Gamma_\beta}{\Gamma}$ is the probability for the compound nucleus C to decay to the exit channel β. [36]

1.5.2 Models of compound nucleus reaction

In what follows we will briefly refer to the compound nucleus models as the statistical model (the Hauser- Feshbach theory (1952)) which comes as a result from the Breit- Wigner resonance theory and the evaporation model for the decay of the compound nucleus (the Weisskopf- Ewing theory (1940)) .

1.5.2.1 Breit- Winger Resonance

When the projectile comes in touch with the target nucleus, the nucleons interact with each other, the beam energy is distributed among all the nucleons most of the time of the interaction, and an excited compound nucleus is formed. None of the nucleons has enough energy to escape but finally the compound nucleus will decay. When the beam energy is low and the compound nucleus has a low excitation energy, then it presents discrete quantum states which have a particular spin and orbit. However, due to the effect of instability of the compound nucleus, each of the decaying states, present an imprecise energy described by a width Γ. The width Γ is given according to the equation $\Gamma \approx \hbar/\tau$ (1.23), where τ is the lifetime of the state.

When the beam energy of the projectile is the same with the energy of one of these quantum states of the compound nucleus (E_r), then a compound resonance is formed (*Breit- Winger*

resonance) and it is presented as a sharp peak in the reaction cross section. The compound resonance is a characteristic of the compound nucleus and not of the pair of the particles from which it is formed. So, the reaction cross section from the entrance channel α to the exit channel β (into which the compound nucleus decays) at the beam energy E, is given from the following formula (1.24) :

$$\sigma_{\alpha\beta} = \frac{\pi}{k_a^2} \frac{\Gamma_\alpha \Gamma_\beta}{\left(E - E_r\right)^2 + \frac{1}{4}\Gamma^2} \qquad (1.24)$$

where E_r is the resonance energy, E is the beam energy, $k_\alpha = p_\alpha/\hbar$ is the wave number of the incident particle in the entrance channel, Γ_α is the width for the decay into the a + X channel, Γ_β is the width for the decay to the exit channel β (Y + b) and Γ is the total width which means that it is the sum of all the widths of the possible exit channels. [37]

While the beam energy increases, as well as the excitation energy, the density of the compound nucleus states gets bigger, the resonances come closer until they overlap each other and the cross section turns to be a smoothly energy function. None state can be analyzed separately and this leads to the statistical model of the formation and the decay of the compound nucleus. [37]

1.5.2.2 The Hauser - Feshbach formula

The statistical model is used for the calculation of the cross sections of reactions averaged over a large number of compound nuclear states as a result of the overlapping compound resonances. When the incident particle collides with the target nucleus, it is absorbed by the target. Using the Bohr Independence Hypothesis and the conservation of the angular momentum, the cross section can be written as a function of the projectile transmission coefficient T_α and of its probability to traverse the surface of the target nucleus. So, from the Bohr Independence Hypothesis, the cross section, as already said, can be written as :

$$\sigma_{\alpha\beta} = \sigma_\alpha P_\beta \qquad (1.25)$$

where σ_α is the cross section for the formation of the compound nucleus and P_β is the probability of its decay into the exit channel β.

The cross section of the compound nucleus formation for a particular angular momentum is given from the equation:

$$\sigma_\alpha = \frac{\pi}{k_\alpha^2} g_\alpha T_a = \frac{\pi}{k_\alpha^2}(2l+1)T_a \qquad (1.26)$$

where $g_\alpha=(2l+1)$ is the statistical weight due to the angular momentum and T_α is the transmission coefficient in the entrance channel. The maximum transmission coefficient T_α is

the unit, but it is usually less than the unit. The T_α can be calculated from the appropriate optical model potentials. Thus, the cross section of a compound nucleus reaction from a single incident channel α to a single exit channel β, for a particular angular momentum l, is written according to the formula:

$$\sigma_{\alpha\beta} = \sigma_\alpha P_\beta = \frac{\pi}{k_\alpha^2}(2l+1)\frac{T_\alpha T_\beta}{\sum_i T_i} \qquad (1.27)$$

where P_β is the ratio of the corresponding transmission coefficients and the sum on the right-hand side represents all the possible exit channels. This is known as *the Hauser-Feshbach theory* and it is also used for the prediction of the differential cross sections. The angular distribution of the reaction products coming from a compound nucleus mechanism are symmetric at around the 90˚ in the center of mass system, while in the direct reactions they are forward peaked. [37,38,40]

1.5.2.3 The evaporation model for decay of the compound nucleus (Weisskopf - Ewing theory)

The Weisskopf theory is the first statistical model which was used for the description of the compound nuclear decay. It compares the emission of particles from the excited compound nucleus, which is formed after the projectile collides with the target nucleus, with the evaporation of molecules from a fluid. Considering that the reaction occurs in the entrance channel α (energy beam E) and the decay of the compound nucleus occurs in the exit channel α' (energy E'), the cross section for the formation of the compound nucleus is $\sigma_{c\alpha}(E)$ and the probability of its decay into the channel α' to states with energy between E' and E'+dE' is $P_{\alpha'}(E,E')$, then the reaction cross section from the α channel to the α' channel can be written as:

$$\sigma_{\alpha\alpha'}(E,E')dE' = \sigma_{c\alpha}(E)P_{a'}(E,E')dE' \qquad (1.28)$$

and the Weisskopf-Ewing formula for the reaction cross section is given according to the equation:

$$\sigma_{\alpha\alpha'}(E,E')dE' = \sigma_{c\alpha}(E)\frac{g_{a'}m_{a'}E'\sigma_{ca'}(E')\omega_{a'}(U)dE'}{\sum_{a''}g_{a''}m_{a''}\int_0^{E-Q''}E''\sigma_{ca''}(E'')\omega_{a''}(U'')dE''} \qquad (1.29)$$

where Q'' is the Q-value of the reaction from channel α to an exit channel α'', U is the residual nucleus energy: U=E-E'-B where B is the binding energy of the ejectile in the compound nucleus, $\omega_{\alpha'}(U)$ is the level density of the residual nucleus in the channel α' at excitation energy U, $g_{\alpha'}=2i_\alpha+1$ and $g_{\alpha'}=2i_{\alpha'}+1$ are the statistical weights of channels α (initial) and α' (final) where i_α and $i_{\alpha'}$ are the spin of the projectile and the ejectile , m_α and $m_{\alpha'}$ are the

reduced masses in the channels α and α'. The level density of the residual nucleus of the reaction depends on the excitation energy and it can be expressed either as a constant temperature formula or as an equidistant spacing approximation with the spacing of the states being predicted by the Fermi gas model.[38]

With this evaporation theory, the differential cross sections can be calculated mostly for reactions to continuum states. In general, the Weisskopf-Ewing formula is used for detailed analyses of the cross sections of several outgoing channels in a particular reaction. It is also used for Monte Carlo code calculations for the description of the decay of a fully equilibrated nuclei [38,40] as is the case in the calculations performed for this experimental work by Dr N. Nicolis but in a generalized approach [43-45]

1.6 Differences between direct and compound nucleus reactions

- In compound nucleus reactions, the angular distribution is symmetric at around 90˚, due to the long lifetime of the compound nucleus which indicates the memory loss of the entrance channel, as well as, due to the conservation of the angular momentum. In the direct reactions the angular distributions are not symmetric and they tend to be strongly peaked at the forward angles.

- The duration of the direct reactions is about 10^{-22} sec, which is the time that the projectile needs to cross the target nucleus, while the duration of the compound nucleus mechanisms is much longer (10^{-16} sec). [38]

1.7 Coulomb barrier

In order for a nuclear reaction to take place, the projectile and the target must come close to each other. With the exception of neutrons, in a nuclear reaction both the projectile and the target are positively charged and when they approach each other, they repel due to the electrostatic interaction. As a result, the projectile needs to overcome this energy barrier due to the electrostatic interaction in order the nuclear reaction to take place, as it can be seen in Figure 1.6. This energy barrier is called the *Coulomb barrier* and is given by the electrostatic potential energy:

$$V_{coul.} = k\frac{q_1 q_2}{r} = \frac{1}{4\pi\varepsilon_o}\frac{Z_1 Z_2 e^2}{r} \qquad (1.30)$$

where Z_1, Z_2 are the atomic numbers of the projectile and the target, r is the distance between them (the sum of the projectile radius and the target radius), e is the elementary charge $\approx 1.6*10^{-19}$ Cb and ε_o is the permittivity of free space $\approx 8.854187*10^{-12}$ Farad/m. In another more practical form we can write the formula for the Coulomb barrier as:

$$V_{coul.} = 1.44\frac{Z_1 Z_2}{r} \qquad (1.31)$$

and if r is in fm then the Coulomb barrier V will be in MeV. The nuclei must collide at high velocities in order the projectile to overcome this energy barrier and their kinetic energies drive them close enough for the strong interaction to take place and bind them together or can interact with the target nucleus via a tunneling effect.

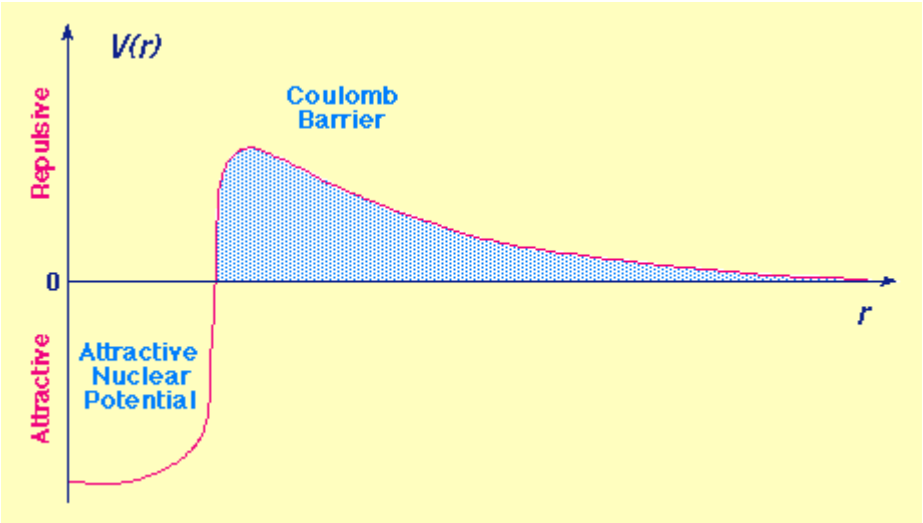

FIG. 1.6: The projectile as it comes closer to the target, a repulsive force is performed due to the electrostatic interaction, so in order the nuclear reaction to take place, the projectile needs to overcome the Coulomb barrier. After it has overcome it, then the strong interaction takes place and the nuclei interact between each other.

1.8 Semi-conductors

Semiconductors are crystalline materials which can be considered as a sum of interacting atoms. When the atoms approach each other close enough to form a solid, the valence electrons interact with each other and their atomic levels are broadened into wider regions, the energy bands. This energy band structure is consisted of three regions: the valence band, the "forbidden" energy gap and the conduction band(Figure 1.7).

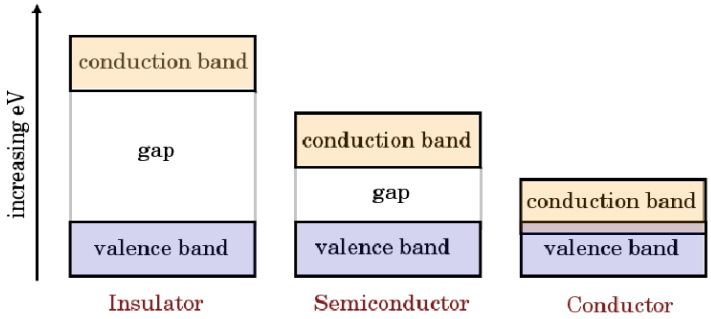

FIG. 1.7: Energy band of insulator, semiconductor and conductor

The *valence band* corresponds to the outer-shell electrons which are tightly bound to specific lattice sites in the crystal and it is totally occupied by electrons. In the *"forbidden" energy gap* there are no available energy levels and its size determines whether the material is classified as a conductor, an insulator or a semiconductor. The *conductivity band* is the region where the electrons are detached from their parent atoms and they are free to traverse the entire crystal.

The electrons in the crystal are exactly as many as there are needed to fill completely the available sites within the valence band. When the temperature is different than 0 K, thermal energy is shared among the electrons, and if a valence electron gains sufficient energy, then it can be excited into the conduction band, leaving a vacancy (hole) in its original position. So an electron-hole pair is created.

In a pure semiconductor (intrinsic semiconductor), the number of electrons in the conduction band is equal to the number of holes in the valence band. This balance can be destroyed by the introduction (*doping*) of a small amount of impurity atoms, which have one more or one less valence electron in their atomic shell. For example, for the silicon semiconductor, which is tetravalent, the dopant may be pentavalent or trivalent.

For a pentavalent dopant, in the ground state, four electrons fill the valence band and one electron is left. This extra electron goes to a discrete energy level (donor level), which is created in the energy gap close to the conduction band, and then it can easily be excited to the conduction band. The extra electrons fill up the holes which are normally formed, decreasing the hole concentration. Thus, the electric current is due to the movement of electrons as they are the majority charge carriers. These are referred to as the ***n-type semiconductors*** (donor doped semiconductors).

For a trivalent dopant, in the ground state, three electrons fill the valence band and one valence electron is missing, leaving one covalent bond unsaturated (one hole). A discrete energy state (acceptor level) is created in the energy gap close to the valence band, to which the electrons from the valence band can be easily excited, leaving behind them extra holes and decreasing the concentration of the free electrons. So, there is an excess of holes in the crystal and the electric current is due to the movement of holes as they are the majority charge carriers. These semiconductors are called as ***p-type semiconductors*** (acceptor doped semiconductors). [46, 47]

1.8.1 The p-n semiconductor junction

The semiconductor detectors are based on the formation of a junction between the *n-type* and the *p-type* semiconductors. Due to the different concentrations of the electrons and the holes in the two regions of the junction, there is a diffusion of holes to the *n-region*, as well as a diffusion of conduction electrons towards the *p-region* (Figure 1.8). Thus, the p-region has a negative charge, while the n-region becomes positive. This effect creates an electric field across the junction which finally stops the further diffusion and an immobile charge distribution is presented. The region over which the charge imbalance exists is called as *depletion region* and is presented in both the p and the n sides of the junction.

However, in the p-n junction the intrinsic electric field is not enough and the thickness of the depletion zone is quite small that it can only stop the lowest energy particles. So, an external voltage is necessary to be applied across the junction in the reverse biased direction. By applying this *reverse-bias* voltage to the junction, the holes are attracted in the p-region towards the p contact, and the electrons in the n-region towards the n contact. The depletion zone is widened (Figure 1.9), as well as the sensitive volume of the crystal for radiation detection.[35,41,46,47]

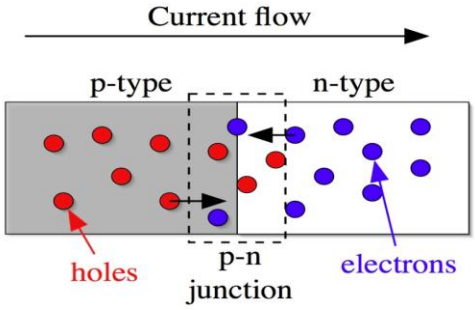

FIG. 1.8: The p-n junction. The electrons from the n-region are diffused to the p-region while the holes from the p-region are diffused to the n-region.

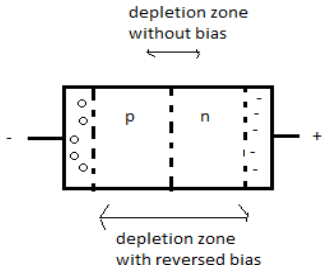

FIG. 1.9: The reversed bias junction. The depletion zone is widened while applying the reversed bias voltage to the junction.

The most widely used silicon detectors for the detection of charged particles are the *surface barrier detectors.* They rely on junction formed between a semiconductor and certain metals, usually n-type silicon with gold or p-type silicon with aluminum. In order to be fabricated, the silicon surface is firstly etched and then a thin layer of gold is deposited via evaporation for electrical contact. Before the deposition, the surface is oxidized slightly. Also, surface barriers can be produced by starting with a p-type crystal and evaporating aluminum which is deposited on the surface for electrical contact. The thickness and the depletion zone regions of the SSB detectors vary. One disadvantage of the surface barrier detectors is their sensitivity to light and to damages from exposure to vapors. [46,47]

1.9 Silicon Strip Detectors

In order to obtain spatial information for a charged particle which traverses a detector, there are two types of detectors. The first uses a continuous readout with a resistive charge division method while the second employs a discrete array of readout elements. The continuous detector is actually a diode with a resistive electrode on the front face and a low resistive back electrode. When a charged particle passes through it, its position and its energy are obtained.

The *silicon strip detectors* are actually discrete detectors. They are consisted of a series of individual strips placed on the same semiconductor base (Figure 1.10). Usually n-type silicon is used as the base material into which highly p- doped (p^+) strips with aluminum contacts are implanted. The metallic cover permits the connection between the detector and the readout electronics via a micro bounding. On the opposite surface (back face), a highly n- doped (n^+) electrode is placed. Each strip acts as a separate detector and forms a p-n junction with the n-type silicon bulk. The gap between the strips is electrically controlled in order to maintain isolation between adjacent diodes. A reverse biased voltage is applied between the p- strips and the back side in order to make the full depth of the bulk sensitive. When a charged particle passes through the silicon detector, it creates ionization in the bulk of silicon. Then electrons from the silicon atom's are released while holes are left behind. So, electron–hole pairs are created. Due to the electric field inside the bulk, the charge carriers start to drift towards the electrodes. The holes drift towards the negatively charged p- type strips, while the electrons drift towards the positively charged back side. The readout electronics is connected to each strip and collects the charges which are generated by the incident particle. From the signals on the individual strips the position of the through going particle is deduced. [46-49]

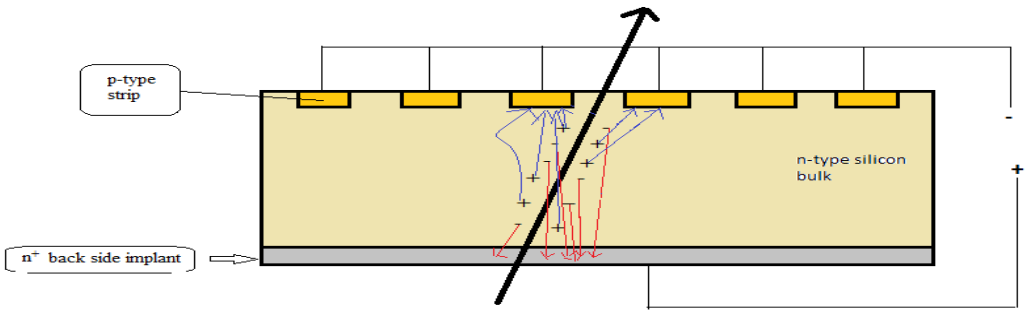

FIG.1.10: A silicon strip detector. It is consisted of a series of p-type strips implanted on the n-type silicon bulk and on the opposite side a highly-doped n type is placed.

1.10 Double Sided Silicon Strip Detectors

The Double Sided Silicon Strip Detector (DSSSD) is a silicon detector with orthogonally oriented readout strips implanted on its two opposite sides. One DSSSD is consisted of a n-type silicon layer which has p^+ doped and n^+ doped implanted strips with aluminum contacts, orthogonally oriented on its two sides (p-side and n- side) as it is shown in Figure 1.11. Each n^+ strip is surrounded by a p^+ implantation (p-stop strip) in order to be isolated from any adjacent strip. A reverse biased voltage is applied over the detector, creating an electric field throughout the bulk material that prevents recombination of the electrons and holes. When a charged particle traverses the depleted silicon bulk, free carriers are released in proportion to the energy of ionization. These free carriers (electrons, holes) migrate to the nearest n^+ and p^+ strips respectively, producing two coincidence signals which can be recognized as a single event at a particular position on the detector. Then, this signal is amplified by the amplifier which is connected to every strip, and the two coordinates of the position of the incoming particle and the deposited energy are determined through the connected readout electronics. A DSSSD can also be formed by using a p-type silicon layer with n^+ and p^+ implanted strips on the front and the back side of the detector. However, usually the most popular DSSSD are the n-type detectors.

The DSSSD are widely used in the fields of radioactive beam physics and nuclear astrophysics, as well as, in many applications such as medical imaging sensors, radiation detectors, sensing detectors in space experiments and tracking detectors of charged particles in high energy physics experiments. They are also used for X-Ray and γ-ray detection owing to the silicon sensitivity to electromagnetic radiation. Moreover, the DSSSD detectors are used in the EXPADES system [50] (the detection array of the EXOTIC facility at LNL) and in the GLORIA system [51-52] developed at Huelva University. One of their advantages is that they can measure two coordinates using one detector layer, while the single sided silicon strip detectors need an extra detector layer for providing two-dimensional information. Also, the DSSSD can cover a large area using a relatively small number of readout channels with a good position resolution. However, due to the complicated manufacturing and handle

procedures they are more expensive and they need special strip insulation of n-side (p-stop). [53-56]

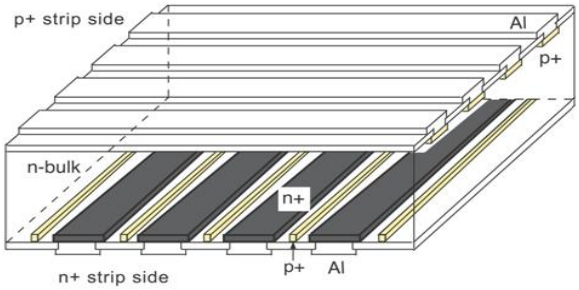

FIG. 1.11: A Double Sided Silicon Strip Detector. It is consisted of a n-type silicon bulk with p^+ and n^+ implanted strips with aluminum contacts, orthogonally oriented on its two sides. The n^+ strips are separated with p^+ implantations.

1.11 The DINEX telescope

The DINEX (Dispersión de Núcleus Exóticos) telescope was designed for better energy resolution, for high granularity and for covering a solid angle as large as possible. It allows mass and charge separation of the reaction products. The DINEX detector array consists of one ΔE detector and one E detector. The ΔE stage of the telescope is a DSSSD silicon detector, ~48 μm thick, with an active area of 5x5 cm and 16 vertical and 16 horizontal strips. The E stage is a silicon detector, 530 μm thick. The ΔE detector is placed over the thick E detector and captures the recoil ion energy of the 2 reaction products ^{3}He and ^{4}He that they lose as they pass through the detector. The E detector, as a thick detector, does not allow the particles to pass through, thereby capturing the total energy (E). Its depletion layer is thick enough in order to cover the whole range from the incident point to the stop point of the particles. Using the ΔE - E technique, the particles can be identified via the Z separation [51,57]. Today the improvement of the DINEX telescope is known as the GLORIA telescope (Global Reaction Array) and in the present work only one of its telescopes has been used.

2. Experimental details

2.1 Experimental setup

The experiment was performed at the Instituto Nazionali di Fisica Nucleare- Laboratori Nazionali del Sud in Catania (INFN-LNS), Italy. A view of the experimental hall where our study took place is presented in Figure 2.1. The system under study was the ^{6}Li + p in inverse kinematics. Beams of ^{6}Li were accelerated at the energies of 16, 20, 25 and 29 MeV and impinged on a ~ 300 μg/cm^{2} CH_2 target. The elastically scattered ^{6}Li ions, were directed due to kinematical laws only at forward angles, and were momentum analyzed by the MAGNEX spectrometer [30-34]. The analysis of elastic scattering is given in [30-31]. For the reaction ^{6}Li + p → ^{3}He + ^{4}He which is presented in this work, measurements were performed with a module of the DINEX telescope [51]. A schematic set up of the telescope inside the reaction chamber is given in Figure 2.2 while a view of it in Figure 2.3 It was set at a distance 15.5 cm far from the target, allocating an angular range of θ_{lab} =16˚ to 34˚. The angular resolution in the lab system is ±0.58°. The DINEX telescope consists of one ΔE detector and two E detectors, but only one E detector is used for the present data analysis (Figure 2.4 and 2.5). The ΔE stage of the telescope is a DSSSD silicon detector, 48 μm thick, with an active area of 5x5 cm and 16 vertical and 16 horizontal strips. The E stage is a silicon pad detector, 530 μm thick. As the ΔE stage of the telescope absorbs a part of the recoil ion energy of the 2 reaction products ^{3}He and ^{4}He, it allows a Z separation via the ΔE - E technique.

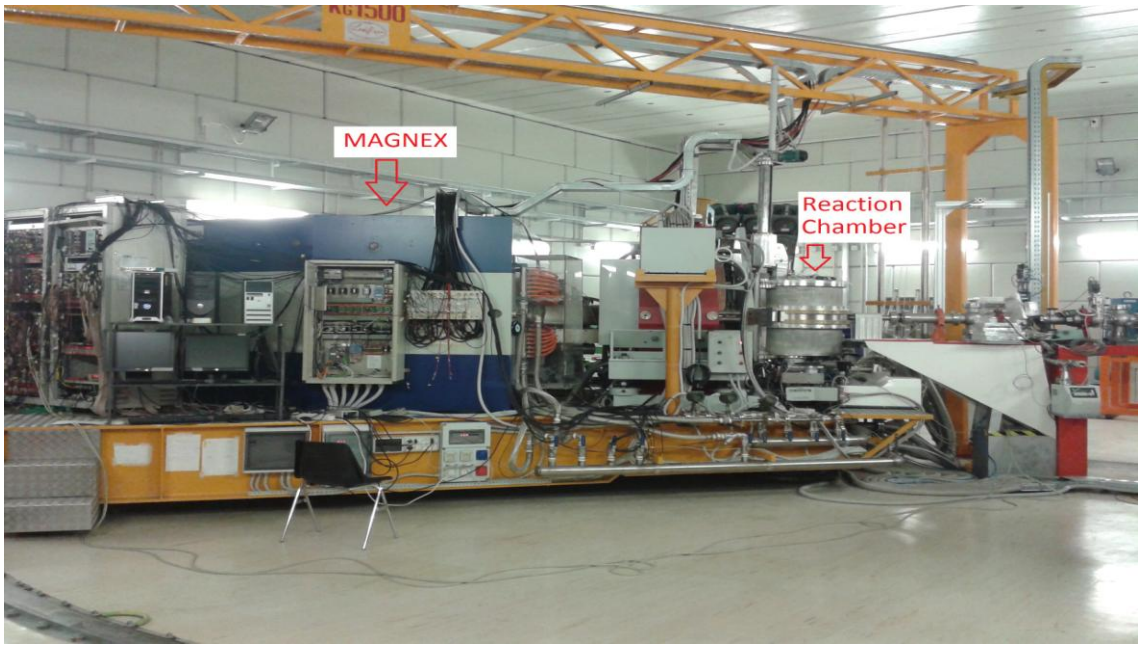

FIG. 2.1: A photo of the experimental hall. At the right side of the picture is the chamber where the reaction takes place, while at the left side is the MAGNEX spectrometer.

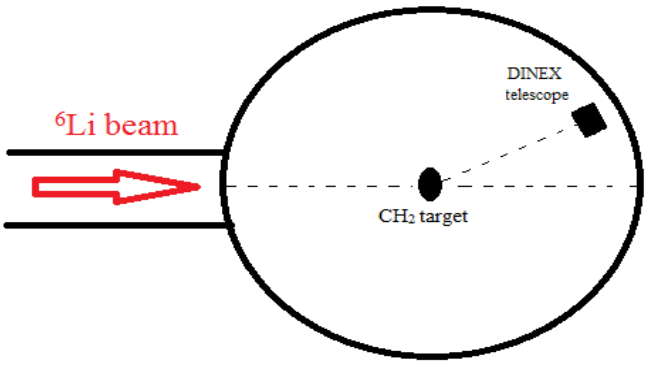

FIG. 2.2: Schematic representation of the reaction chamber. ^{6}Li beams were accelerated at the energies 16, 20, 25 and 29 MeV and impinged on a ~ 300 μg/cm^2 CH_2 target. The reaction products 3He and 4He were recorded by one DINEX telescope, allocating an angular range of θ_{lab} =16˚ to 34˚ at a distance of 15.5 cm far from the target.

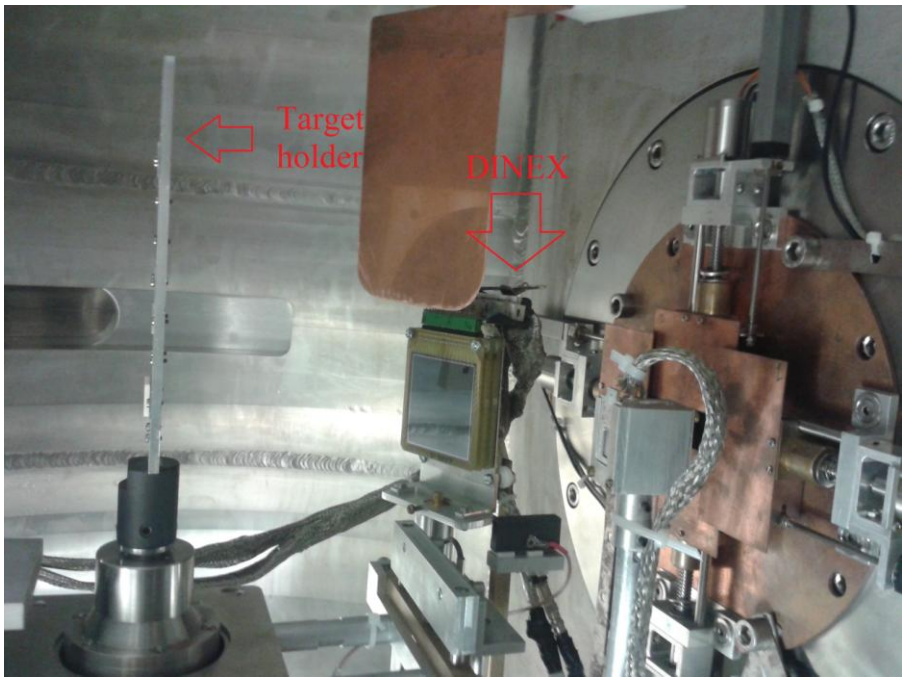

FIG. 2.3: View of the reaction chamber. The target holder and the DINEX telescope are shown.

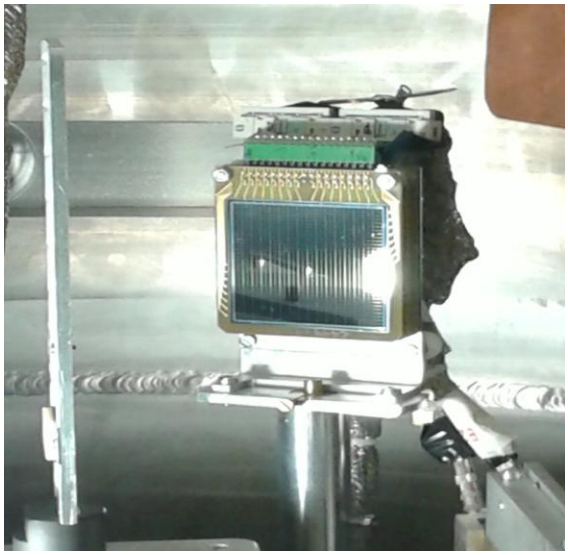

FIG. 2.4: The DINEX telescope. The ΔE stage of the telescope is a DSSSD silicon detector, 48 μm thick, with an active area of 5x5 cm and 16 strips per side. The E stage is a silicon pad detector, 530 μm thick

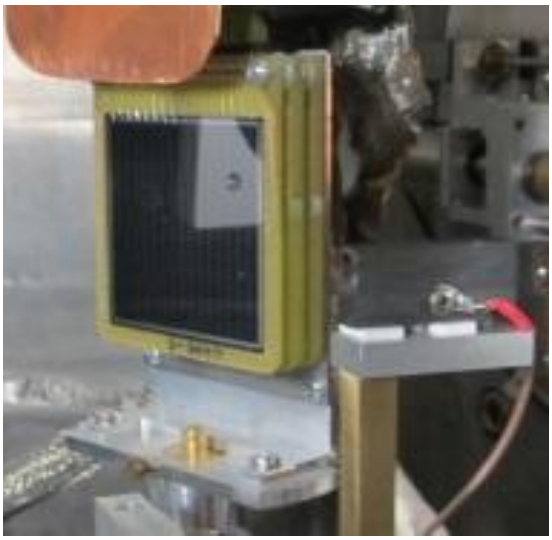

FIG. 2.5: Another photo of the DINEX telescope. The ΔE detector and the E detector can be clearly distinguished.

All the targets were mounted in a target ladder, in the middle of the reaction chamber. The target ladder holds the targets vertically aligned above one another, as shown in Figure 2.6. By changing the height of the ladder, any one of the targets could be positioned in the beam. From top to the bottom we can see a ^{12}C target , which is used for energy calibration purposes as it is described in chapter 2.2, and it is also used for estimating the background due to carbon. It is followed by one of the CH_2 targets, 308 μg/cm^2 thick which is used for the main reaction measurement at the energies of 16, 25, and 29 MeV, while the last CH_2 target, 489 μg/cm^2 thick is used at the energy of 20 MeV. The ^{197}Au target is used for the determination of solid angle and for energy calibration purposes, as it is described in the chapter 2.2 and 2.3. The Quartz and the Allumina is used for the alignment of the beam.

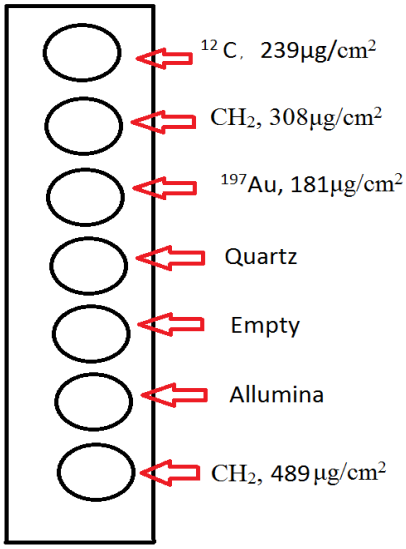

FIG. 2.6: Schematic representation of the target holder.

Detectors provide information on detected radiation in the form of electrical pulse signals. In order to extract the information which is provided by the detectors, the signal must be further processed by an electronic system as shown in figure 2.7.

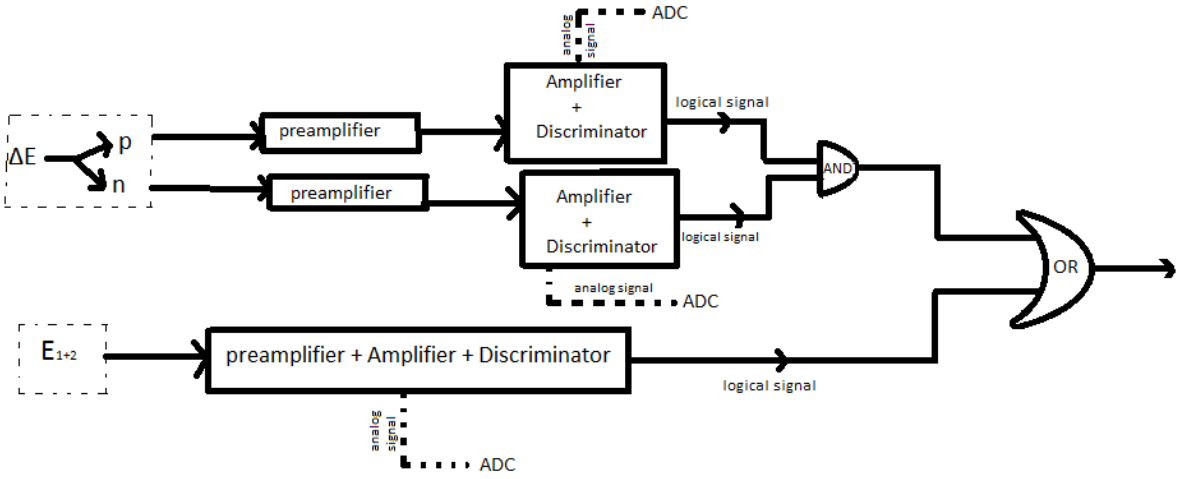

FIG. 2.7 : Schematic representation of the electronic modules used in the experiment.

The output of the ΔE detector was connected to a Mesytec preamplifier (MPR-64 with 4x16 channels). The preamplifier provides an interface between the detector and the pulse processing electronics, amplifying weak signals from the detector, and shapes the subsequent output pulses. The linear output signals (energy and time signals) from the preamplifier were fed to a compact Mesytec electronic unit (STM-16) , providing amplification and discrimination. From that electronic unit two kind of signals went out. A logical signal which went to the OR unit and an analog signal which went to the ADC unit. The logical signal,

which went to the OR unit, is the result of the coincidence of the logical signals coming from the n and p side of the DSSSD detector (from the front side and the back side of the ΔE detector). The output signal from the E detector was fed to a compact Mesytec unit MSI-8 (8 channel unit) providing a preamplifier, amplifier and a discriminator processing. From that electronic unit, a logical and an analog signal went out. The logical signal was directed to the OR unit to contribute in the gate, while the analog signal went to the ADC unit for recording the energy. The data which came either from the ΔE detector or from the E detector, after being recorded in the PC controlled acquisition system, were analyzed off line.

2.2 Energy calibration

In principle a good energy calibration is essential for the identification of the particles in a spectrum and for an accurate data reduction. In this study the ΔE-E technique was enough for the identification of the reaction products ^{3}He and ^{4}He as the Q-values of other reactions were very different from the reaction under study. However for a "double checking" procedure and for the global view of the study we have proceed with a detailed energy calibration of both ΔE and E stages of the telescope.

It is known that the reaction ^{6}Li + p can give several channels such as the elastic channel, the break up channel, and the compound and transfer reaction channels. Because of the CH_2 target, there is also the reactions on carbon, ^{6}Li + ^{12}C, which can give several channels, such as the elastic channel, the break up channel, the fusion channel and transfer reaction channels some of them giving as reaction products ^{3}He and ^{4}He. For the calculation of the differential cross section, only the ^{3}He and the ^{4}He that originate from the reaction ^{6}Li + p → ^{3}He + ^{4}He and not from any other channel of this reaction or from the reaction ^{6}Li + ^{12}C are required. In order the ^{3}He and the ^{4}He to be identified in the spectrum, a good energy calibration is necessary.

The data analysis is performed using the program PAW [58]. For the kinematic prediction the nuclear reaction video project [59] is adopted. Last the energy loss and the energy remaining on E detector are obtained by taking into account the thickness of the target and of the ΔE detector adopting the Lise++ program [60].

2.2.1 Energy Calibration of ΔE detector

For the energy calibration of ΔE detector, the elastic scattering measurements performed with a gold foil 180 μg/cm^2 thick and with a carbon foil 240 μg/cm^2 thick, at bombarding energies 29 MeV and 25 MeV, are used (Figure 2.8 and 2.9). The energy calibration is performed assuming a linear function (2.1) as:

$$E = a * channel + b \quad (2.1)$$

The best fitted parameters a, b are given in Table 2.1. Some typical plots of the energy calibration for certain strips are shown in Figures 2.10 and 2.11

TABLE 2.1: Fitted parameters a, b to a linear function for the energy calibration of ΔE detector. The calibration is based on the elastic scattering measurements performed with gold and carbon foils at bombarding energies 29 MeV and 25 MeV.

strip	θ_{lab}(°)	a	b
1	16.38	0.004556	-0.386896
2	17.54	0.004816	0.000162
3	18.70	0.004912	-0.211269
4	19.86	0.005275	-0.690453
5	21.02	0.005058	-0.698301
6	22.18	0.005359	-1.178557
7	23.34	0.004657	0.430023
8	24.50	0.005017	-0.483877
9	25.66	0.005957	-1.260332
10	26.82	0.005939	-1.266226
11	27.98	0.003924	-1.682743
12	29.14	0.005956	-1.682743
13	30.30	0.006005	-1.683126
14	31.46	0.005762	-1.810744
15	32.62	0.006223	-1.993463
16	33.78	0.005029	-1.06319

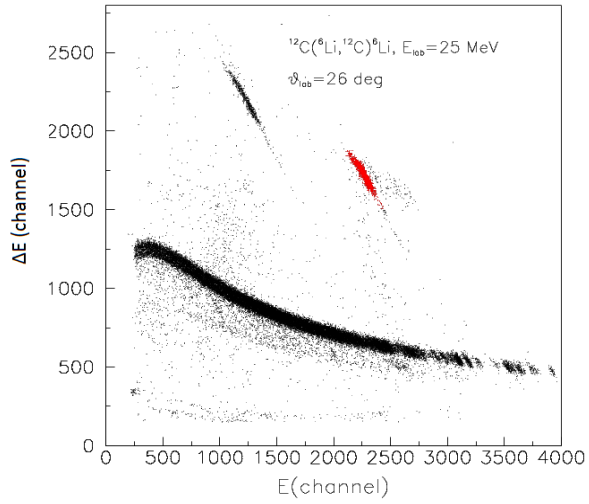

FIG. 2.8: A typical two dimension spectrum ΔE-E collected at θ_{lab}=26˚ for the elastic scattering $^{6}Li + ^{12}C \rightarrow ^{6}Li + ^{12}C$ at bombarding energy 25 MeV . The red spot corresponds to ^{6}Li .

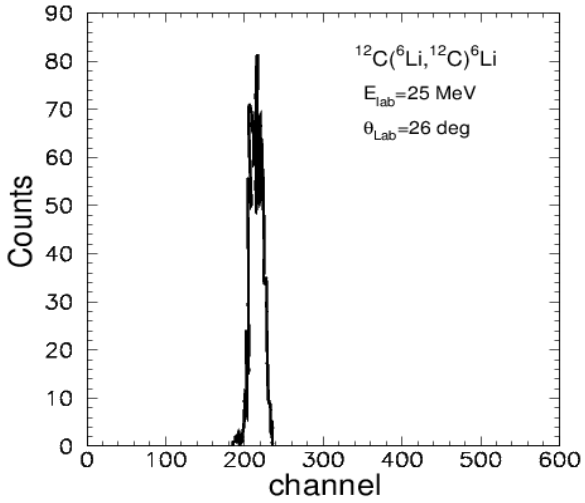

FIG. 2.9: A typical one dimension ΔE- spectrum collected at θ_{lab}=16˚ for the elastic scattering $^{6}Li + ^{12}C \rightarrow ^{6}Li + ^{12}C$ at bombarding energy 25 MeV .The peak represents ^{6}Li on ΔE detector.

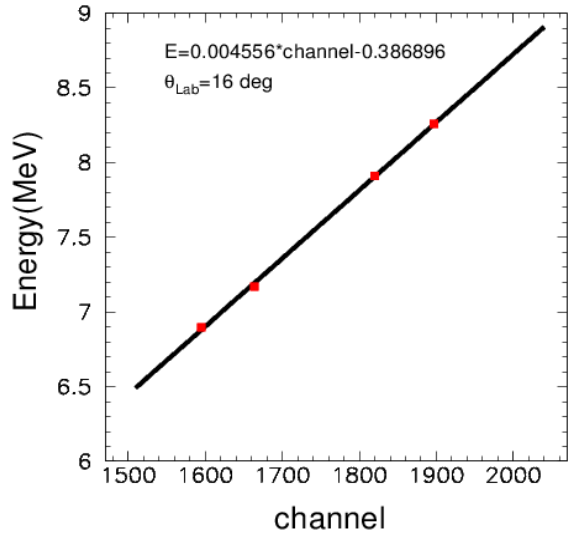

FIG. 2.10: Energy versus channel plot for the energy calibration of ΔE detector. It corresponds to the first strip (θ_{lab}=16˚). Data are designated with the red cubes while the black solid line corresponds to the best fit assuming a linear function.

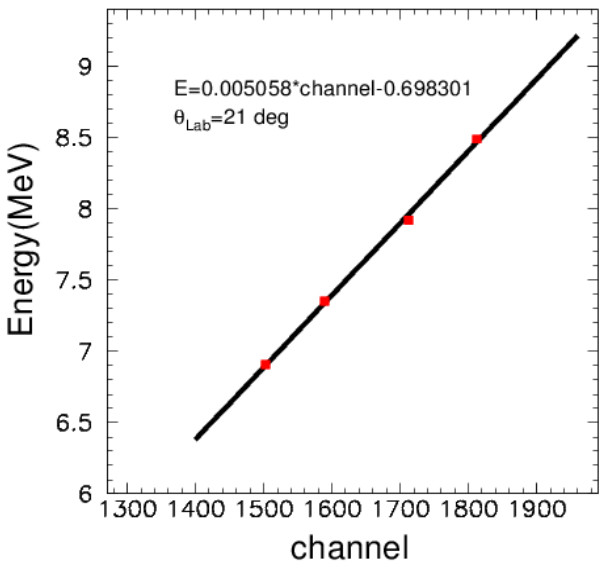

FIG. 2.11: Same as in Fig. 2.10 but for the 5th strip (θ_{lab}=21˚).

For the verification of the energy calibration of ΔE detector, the first solution of ^{3}He and of ^{4}He from the reaction $^{6}Li + p \rightarrow {}^{3}He + {}^{4}He$ at bombarding energy 29 MeV are used. The deviations between the experimental energy and the energy from kinematical prediction are shown in Table 2.2 and Table 2.3. Also extensive tables with the energies from kinematical prediction for the reaction products ^{3}He and ^{4}He, for all the beam energies, are presented in appendix D.

TABLE 2.2: Experimental energies via our energy calibration for the 1st kinematic solution of ^{3}He originating from the reaction $^{6}Li + p \rightarrow {}^{3}He + {}^{4}He$ at 29 MeV, are compared with the theoretical values. The deviation of experimental and theoretical values is also presented.

strip	$\theta_{lab}(^{\circ})$	E predicted (MeV)	E experimental (MeV)	% deviation
1	16.38	1.8481	1.7493	5.35
2	17.54	1.8782	2.0294	8.05
3	18.70	1.9127	1.9434	1.61
4	19.86	1.9469	1.7062	12.36
5	21.02	1.9883	1.6119	18.93
6	22.18	2.0323	1.5106	25.67
7	23.34	2.0822	2.5960	24.68
8	24.50	2.1368	2.0287	5.05
9	25.66	2.1971	1.6359	25.54
10	26.82	2.2649	1.7292	23.65
11	27.98	2.3399	3.2992	41.00
12	29.14	2.4249	1.6138	33.45
13	30.30	2.5213	1.7236	31.64
14	31.46	2.6278	1.7580	33.10
15	32.62	2.7573	1.9085	30.78
16	33.78	2.9041	2.4219	16.60

TABLE 2.3: Same as in Table 2.1 but for the reaction product ^{4}He.

strip	θ_{lab}(˚)	E predicted (MeV)	E experimental (MeV)	% deviation
1	16.38	2.25	2.23	0.89
2	17.54	2.31	2.51	8.66
3	18.70	2.37	2.46	3.70
4	19.86	2.44	2.30	5.74
5	21.02	2.52	2.34	7.14
6	22.18	2.61	2.28	12.64
7	23.34	2.73	3.26	19.41
8	24.50	2.86	2.84	0.70
9	25.66	3.03	2.71	10.56
10	26.82	3.25	3.01	7.38
11	27.98	3.55	4.34	22.25
12	29.14	4.07	3.59	11.79

The deviations between the energy from kinematic prediction and the experimental energy, in some strips are not small. This is due to the fact that the main measurement with the CH_2 target followed several days after the calibration ones and it is apparent that the amplification conditions might have changed in some strips.

However, this has no effect on the analysis of the ΔE-E peaks of ^{3}He and ^{4}He. The peaks from the first solution of ^{3}He and of ^{4}He can be well identified. No other peaks are included from other channels nearby. The second solution of ^{3}He and of ^{4}He cannot be identified as they stop in the first stage. The second solution of ^{3}He cannot be seen anyhow because of the high discrimination threshold, while the second solution of ^{4}He is below a high continuous background and as a result it cannot be observed (Figure 2.12).

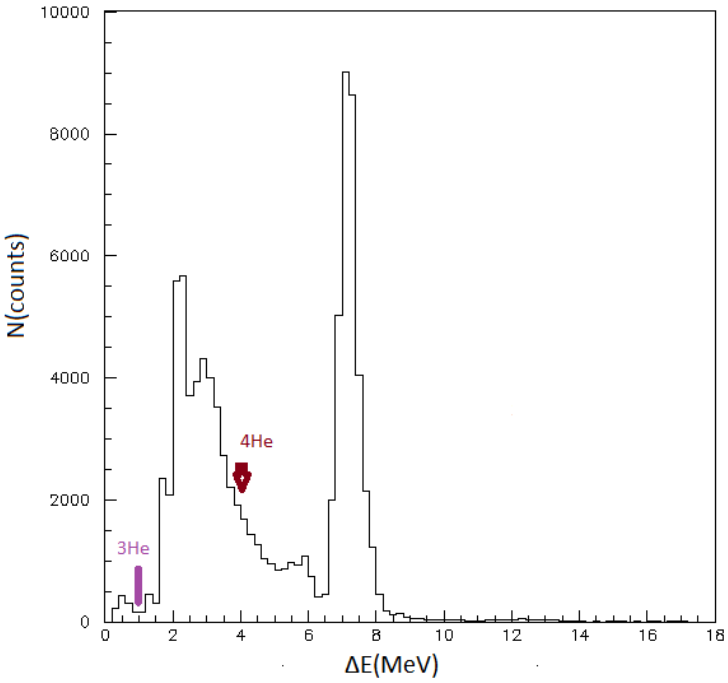

FIG. 2.12: A typical calibrated one dimension ΔE- spectrum collected at θ_{lab}=16˚, for the reaction ^{6}Li + p at bombarding energy 29 MeV without any condition. The energies from kinematic prediction on ΔE detector for the second solution of ^{3}He and of ^{4}He from the reaction ^{6}Li + p → ^{3}He + ^{4}He are shown. The pink arrow represents the expected energy for the 2nd solution of ^{3}He, while the brown arrow represents the expected energy for the 2nd solution of ^{4}He. Peaks for the second solution of ^{3}He and ^{4}He cannot be seen due to a high discrimination threshold and the large background respectively.

2.2.2 Energy calibration of E detector

The energy calibration of E detector is based on the elastic scattering measurements performed with a carbon foil 240 μg/cm^2 thick at bombarding energies 29 MeV and 25 MeV (Figure 2.13). The equations of the energy calibration are linear according to the formula (2.2):

$$E = a*channel + b \qquad (2.2)$$

The parameters a, b are given in Table 2.4. Some indicative equations of the energy calibration are shown in Figure 2.14 and Figure 2.15

TABLE 2.4: Fitted parameters a, b of a linear function for the energy calibration of E detector. The calibration is based on the elastic scattering measurements performed with carbon foils at bombarding energies 29 MeV and 25 MeV.

strip	$\theta_{lab}(^{\circ})$	a	b
1	16.38	0.007	-0.766
2	17.54	0.007	-1.124
3	18.70	0.007	-1.326
4	19.86	0.007	-1.389
5	21.02	0.007	-1.884
6	22.18	0.007	-1.663
7	23.34	0.007	-1.771
8	24.50	0.007	-3.118
9	25.66	0.006	-0.987
10	26.82	0.006	-0.158
11	27.98	0.007	-1.369
12	29.14	0.007	-1.985
13	30.30	0.007	-1.928
14	31.46	0.007	-2.217
15	32.62	0.006	-0.363
16	33.78	0.007	-2.012

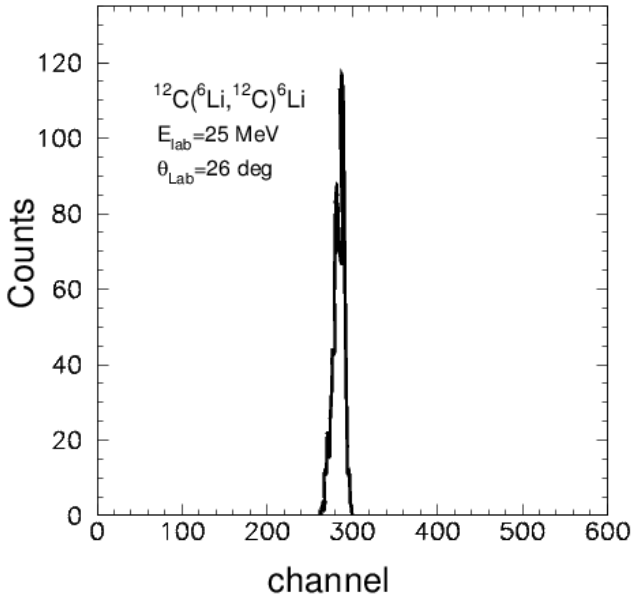

FIG. 2.13: A typical one dimension E- spectrum collected at θ_{lab}=16˚ for the elastic scattering $^{6}Li + ^{12}C \rightarrow ^{6}Li + ^{12}C$ at bombarding energy 25 MeV. The peak corresponds to ^{6}Li on E detector.

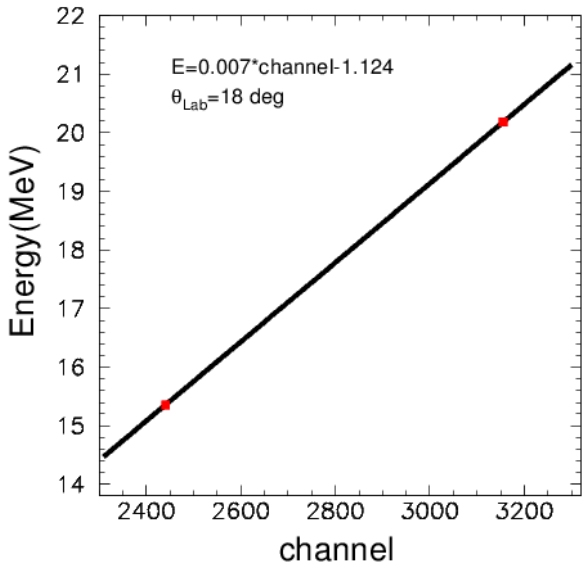

FIG. 2.14: Energy versus channel plot for the energy calibration of the E detector. It corresponds to the second strip of ΔE (θ_{lab}=18˚). Data are designated with the red cubes while the black solid line corresponds to the best fit assuming a linear function.

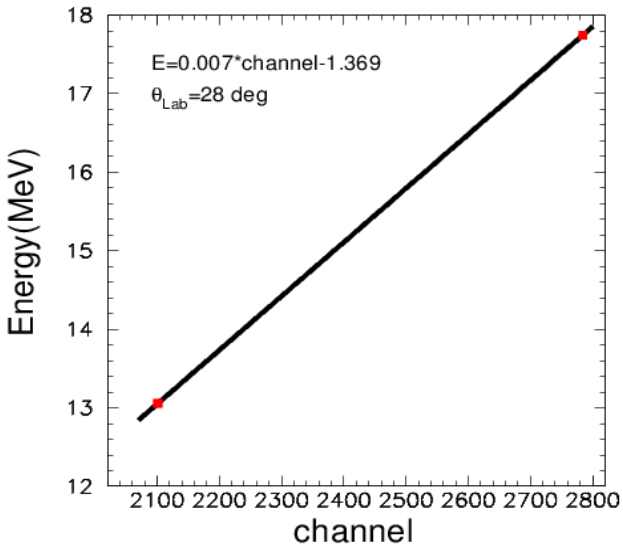

FIG. 2.15: Same as in Figure 2.14 but for the 11th strip (θ_{lab}=28˚).

For the verification of the energy calibration of E detector, the first solution of ^{3}He and of ^{4}He from the reaction $^{6}Li + p \rightarrow {}^{3}He + {}^{4}He$ at the bombarding energy 29 MeV are used. The deviations between the experimental energy and the predicted energy from kinematics are shown in Table 2.5 and Table 2.6

TABLE 2.5: The predicted energy from kinematics (theoretical values) are compared with the experimental values for the energy of the 1^{st} solution for ^{3}He from the reaction $^{6}Li + p \rightarrow {}^{3}He + {}^{4}He$ at 29 MeV. The deviation between theory and experiment is also presented.

strip	$\theta_{lab}(^{\circ})$	E predicted (MeV)	E experimental (MeV)	% deviation
1	16.38	23.83	22.45	5.82
2	17.54	23.30	22.20	4.74
3	18.70	22.72	21.65	4.71
4	19.86	22.13	20.85	5.78
5	21.02	21.49	20.17	6.13
6	22.18	20.81	19.12	8.12
7	23.34	20.10	19.05	5.22
8	24.50	19.36	18.75	3.15
9	25.66	18.59	16.49	11.26
10	26.82	17.77	16.74	5.75
11	27.98	16.93	16.53	2.37
12	29.14	16.03	14.87	7.27
13	30.30	15.12	13.64	9.79
14	31.46	14.17	12.78	9.78
15	32.62	13.13	12.07	8.07
16	33.78	12.08	11.13	7.91

TABLE 2.6: Same as in Table 2.5 but for the 1st solution of ^{4}He.

strip	θ_{lab}(˚)	E predicted (MeV)	E experimental (MeV)	% deviation
1	16.38	24.12	23.33	3.29
2	17.54	23.31	22.41	3.82
3	18.70	22.42	21.35	4.79
4	19.86	21.48	20.10	6.44
5	21.02	20.46	19.01	7.07
6	22.18	19.36	17.68	8.70
7	23.34	18.16	17.09	5.91
8	24.50	16.85	15.72	6.67
9	25.66	15.42	13.47	12.63
10	26.82	13.80	12.99	5.87
11	27.98	11.86	11.33	4.45
12	29.14	9.24	7.98	13.61

As it can be seen, the deviations between the energy predicted from kinematics and the experimental energy do not exceed a 10% variation, but are not the same for all the strips due the possible different conditions of the amplification during the experiment.

2.3 Determination of solid angle

In general, the solid angle, for ideal conditions of point source and large distances between radiated source and detectors, is given by the relation (2.3):

$$\Omega = \frac{S}{R^2} \qquad (2.3)$$

where

S is the surface of the detector

R is the distance between the detector and the target.

In the present study, a more precise way is used for the definition of solid angle as neither of the ideal conditions is due. The solid angle for each strip is determined with an elastic scattering measurement performed with a gold foil 180 μg/cm^2 thick, at one of the lower energies, namely 25 MeV, where the scattering can be considered as pure Rutherford. Data at 16 MeV were not considered for the solid angle, as the dead time was very high and the introduced error to the measurement was estimated to be very large. The energy has been chosen after calculating the Coulomb barrier ($E_{C.b(lab).}$ ~30MeV), via the code described in Appendix B.

The solid angle is then deduced via the relation (2.4):

$$\Omega = \frac{N}{\Phi * D * \sigma_{Ruth.}} \tag{2.4}$$

where:

N represents the number of counts per time, Φ is the flux of the beam, D are the scattering centers of gold and $\sigma_{Ruth.}$ is the Rutherford cross section. When $\sigma_{Ruth.}$ is expressed in mbarn, Φ in particles per time, and D in atoms per cm^2, the solid angle is expressed in steradian after the fraction is multiplied with 10^{27}, as 1 mbarn=10^{-27}cm^2 .

The calculations are performed with the LISE++ program assuming that the reaction takes place in the middle of the target. The flux of the beam was recorded in the Faraday cup and the accuracy of the flux intensity measurement was confirmed via the Rutherford scattering of ^{6}Li on hydrogen, recorded in MAGNEX [30]. The solid angle and the error for each strip are shown in Table 2.7. The error of solid angle is calculated according to the following formula (2.5) deduced in Appendix A:

$$\Rightarrow \quad \sigma_{\Omega} = \frac{1}{\Phi * D * \sigma_{Ruth.}} * \left(N + 0.005 * N^2\right)^{1/2} \tag{2.5}$$

TABLE 2.7: The solid angle and the error for each strip, as determined with the elastic scattering measurement performed with a gold foil at 25MeV, where the scattering can be considered as pure Rutherford.

strip	$\theta_{lab}(^{\circ})$	Ω(sr)	error Ω(sr)
1	16.38	0.00145	0.00010
2	17.54	0.00169	0.00012
3	18.70	0.00176	0.00013
4	19.86	0.00181	0.00013
5	21.02	0.00185	0.00013
6	22.18	0.00186	0.00013
7	23.34	0.00193	0.00014
8	24.50	0.00196	0.00014
9	25.66	0.00197	0.00014
10	26.82	0.00199	0.00014
11	27.98	0.00202	0.00014
12	29.14	0.00202	0.00014
13	30.30	0.00208	0.00015
14	31.46	0.00207	0.00015
15	32.62	0.00206	0.00015
16	33.78	0.00149	0.00011

Errors adopted in the solid angle deduction apart of the statistical error are: a 5% error in the estimation of the target thickness and a 5% error in the measured integrated beam charge.

After the determination of solid angle and the good energy calibration of the detectors, the next step is the calculation of the angular distribution of the reaction.

3. Data reduction

3.1 Angular distribution measurements

Angular distribution measurements were performed at the energies 16, 20, 25 and 29 MeV, by detecting both reaction products ^{3}He and ^{4}He at an angular range θ_{lab}= 16˚ to 34˚. This angular range corresponds in the center of mass system to $\theta_{c.m}$= 40˚ to 140˚. The ^{3}He and ^{4}He reaction products were well resolved via the ΔE - E technique, as can be seen in a typical bi-dimensional spectrum ΔE- E, in Figure 3.1. The red spot corresponds to ^{4}He, while the green spot corresponds to ^{3}He. The ^{4}He peak, that comes from the under study reaction, is sitting on the top of a continuous background originating from breakup processes on hydrogen and on carbon as well as from fusion reactions on carbon. The background reduction can be achieved via two methods. In the first method, which is finally adopted in our analysis, the background subtraction is made by placing the windows left and right to the "peak" in the two dimension spectrum which with the appropriate normalization to the peak area, gives the background counts. In a second scenario which is adopted only for one energy for reasons of comparison, the deduction of the background was obtained by using the data collected with the carbon target. In this respect alpha originating from reactions on carbon can be eliminated. Alpha originating from breakup on hydrogen are considered to be minimum and are not taken into account. This procedure follows in two steps: First the alpha of the reaction ^{6}Li + ^{12}C (Figure 3.3), are appropriately normalized in flux and scattering centers to the run with the CH_2 target (Figure 3.4). Subsequently they are subtracted from the alpha of the reaction ^{6}Li + p (Figure 3.2). The remaining alpha are those from the under study reaction (Figure 3.5.) The analysis of the last spectrum gives results in good agreement with the deduced via the first method. As the error here is larger than the first method, the last is adopted for the background analysis.

Our analysis includes the following steps.

- Single ^{4}He and ^{3}He single spectra are formed with the appropriate conditions in two dimensional spectra.
- The ^{4}He and ^{3}He peaks are integrated and relevant counts are extracted
- Taking into account the details of measurement, differential cross sections are formed

The differential cross sections for all beam energies are calculated via the formula:

$$\frac{d\sigma(\theta)}{d\Omega} = \frac{N(\theta)}{\Phi * \Omega * D} \qquad (3.1)$$

where:

$\frac{d\sigma}{d\Omega}$ is the differential cross section at angle θ, N are the number of counts per time at angle θ , Φ is the flux of the beam, Ω is the solid angle and D are the scattering centers of hydrogen. The solid angle was determined in chapter 2.3, while the flux of the beam was recorded in the Faraday cup. The accuracy of the flux intensity measurement was tested via the scattering measurement of ^{6}Li on hydrogen, recorded in MAGNEX [30], where the scattering was considered to be Rutherford. The differential cross sections are extracted in units of mbarn per steradian as long as the flux is expressed in particles per time, the solid angle in steradian, and the scattering centers in atoms per cm^2. This quantity has to be multiplied by 10^{27} as 1 mbarn=10^{-27}cm^2.

The error of the differential cross section in the laboratory system is calculated according to the formula (3.2). For the error calculation, the errors which are adopted are the statistical error, a 5% error in the estimation of the target thickness, a 5% error in the measured integrated beam charge and a 7% error due to the solid angle measurement. The deduction of the differential cross section error is presented in appendix E.

$$\Delta\left(\frac{d\sigma}{d\Omega}\right)=\sqrt{\frac{N}{\left(\Omega*\Phi*D_{hyd.}\right)^2}+\left(\frac{N}{\Omega^2*\Phi*D_{hyd.}}*\sigma_{\Omega}\right)^2+2*\left(\frac{0.05*N}{\Omega*\Phi*D_{hyd.}}\right)^2} \qquad (3.2)$$

The obtained differential cross sections for all the beam energies are extensively presented in chapters 3.1.1 to 3.1.4.

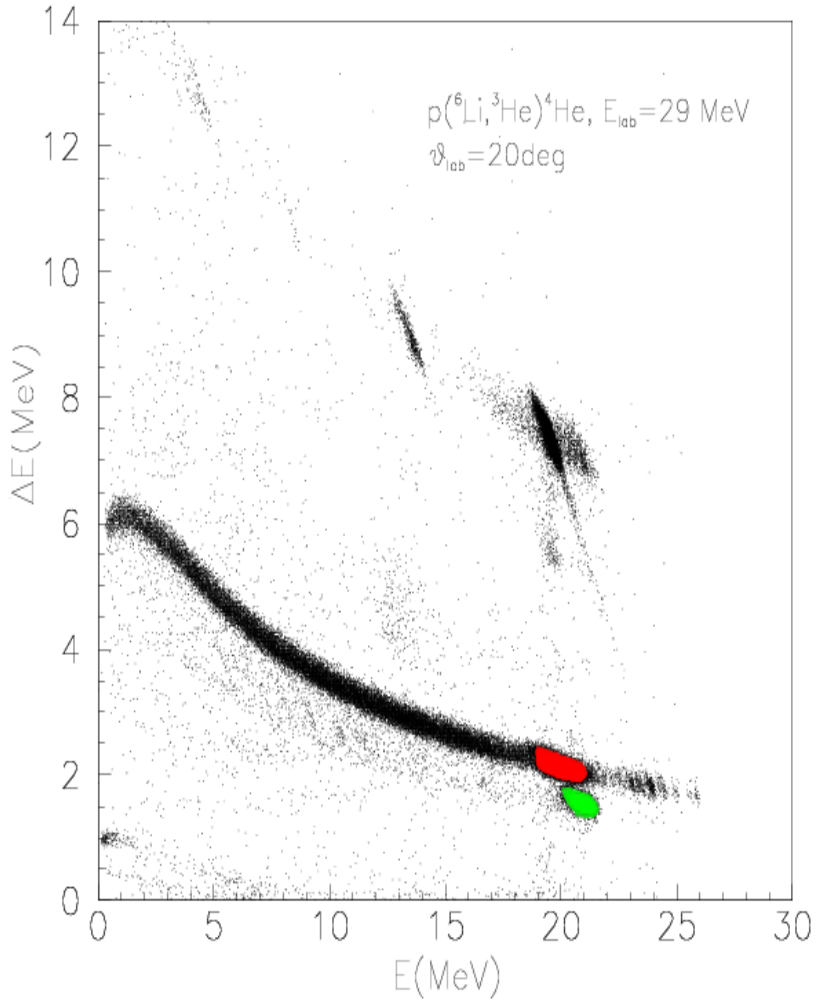

FIG. 3.1: A two dimensional spectrum ΔE-E collected at θ_{lab}=20˚ for the reaction ^{6}Li + p → ^{3}He + ^{4}He at bombarding energy 29 MeV. The red spot corresponds to ^{4}He and the green spot corresponds to ^{3}He.

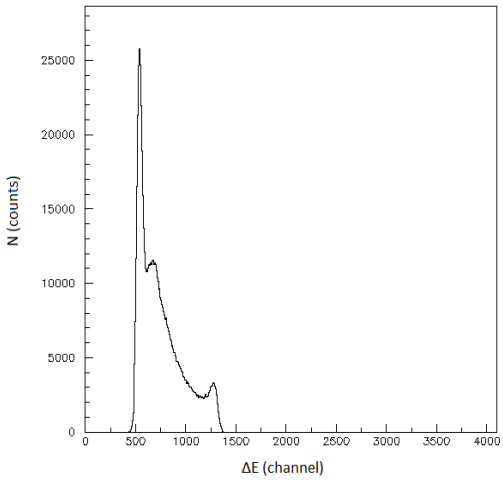

FIG. 3.2: One dimension ΔE spectrum collected at θ_{lab}=19˚, at bombarding energy 29 MeV and a CH_2 target.

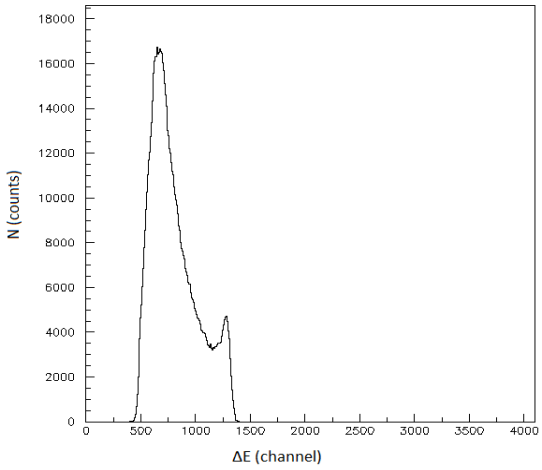

FIG. 3.3: Same as in Figure 3.2 but with a carbon target

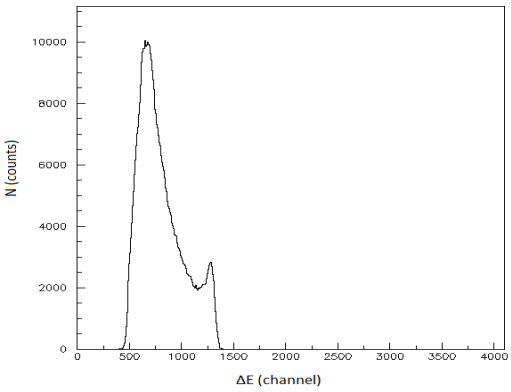

FIG. 3.4: Same as in 3.3 but normalized in flux and scattering centers to the CH_2 run

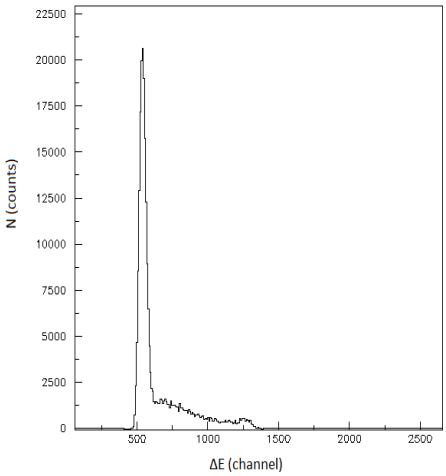

FIG. 3.5: Net spectrum after the subtraction between spectra of Figures 3.2 and 3.4. The observed peak represents the alpha's from the under study reaction $^{6}Li + p \rightarrow {}^{3}He + {}^{4}He$.

3.1.1 Angular distribution at E_{lab}=16 MeV

At the bombarding energy of 16 MeV, the differential cross section is calculated according to the formula (3.1) for the laboratory system and it is converted to the center of mass frame via the code in appendix C. The scattering centers of hydrogen are taken as $0.265012*10^{20}$ atoms/cm^2 and the flux of the beam is $3.38*10^{12}$ particles/sec as it was recorded in the Faraday cup. The counts of each strip are shown in Table T3.1 in appendix D. The differential cross section and the error for each strip are indicated in Table 3.1. The error of the differential cross section, in the laboratory system, is calculated according to the formula (3.2), which is deduced in appendix E.

TABLE 3.1.a: Differential cross sections in the laboratory and the center of mass frame as well as the associated error in the c.m system are given for each strip for the reaction product ^{4}He, at bombarding energy Elab=16 MeV.

	$\theta_{lab}(^\circ)$	$\theta_{c.m.}(^\circ)$	$\frac{d\sigma}{d\Omega}lab\left(mb/sr\right)$	$\frac{d\sigma}{d\Omega}cm\left(mb/sr\right)$	$\Delta\left(\frac{d\sigma}{d\Omega}cm\right)\left(mb/sr\right)$	error %
^{4}He	16.38	44.95	66.33	9.28	0.93	10.02
^{4}He	17.54	48.25	66.84	9.36	0.94	10.04
^{4}He	18.70	51.65	66.96	9.39	0.94	10.01
^{4}He	19.86	55.05	71.46	10.03	1.01	10.07
^{4}He	21.02	58.45	69.16	9.71	0.98	10.09
^{4}He	22.18	61.95	68.32	9.59	0.96	10.01
^{4}He	23.34	65.55	63.19	8.86	0.89	10.05
^{4}He	24.50	69.15	61.44	8.59	0.86	10.01
^{4}He	25.66	72.95	67.44	9.39	0.94	10.01
^{4}He	26.82	76.75	64.96	8.98	0.90	10.02
^{4}He	27.98	80.75	66.14	9.05	0.91	10.06
^{4}He	29.14	84.85	61.54	8.29	0.84	10.13
^{4}He	30.30	89.15	56.24	7.41	0.75	10.12
^{4}He	31.46	93.75	60.49	7.69	0.78	10.14

TABLE 3.1.b: Differential cross sections in the laboratory and the center of mass frame as well as the associated error in the c.m system are given for each strip for the reaction product ^{3}He, at bombarding energy Elab=16 MeV.

	$\theta_{lab}(^\circ)$	$\theta_{c.m.}(^\circ)$	$\frac{d\sigma}{d\Omega}lab\left(mb/sr\right)$	$\frac{d\sigma}{d\Omega}cm\left(mb/sr\right)$	$\Delta\left(\frac{d\sigma}{d\Omega}cm\right)\left(mb/sr\right)$	error %
^{3}He	33.78	101.25	33.26	7.50	0.76	10.13
^{3}He	32.62	104.05	31.98	7.14	0.72	10.08
^{3}He	31.46	106.95	33.97	7.51	0.76	10.12
^{3}He	30.30	109.75	33.69	7.38	0.75	10.16
^{3}He	29.14	112.55	35.05	7.61	0.77	10.12
^{3}He	27.98	115.35	34.93	7.51	0.76	10.12
^{3}He	26.82	118.15	37.45	7.98	0.81	10.15
^{3}He	25.66	120.95	37.46	7.92	0.80	10.10
^{3}He	24.50	123.65	36.63	7.68	0.78	10.15
^{3}He	23.34	126.45	36.91	7.68	0.77	10.03
^{3}He	22.18	129.15	41.04	8.47	0.85	10.04
^{3}He	21.02	131.85	42.18	8.65	0.87	10.06
^{3}He	19.86	134.55	43.23	8.80	0.89	10.11
^{3}He	18.70	137.25	46.34	9.38	0.95	10.13
^{3}He	17.54	139.95	47.02	9.46	0.95	10.04
^{3}He	16.38	142.65	51.58	10.32	1.04	10.08

The reaction product ^{3}He is observed from $\theta_{c.m.}$=101˚ to 143˚, while the ^{4}He from $\theta_{c.m.}$= 45˚ to 94˚. The differential cross sections are presented in Figure 3.6 and they are compared with previous measurements from Lin et al. [18] and from Elwyn et al. [20]. The data from Lin et al. are not in a good agreement with the data from Elwyn et al., but they seem to agree well with the present data at the more backward angles. At the more forward angles, the present data seem to be located between the two previous measurements. Finally, for the extraction of reaction cross sections, the differential cross sections are fitted by a sum of Legendre polynomials $\sum_{l=0}^{l} B_l P_l\left(\cos(\theta)\right)$. The best fit to the data (4 terms of Legendre polynomials) is

represented with the pink dotted-dashed line in Figure 3.6, while the blue solid line represents theoretical calculations for the determination of the reaction mechanism, performed by Dr N. G. Nicolis [43, 57] . In Figure 3.7 different fits to the data depending on 4, 5 and 7 terms in the sum of Legendre polynomials are represented for probing uncertainties due to the fit. The different fits give approximately the same reaction cross section with deviations no more than 2%, as it can be seen in Table 3.2, where the coefficients of the Legendre polynomials are presented. However, the shape of the fit with 7 terms differs from the shape of the fits with 4 and 5 terms, at the forward and at the background angles, but it cannot be verified as data exist only from $\theta_{c.m.}$=40˚ to 140˚. Subsequently an uncertainty band was formed for the angular distribution due to the statistical errors of the differential cross sections indicating an upper limit to the obtained uncertainty of the reaction cross section. The angular distribution of the reaction at 16 MeV, the best fit to the data and the uncertainty band are represented in Figure 3.8. The uncertainty band corresponds to a 10% error for the reaction cross section.

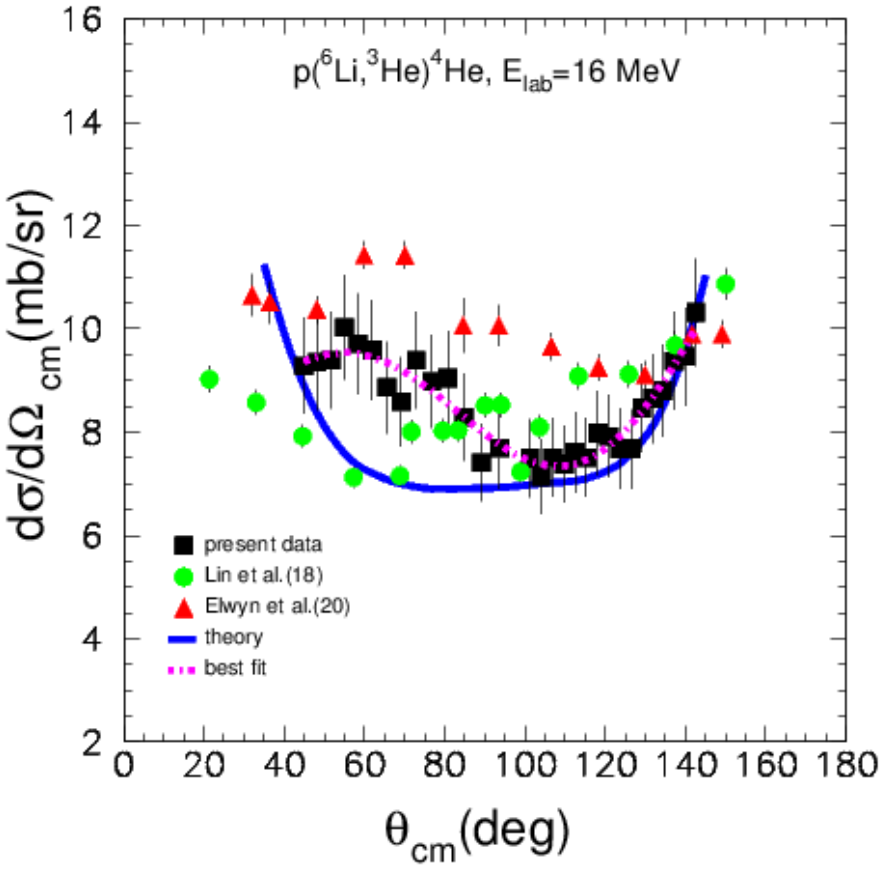

FIG. 3.6 Angular distribution data for the reaction ^{6}Li + p → ^{3}He + ^{4}He at bombarding energy 16 MeV (2.7 MeV/u) are compared with previous data [18,20], and with theoretical calculations performed by Dr N. G. Nicolis [43, 57] . The vertical error is due to a statistical error which is less than 1% and mainly due to an error 7% of the solid angle, 5% of the intensity of the beam and 5% of the thickness of the target. The horizontal error due to the angular uncertainty is approximately ±2˚ and is included in the size of the data points.

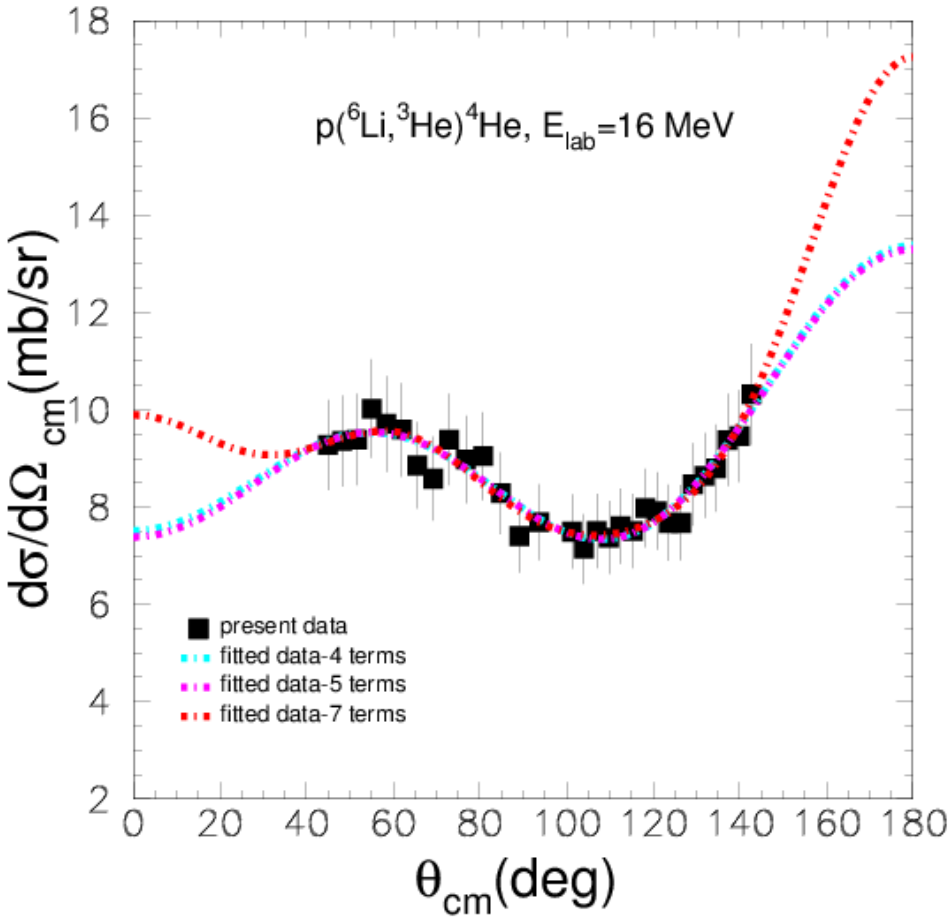

FIG. 3.7: Angular distribution data for the reaction $^{6}Li + p \rightarrow {}^{3}He + {}^{4}He$ at bombarding energy 16 MeV. The light blue dotted-dashed line represents the fourth order Legendre polynomial fit to the data, the pink dotted-dashed line represents the fifth order Legendre polynomial fit to the data, while the red dotted-dashed line represents the seventh order Legendre polynomial fit.

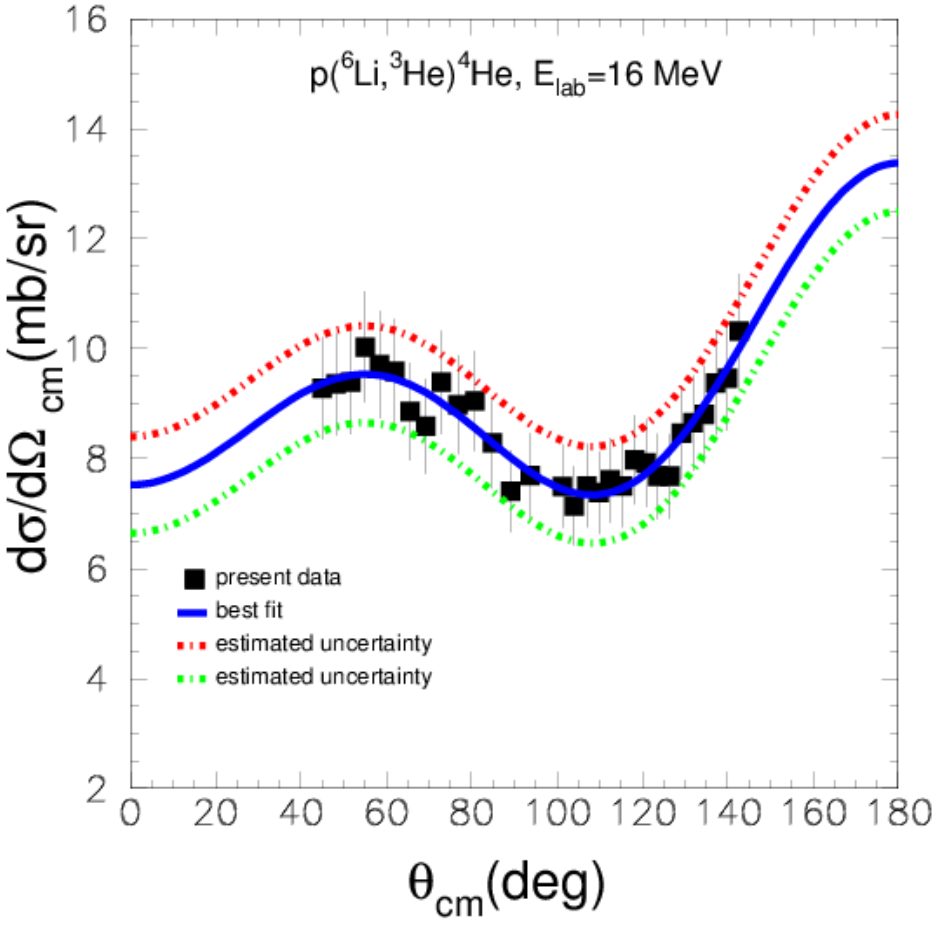

FIG. 3.8: Angular distribution data for the reaction $^{6}Li + p \rightarrow {}^{3}He + {}^{4}He$ at bombarding energy 16 MeV. The blue solid line represents the best fit to the data (fourth order Legendre polynomial fit), while the red and the green dotted-dashed lines define the uncertainty band for a 10% error to the reaction cross section -B_0 term of the Legendre polynomial.

TABLE 3.2: Values of coefficients B_L in the expansion of the differential cross section in the center of mass frame into a series of Legendre polynomials $d\sigma/d\Omega = \sum_{l=0}^{l} B_l P_l(\cos\theta)$ at bombarding energy 16 MeV.

	Bo	B1	B2	B3	B4	B5	B6	$\sigma_r = 4\pi Bo$ (mb)
4 terms	8.7938	-0.4002	1.6557	-2.5278				110
5 terms	8.7808	-0.4129	1.6099	-2.544	-0.0474			110
7 terms	9.0322	-0.5816	2.6729	-2.8275	1.1002	-0.2684	0.7720	113

The reaction cross section is calculated via the formula

$$\sigma = 4\pi B_0 \qquad (3.3)$$

where B_0 is the zero order coefficient from Legendre polynomials to which the data are fitted. The reaction cross section for the bombarding energy of 16 MeV is obtained by taking the mean value of the reaction cross sections coming from the fits with 4 terms, 5 terms and 7 terms, while the standard deviation of the mean value is calculated according to the equation (3.4):

$$\sigma_{\sigma_r} = \sqrt{\frac{\sum_{i=1}^{3}\left(\sigma_{r_i} - \overline{\sigma_r}\right)^2}{N-1}} \qquad (3.4)$$

Therefore, the mean value of the reaction cross section, at bombarding energy 16 MeV, is 111 mb and the standard deviation of the mean value is 2 mb. This error is modified quadratically due to the statistical uncertainty (upper limit of 10%) of the measured differential cross sections.

3.1.2 Angular distribution at E_{lab}=20 MeV

At the bombarding energy of 20 MeV, the differential cross section is calculated according to the formula (3.1) for the laboratory system and it is converted to the center of mass frame via the code in appendix C. The scattering centers of hydrogen are $0.42075*10^{20}$ atoms/cm^2 and the flux of the beam is $30.35*10^{12}$ particles/sec as it was recorded in the Faraday cup. The counts of each strip are shown in the Table T3.2 in appendix D. The differential cross section and the error for each strip are shown in Table 3.3. The error of the differential cross section in the laboratory system, is calculated according to the formula (3.2), which is deduced in appendix E.

TABLE 3.3.a: Differential cross sections in the laboratory and the center of mass frame as well as the associated error in the c.m system are given for each strip for the reaction product ^{4}He, at bombarding energy Elab=20 MeV.

	$\theta_{lab}(^\circ)$	$\theta_{cm}(^\circ)$	$\frac{d\sigma}{d\Omega}lab\left(mb/sr\right)$	$\frac{d\sigma}{d\Omega}cm\left(mb/sr\right)$	$\Delta\left(\frac{d\sigma}{d\Omega}cm\right)\left(mb/sr\right)$	Error %
^{4}He	17.54	50.75	98.95	12.55	1.26	10.04
^{4}He	18.70	54.35	100.48	12.73	1.27	9.98
^{4}He	19.86	57.95	94.30	11.92	1.19	9.98
^{4}He	21.02	61.65	99.82	12.58	1.26	10.02
^{4}He	22.18	65.45	90.44	11.34	1.14	9.98
^{4}He	23.34	69.35	85.30	10.62	1.06	9.98
^{4}He	24.50	73.35	84.54	10.42	1.04	9.98
^{4}He	25.66	77.45	88.11	10.71	1.07	9.99
^{4}He	26.82	81.85	96.61	11.51	1.15	9.99
^{4}He	27.98	86.35	98.47	11.39	1.14	10.01
^{4}He	29.14	91.25	92.52	10.25	1.03	10.05
^{4}He	30.30	96.65	97.87	10.12	1.02	10.08
^{4}He	31.46	102.85	100.87	9.22	0.93	10.09

TABLE 3.3.b: Differential cross sections in the laboratory and the center of mass frame as well as the associated error in the c.m system are given for each strip for the reaction product ^{3}He, at bombarding energy Elab=20 MeV.

	$\theta_{lab}(^\circ)$	$\theta_{cm}(^\circ)$	$\frac{d\sigma}{d\Omega}lab\left(mb/sr\right)$	$\frac{d\sigma}{d\Omega}cm\left(mb/sr\right)$	$\Delta\left(\frac{d\sigma}{d\Omega}cm\right)\left(mb/sr\right)$	Error %
^{3}He	33.78	97.05	45.57	9.27	0.93	10.03
^{3}He	32.62	100.15	44.87	9.07	0.91	10.03
^{3}He	31.46	103.25	44.94	9.02	0.91	10.09
^{3}He	30.30	106.35	44.81	8.94	0.90	10.07
^{3}He	29.14	109.35	46.01	9.11	0.91	9.99
^{3}He	27.98	112.35	45.86	9.01	0.90	9.99
^{3}He	26.82	115.25	46.68	9.11	0.91	9.99
^{3}He	25.66	118.25	46.90	9.09	0.91	10.01
^{3}He	24.50	121.15	47.43	9.13	0.91	9.97
^{3}He	23.34	124.05	48.83	9.34	0.94	10.06
^{3}He	22.18	126.85	52.67	10.00	1.00	10.00
^{3}He	21.02	129.75	52.70	9.95	1.00	10.05
^{3}He	19.86	132.55	55.32	10.38	1.04	10.02
^{3}He	18.7	135.35	58.05	10.83	1.08	9.97
^{3}He	17.54	138.25	60.77	11.28	1.13	10.02
^{3}He	16.38	141.05	64.02	11.82	1.18	9.98

The reaction product ^{3}He is observed from $\theta_{c.m.}$=97˚ to 141˚, while the ^{4}He from $\theta_{c.m.}$=47˚ to 103˚. At the angular region from $\theta_{c.m.}$=97˚ to 103˚(overlapping region), where data exist for both reaction products ^{3}He, ^{4}He, the differential cross sections present very good agreement between theirselves, as it can be seen in Table 3.4. The agreement of these differential cross sections indicates the accuracy of the subtraction of the background for ^{4}He. The differential cross sections are presented in Figure 3.9 and they are compared with previous measurements from Gould et al. [27]. The present results are not in a good agreement with them. Finally, for the extraction of the reaction cross sections, the differential cross sections are fitted by a sum of Legendre polynomials $\sum_{l=0}^{l} B_l P_l\left(\cos(\theta)\right)$. The best fit to the data (4 terms of Legendre

polynomials) is represented with the pink dotted-dashed line in Figure 3.9, while the blue solid line represents theoretical calculations for the determination of the reaction mechanism performed by Dr N.G. Nicolis [43,57]. In Figure 3.10, different fits to the data depending on 4, 5 and 7 terms in the sum of Legendre polynomials are represented for probing uncertainties due to the fit. The different fits give approximately the same reaction cross section with deviations no more than 6%, as it can be seen in Table 3.5, where the coefficients of the Legendre polynomials are presented. However, the shape of the fit with 7 terms differs from the shapes of the fit with 4 and with 5 terms, at the forward and at the background angles, but it cannot be verified, as data exist from $\theta_{c.m.}$=40˚ to 140˚. Subsequently, an uncertainty band is formed for the angular distribution due to the statistical errors of the differential cross sections corresponding to a 10% error to the reaction cross section. The angular distribution data of the reaction at 20 MeV, the best fit to the data and the uncertainty band are represented in Figure 3.11.

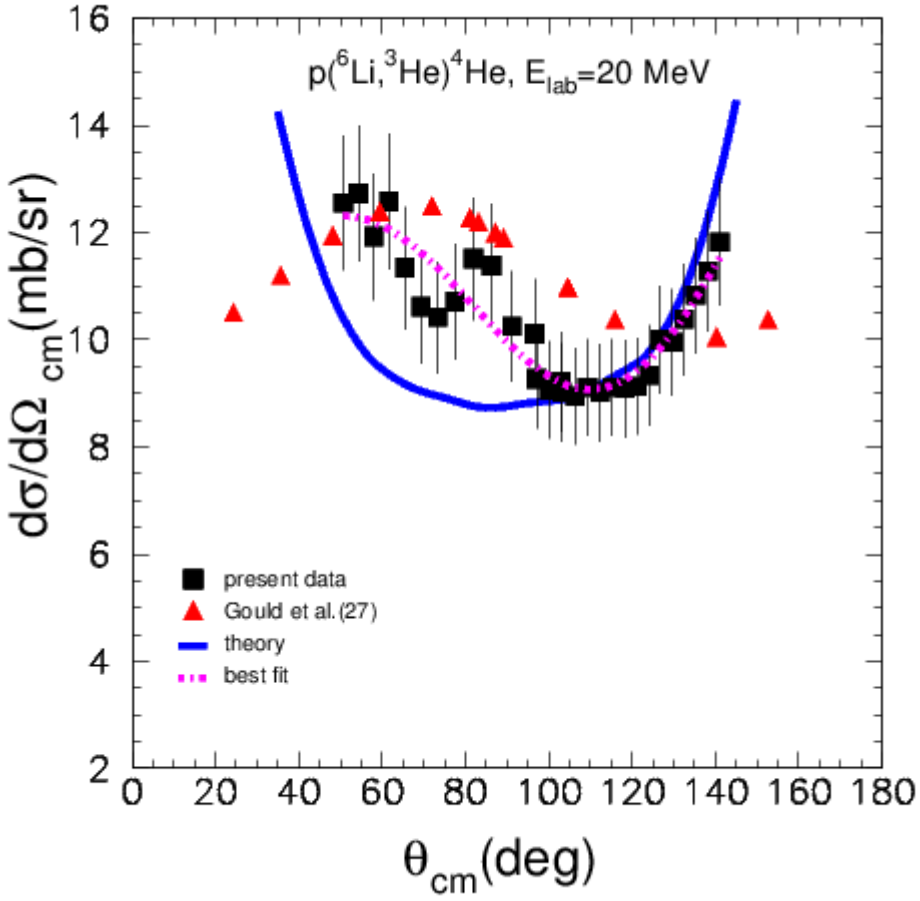

FIG. 3.9: Angular distribution data for the reaction ^{6}Li + p → ^{3}He + ^{4}He at bombarding energy 20 MeV (3.3 MeV/u) are compared with previous data [27] and with theoretical calculations performed by Dr N. G. Nicolis [43, 57] . The vertical error is due to a statistical error which is less than 1% and mainly due to an error 7% of the solid angle, 5% of the intensity of the beam and 5% of the thickness of the target. The horizontal error due to the angular uncertainty is approximately ±2˚ and is included in the size of the data points.

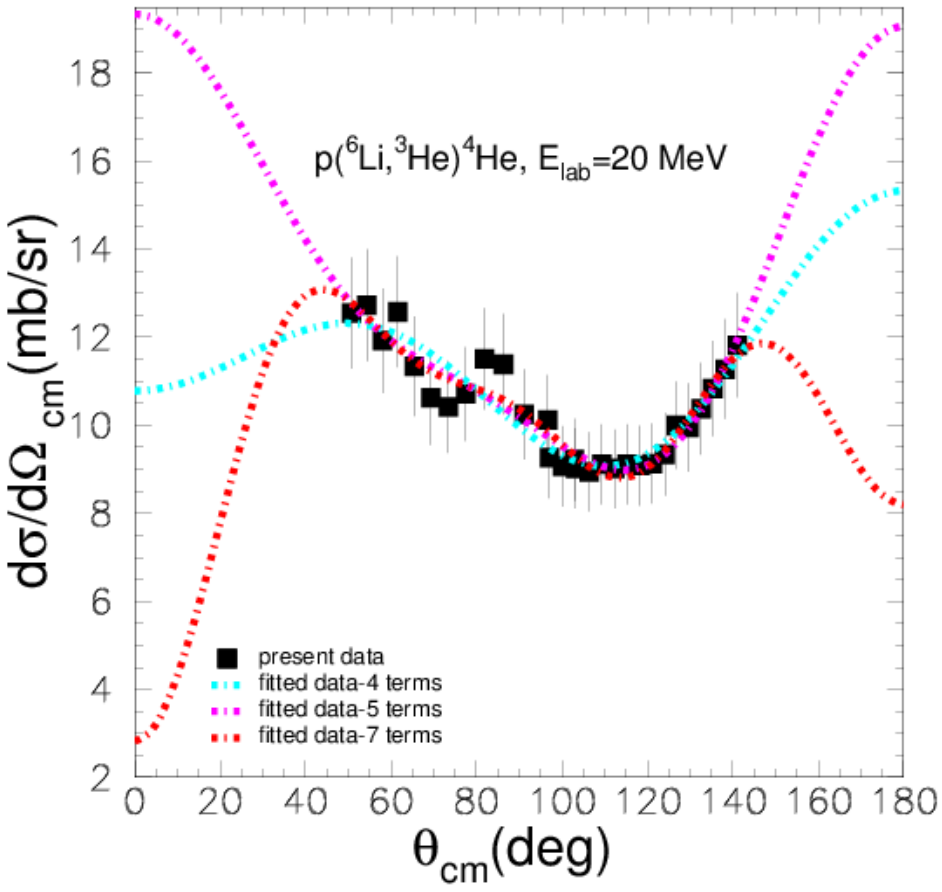

FIG. 3.10: Angular distribution data for the reaction $^{6}Li + p \rightarrow {}^{3}He + {}^{4}He$ at bombarding energy 20 MeV. The light blue dotted-dashed line represents the fourth order Legendre polynomial fit to the data, the pink dotted-dashed line represents the fifth order Legendre polynomial fit to the data, while the red dotted-dashed line represents the seventh order Legendre polynomial fit.

TABLE 3.4: Results of overlap angles in the center of mass frame at bombarding energy 20 MeV.

	$\left(\frac{d\sigma}{d\Omega}\right)_{c.m.}\left(mb/sr\right)$	
$\theta_{c.m.}$	^{3}He	^{4}He
96.65	9.27	10.12
100.15	9.07	9.61
102.85	9.02	9.22

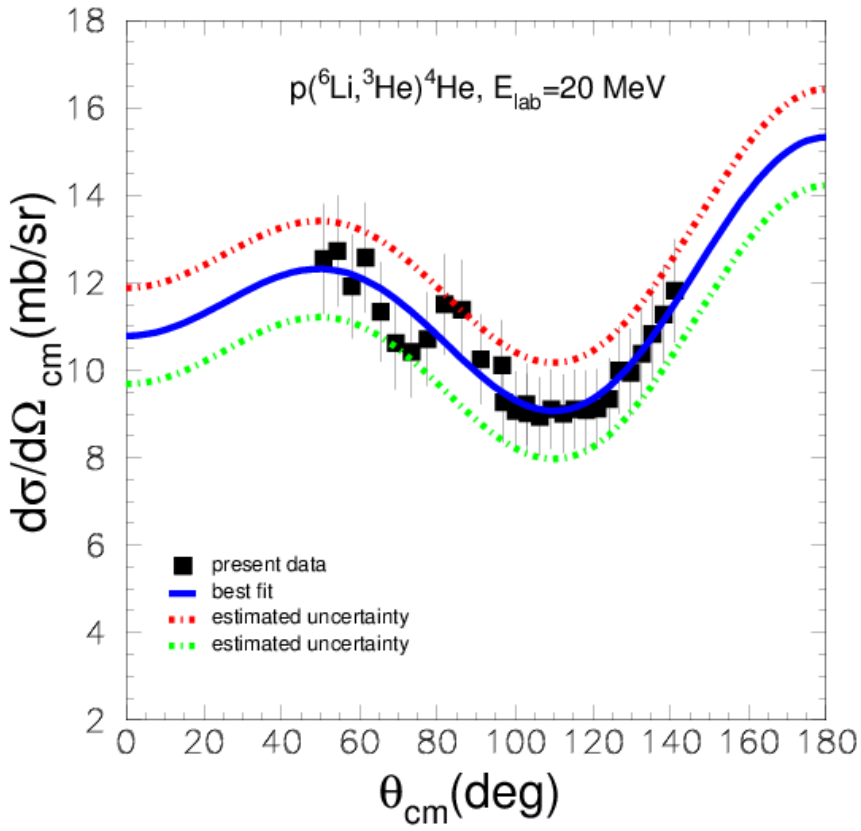

FIG. 3.11: Angular distribution data for the reaction $^{6}Li + p \rightarrow {}^{3}He + {}^{4}He$ at bombarding energy 20 MeV. The blue solid line represents the best fit to the data (fourth order Legendre polynomial fit), while the red and the green dotted-dashed lines define the uncertainty band for a 10% error to the reaction cross section -B_o term of the Legendre polynomial.

TABLE 3.5: Values of coefficients B_L in the expansion of the differential cross section in the center of mass frame into a series of Legendre polynomials $d\sigma/d\Omega = \sum_{l=0}^{l} B_l P_l (\cos\theta)$ at bombarding energy 20 MeV.

	Bo	B1	B2	B3	B4	B5	B6	$\sigma_r = 4\pi Bo$ (mb)
4 terms	10.9942	0.4164	2.0624	-2.6890				138
5 terms	11.8187	1.5650	5.0302	-1.4286	2.3541			148
7 terms	10.5673	0.5643	0.0606	-2.7372	-2.5635	-0.5104	-2.5462	133

For each fit the reaction cross section is calculated according to the equation (3.3), where B_0 is the zero order coefficient from Legendre polynomials to which the data are fitted. The final reaction cross section for the bombarding energy of 20 MeV is obtained by taking the mean

value of the reaction cross sections coming from the fits with 4 terms, 5 terms and 7 terms, while the standard deviation of the mean value is calculated according to the equation (3.4).

Therefore, the adopted value for the reaction cross section of $^{6}Li + p \rightarrow {}^{3}He + {}^{4}He$, at bombarding energy 20 MeV, is 140 mb and the standard deviation of the mean value is 8 mb. This error is modified at most quadratically due to the statistical uncertainty (upper limit of 10%) of the measured differential cross sections.

3.1.3 Angular distribution at E_{lab}=25 MeV

At the bombarding energy of 25 MeV, the differential cross section is calculated according to the formula (3.1) for the laboratory system and it is converted to the center of mass frame via the code in appendix C . The scattering centers of hydrogen are $0.265012*10^{20}$ atoms/cm^2 and the flux of the beam is $15.53*10^{12}$ particles/sec as it was recorded in the Faraday cup. The counts of each strip are shown in the Table T3.3 in appendix D. The differential cross section and the error for each strip are indicated in Table 3.6. The error of the differential cross section in the laboratory system is calculated according to the formula (3.2), which is deduced in appendix E.

TABLE 3.6.a: Differential cross sections in the laboratory and the center of mass frame as well as the associated error in the c.m system are given for each strip for the reaction product ^{4}He, at bombarding energy Elab=25 MeV.

	$\theta_{lab}(^\circ)$	$\theta_{c.m}(^\circ)$	$\frac{d\sigma}{d\Omega}lab\left(mb/sr\right)$	$\frac{d\sigma}{d\Omega}cm\left(mb/sr\right)$	$\Delta\left(\frac{d\sigma}{d\Omega}cm\right)\left(mb/sr\right)$	Error %
^{4}He	16.38	49.55	103.10	11.93	1.19	9.97
^{4}He	18.70	57.15	111.30	12.78	1.28	10.02
^{4}He	19.86	61.05	111.11	12.67	1.27	10.02
^{4}He	21.02	65.05	105.03	11.88	1.19	10.02
^{4}He	22.18	69.25	115.40	12.91	1.29	9.99
^{4}He	23.34	73.45	103.59	11.41	1.14	9.99
^{4}He	24.50	77.95	112.61	12.13	1.22	10.06
^{4}He	25.66	82.65	117.63	12.29	1.23	10.01
^{4}He	26.82	87.75	117.05	11.70	1.17	10.00
$^{4}He,^{3}He$	27.98	92.85	80.34	9.62	1.05	10.91
^{4}He	29.14	99.75	105.22	8.68	0.87	10.02

TABLE 3.6.b: Differential cross sections in the laboratory and the center of mass frame as well as the associated error in the c.m system are given for each strip for the reaction product ^{3}He, at bombarding energy Elab=25 MeV.

	$\theta_{lab}(^\circ)$	$\theta_{c.m}(^\circ)$	$\frac{d\sigma}{d\Omega}lab\left(mb/sr\right)$	$\frac{d\sigma}{d\Omega}cm\left(mb/sr\right)$	$\Delta\left(\frac{d\sigma}{d\Omega}cm\right)\left(mb/sr\right)$	Error %
^{3}He	32.62	95.85	48.84	8.88	0.89	10.02
^{3}He	31.46	99.25	48.39	8.79	0.88	10.01
^{3}He	30.30	102.6	47.10	8.53	0.86	10.08
^{3}He	29.14	105.9	45.52	8.21	0.82	9.99
^{3}He	27.98	109.1	46.75	8.40	0.84	10.00
^{3}He	26.82	112.3	47.00	8.41	0.84	9.99
^{3}He	25.66	115.4	47.17	8.40	0.84	10.00
^{3}He	24.50	118.5	47.21	8.36	0.84	10.05
^{3}He	23.34	121.6	44.63	7.86	0.79	10.05
^{3}He	22.18	124.6	49.90	8.74	0.88	10.07
^{3}He	21.02	127.6	50.83	8.86	0.89	10.05
^{3}He	19.86	130.6	50.33	8.73	0.88	10.08
^{3}He	18.70	133.6	51.71	8.93	0.89	9.97
^{3}He	17.54	136.5	54.95	9.44	0.95	10.06
^{3}He	16.38	139.5	55.48	9.49	0.95	10.01

The reaction product ^{3}He is observed from $\theta_{c.m.}$=96˚ to 140˚, while the ^{4}He from $\theta_{c.m.}$=50˚ to 100˚. At the angular region from $\theta_{c.m.}$=96˚ to 100˚(overlapping region), where data exist for both reaction products ^{3}He, ^{4}He, the differential cross sections present an agreement between theirselves, as it can be seen in Table 3.7. The agreement of these differential cross sections indicates the accuracy of the subtraction of the background. The differential cross sections are presented in Figure 3.12 and they are compared with previous measurements from Gould et al. [27]. There is an agreement between the present data and the results from Gould et al..For the extraction of the reaction cross section, the differential cross sections are fitted by a sum of Legendre polynomials $\sum_{l=0}^{1} B_l P_l(\cos(\theta))$. The best fit to the data (4 terms of Legendre polynomials) is represented with the pink dotted-dashed line in Figure 3.12, while the blue

solid line represents theoretical calculations for the determination of the reaction mechanism, performed by Dr N.G. Nicolis [43,57]. In Figure 3.13 different fits to the data depending on 4, 5 and 7 terms in the sum of Legendre polynomials are represented for probing uncertainties due to the fit. The different fits give approximately the same reaction cross section with deviations no more than 5%, as it can be seen in Table 3.8, where the coefficients of the Legendre polynomials are indicated. The shape of the fit with 7 terms differs from the shapes of the fit with 4 terms and with 5 terms, at the forward and at the background angles, but it cannot be verified as data exist from $\theta_{c.m.}$=40˚ to 140˚. Subsequently, an uncertainty band is formed for the angular distribution due the statistical errors of the differential cross sections indicating an upper limit to the obtained uncertainty of the reaction cross section. The angular distribution of the reaction at 25 MeV, the best fit to the data and the uncertainty band are represented in Figure 3.14. The uncertainty band corresponds to a 10% error for the reaction cross section.

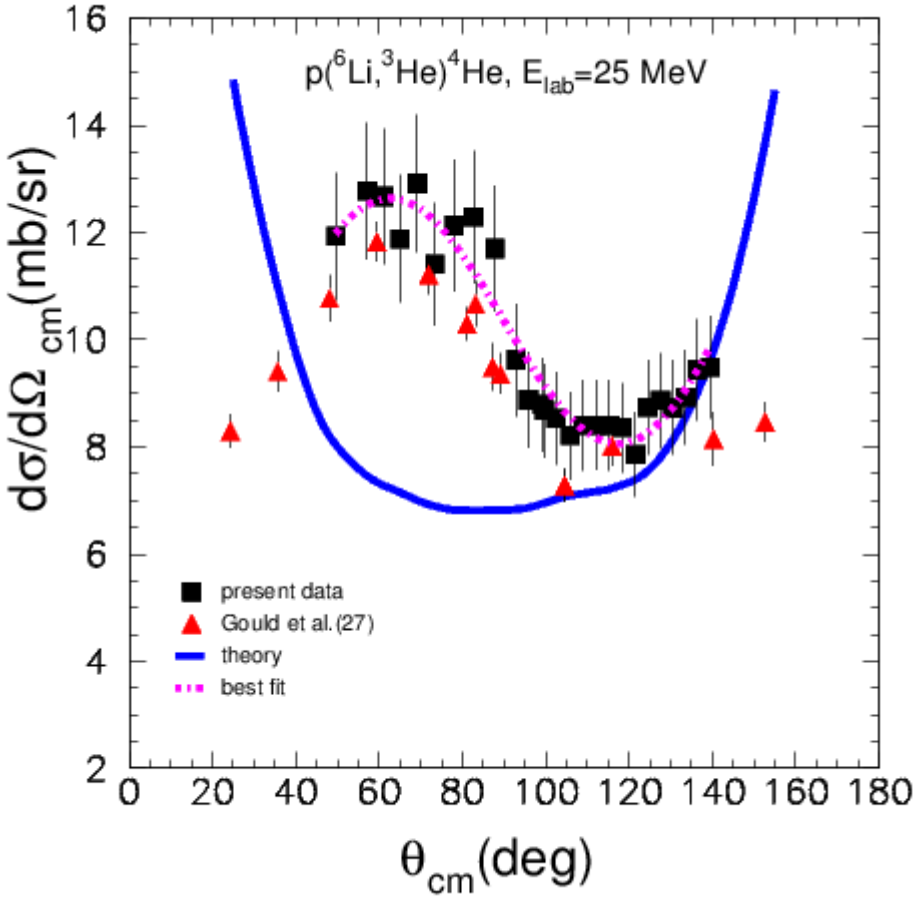

FIG. 3.12: Angular distribution data for the reaction ^{6}Li + p → ^{3}He + ^{4}He at bombarding energy 25 MeV (4.17 MeV/u) are compared with previous data [27] ,and with theoretical calculations performed by Dr N. G. Nicolis [43, 57]. The vertical error is due to a statistical error which is less than 1% and mainly due to an error 7% of the solid angle, 5% of the intensity of the beam and 5% of the thickness of the target. The horizontal error due to the angular uncertainty is approximately ±3˚ and is included in the size of the data points.

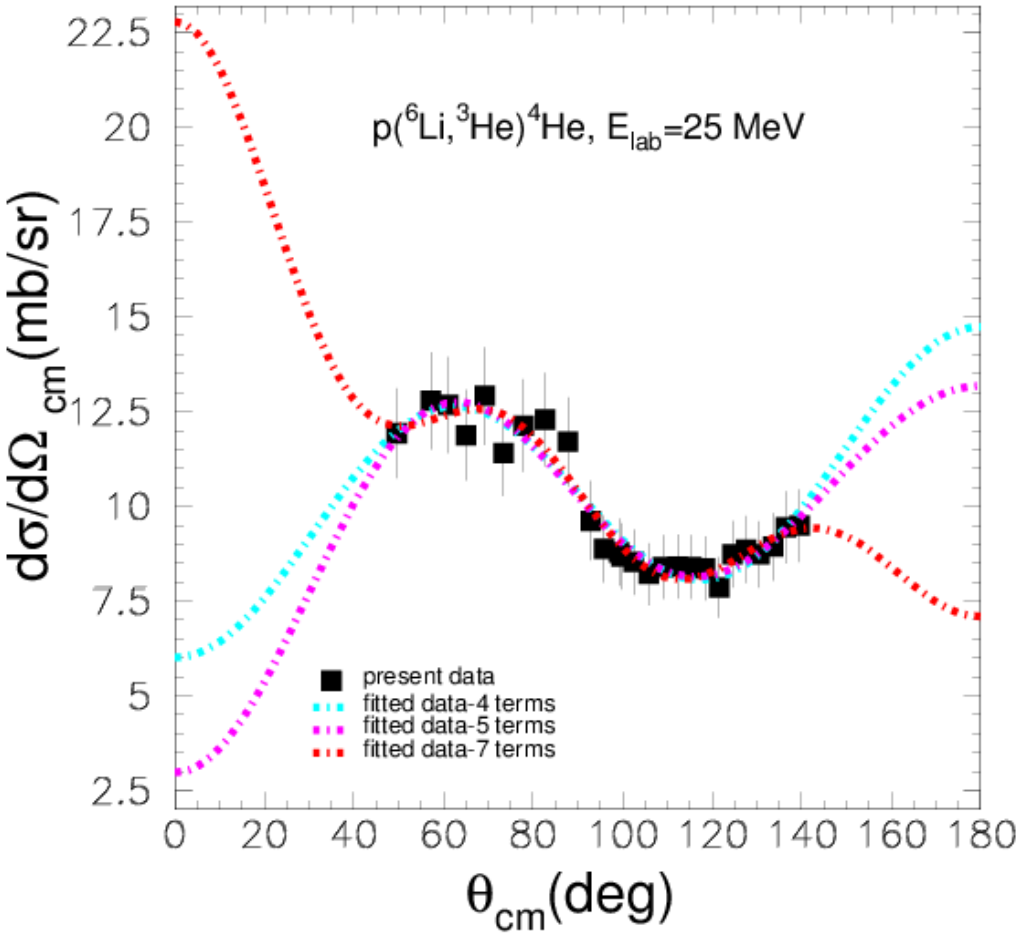

FIG. 3.13: Angular distribution data for the reaction $^{6}Li + p \rightarrow {}^{3}He + {}^{4}He$ at bombarding energy 25 MeV. The light blue dotted-dashed line represents the fourth order Legendre polynomial fit to the data, the pink dotted-dashed line represents the fifth order Legendre polynomial fit to the data, while the red dotted-dashed line represents the seventh order Legendre polynomial fit.

Table 3.7: Results of overlap angles in the center of mass frame at bombarding energy 25 MeV .

	$\left(\frac{d\sigma}{d\Omega}\right)_{c.m.}\left(mb/sr\right)$	
$\theta_{c.m.}$	^{3}He	^{4}He
99.25	8.79	8.68
95.85	8.88	9.21

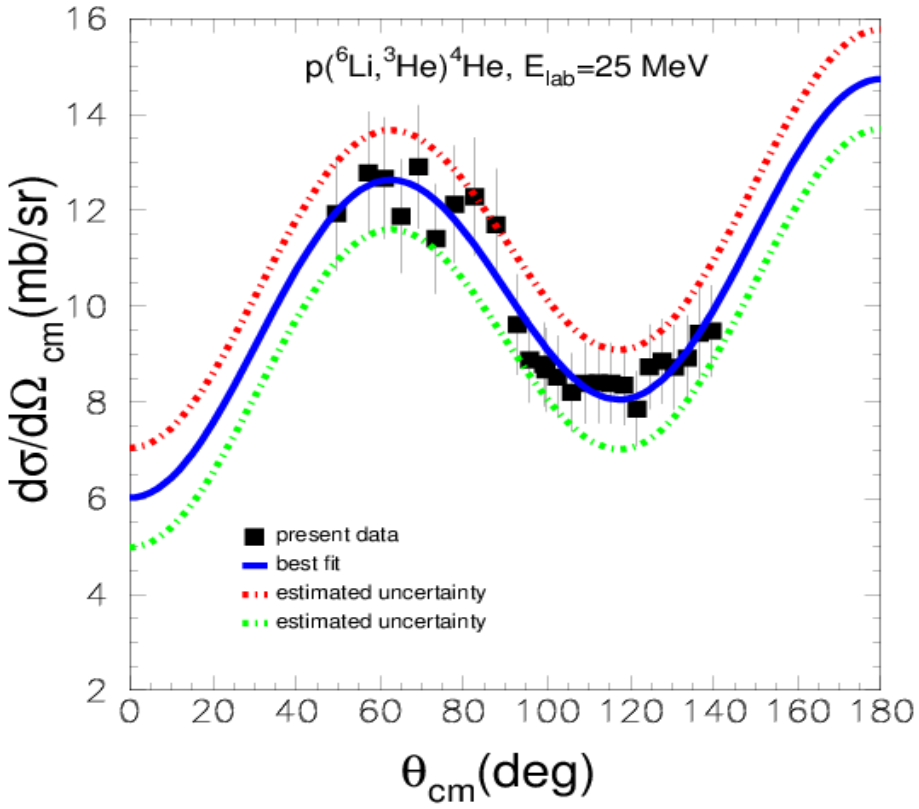

FIG. 3.14: Angular distribution data for the reaction $^{6}Li + p \rightarrow {}^{3}He + {}^{4}He$ at bombarding energy 25 MeV. The blue solid line represents the best fit to the data (fourth order Legendre polynomial fit), while the red and the green dotted-dashed lines define the uncertainty band for a 10% error to the reaction cross section -B_o term of the Legendre polynomial.

TABLE 3.8: Values of coefficients B_L in the expansion of the differential cross section in the center of mass frame into a series of Legendre polynomials $d\sigma/d\Omega = \sum_{l=0}^{L} B_l P_l(\cos\theta)$ at bombarding energy 25 MeV.

	Bo	B1	B2	B3	B4	B5	B6	$\sigma_r = 4\pi Bo$ (mb)
4 terms	10.3533	0.3762	0.0222	-4.7375				130
5 terms	10.0484	0.0248	-1.0789	-5.1221	-0.8903			126
7 terms	10.9398	4.0255	2.0707	0.5643	1.5891	3.2563	0.3341	137

The reaction cross section is calculated according to the equation (3.3), where B_0 is the zero order coefficient from Legendre polynomials to which data are fitted. The reaction cross section for the bombarding energy of 25 MeV is obtained by taking the mean value of the reaction cross sections coming from the fits with 4 terms, 5 terms and 7 terms, while the standard deviation of the mean value is calculated according to the equation 3.4.

Therefore, the mean value of the reaction cross section, at bombarding energy 25 MeV, is 131 mb and the standard deviation of the mean value is 6 mb. This error is modified quadratically at most by 10% due to the statistical uncertainty of the measured differential cross sections.

3.1.4 Angular distribution at E_{lab}=29 MeV

At the bombarding energy of 29 MeV, the differential cross section is calculated according to the formula (3.1) for the laboratory system and it is converted to the center of mass frame via the code in appendix C. The scattering centers of hydrogen are $0.265012*10^{20}$ atoms/cm^2 and the flux of the beam is $33.47*10^{12}$ particles/sec, as it was recorded in the Faraday cup. The counts of each strip are shown in the Table T3.4 in appendix D. The differential cross section and the error for each strip are indicated in Table 3.9. The error of the differential cross section in the laboratory system is calculated according to the formula (3.2) which is deduced in appendix E.

TABLE 3.9.a: Differential cross sections in the laboratory and the center of mass frame as well as the associated error in the c.m system are given for each strip for the reaction product ^{4}He, at bombarding energy Elab=29 MeV.

	$\theta_{lab}(^\circ)$	$\theta_{cm}(^\circ)$	$\frac{d\sigma}{d\Omega}lab\left(mb/sr\right)$	$\frac{d\sigma}{d\Omega}cm\left(mb/sr\right)$	$\Delta\left(\frac{d\sigma}{d\Omega}cm\right)\left(mb/sr\right)$	Error %
^{4}He	16.38	50.95	89.66	9.79	0.98	10.01
^{4}He	17.54	54.85	90.34	9.82	0.98	9.98
^{4}He	18.70	58.85	89.36	9.64	0.97	10.06
^{4}He	19.86	62.95	85.66	9.16	0.92	10.04
^{4}He	21.02	67.15	86.35	9.11	0.91	9.99
^{4}He	22.18	71.55	84.73	8.79	0.88	10.01
^{4}He	23.34	76.15	77.38	7.85	0.79	10.06
^{4}He	24.50	81.05	76.04	7.46	0.75	10.05
^{4}He	25.66	89.10	75.68	6.88	0.84	12.21
^{4}He	27.98	103.05	95.26	6.41	0.80	12.48

TABLE 3.9.b: Differential cross sections in the laboratory and the center of mass frame as well as the associated error in the c.m system are given for each strip for the reaction product ^{3}He, at bombarding energy Elab=29 MeV.

	$\theta_{lab}(^\circ)$	$\theta_{cm}(^\circ)$	$\frac{d\sigma}{d\Omega}lab\left(mb/sr\right)$	$\frac{d\sigma}{d\Omega}cm\left(mb/sr\right)$	$\Delta\left(\frac{d\sigma}{d\Omega}cm\right)\left(mb/sr\right)$	Error %
^{3}He	33.78	89.10	38.17	6.41	0.65	10.14
^{3}He	32.62	92.87	37.19	6.29	0.63	10.02
^{3}He	31.46	96.51	35.82	6.08	0.61	10.03
^{3}He	30.30	100.05	34.83	5.92	0.59	9.97
^{3}He	29.14	103.51	35.06	5.96	0.60	10.07
^{3}He	27.98	106.89	34.10	5.78	0.58	10.03
^{3}He	26.82	110.22	33.82	5.72	0.57	9.97
^{3}He	25.66	113.49	33.64	5.67	0.57	10.05
^{3}He	24.50	116.72	30.97	5.20	0.52	10.00
^{3}He	23.34	119.90	32.52	5.44	0.55	10.11
^{3}He	22.18	123.05	33.73	5.62	0.56	9.96
^{3}He	21.02	126.17	33.81	5.61	0.56	9.98
^{3}He	19.86	129.27	33.75	5.58	0.56	10.04
^{3}He	18.70	132.33	35.66	5.87	0.59	10.05
^{3}He	17.54	135.38	36.80	6.03	0.60	9.95
^{3}He	16.38	138.41	38.53	6.29	0.63	10.02

The reaction product ^{3}He is observed from $\theta_{c.m.}$=89˚ to 138˚, while the ^{4}He from $\theta_{c.m.}$=51˚ to 103˚. At the angular region from $\theta_{c.m.}$=89˚ to 103˚ (overlapping region), where data exist for both reaction products ^{3}He, ^{4}He, the differential cross sections present a good agreement between theirselves, as it can be seen in Table 3.10. The agreement of these differential cross sections indicates the accuracy of the subtraction of the background. The differential cross sections are presented in Figure 3.15 and they are compared with previous measurements from Gould et al. [27]. There is an agreement between the present data and the results from Gould et al. The differential cross sections are fitted by a sum of Legendre polynomials $\sum_{l=0}^{l} B_l P_l\left(\cos(\theta)\right)$. The best fit to the data (4 terms of Legendre polynomials) is represented

with the pink dotted-dashed line in Figure 3.15, while the blue solid line represents theoretical calculations for the determination of the reaction mechanism, performed by Dr N.G. Nicolis [43,57]. In Figure 3.16 different fits to the data depending on 4, 5 and 7 terms in the sum of Legendre polynomials are represented for probing uncertainties due to the fit. The different fits give approximately the same reaction cross section with deviations no more than 2%, as it can be seen in Table 3.11, where the coefficients of the Legendre polynomials are indicated. The shape of the fit with 7 terms differs from the shapes of the fit with 4 terms and with 5 terms, at the forward and at the background angles, but it cannot be verified as data exist from $\theta_{c.m.}$=40˚ to 140˚. Subsequently, an uncertainty band is formed for the angular distribution due to the statistical errors of the differential cross sections indicating an upper limit to the obtained uncertainty of the reaction cross section. The angular distribution of the reaction at 29 MeV, the best fit to the data and the uncertainty band are represented in Figure 3.17. The uncertainty band corresponds to a 10% error for the reaction cross section.

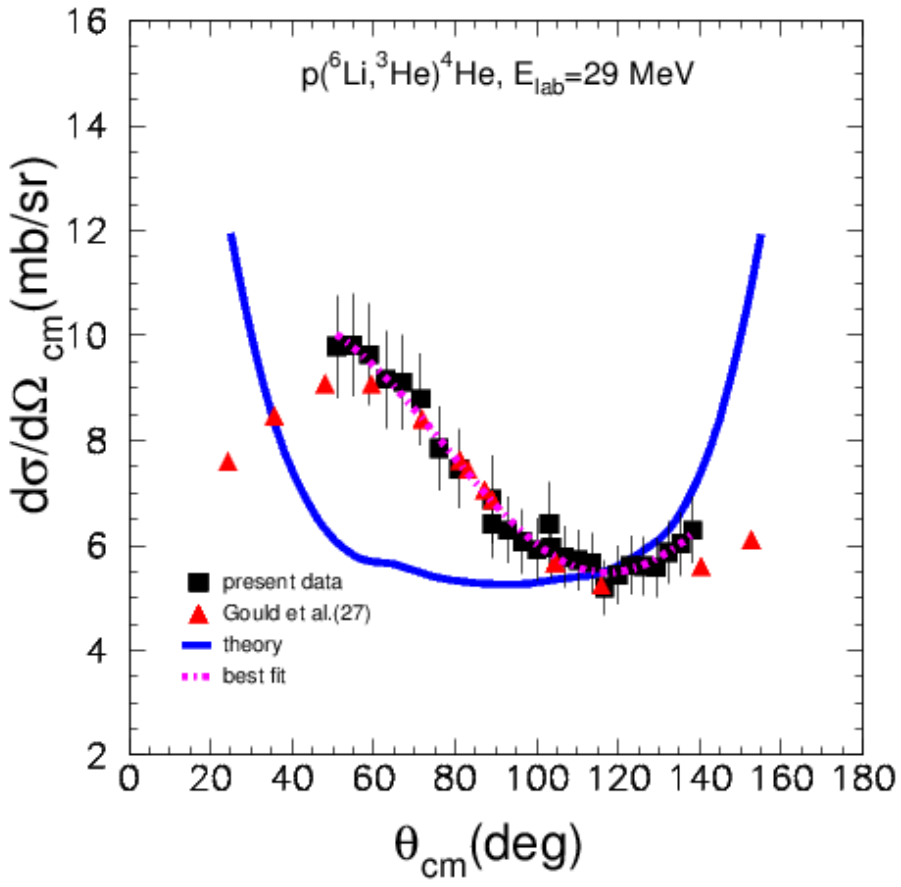

FIG. 3.15: Angular distribution data for the reaction ^{6}Li + p → ^{3}He + ^{4}He at bombarding energy 29 MeV (4.8 MeV/u) are compared with previous data [27] ,and with theoretical calculations performed by Dr N. G. Nicolis [43,57]. The vertical error is due to a statistical error which is less than 1% and mainly due to an error 7% of the solid angle, 5% of the intensity of the beam and 5% of the thickness of the target. The horizontal error due to the angular uncertainty is approximately ±3˚ and is included in the size of the data points.

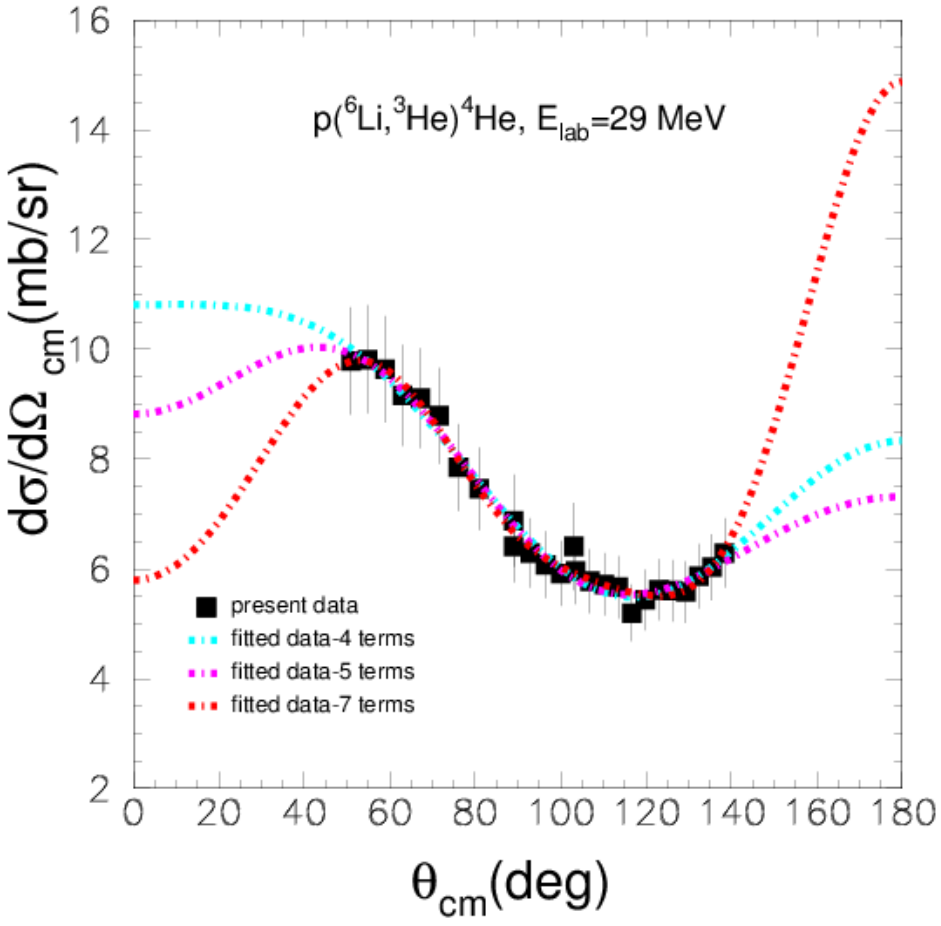

FIG. 3.16: Angular distribution data for the reaction $^{6}Li + p \rightarrow {}^{3}He + {}^{4}He$ at bombarding energy 29 MeV. The light blue dotted-dashed line represents the fourth order Legendre polynomial fit to the data, the pink dotted-dashed line represents the fifth order Legendre polynomial fit to the data, while the red dotted-dashed line represents the seventh order Legendre polynomial fit.

TABLE 3.10: Results of overlap angles in the center of mass frame at bombarding energy 29 MeV.

	$\left(\frac{d\sigma}{d\Omega}\right)_{c.m.}\left(mb/sr\right)$	
$\theta_{c.m.}$	^{3}He	^{4}He
89.10	6.41	6.88
96.51	6.08	6.41
103.05	5.96	6.65

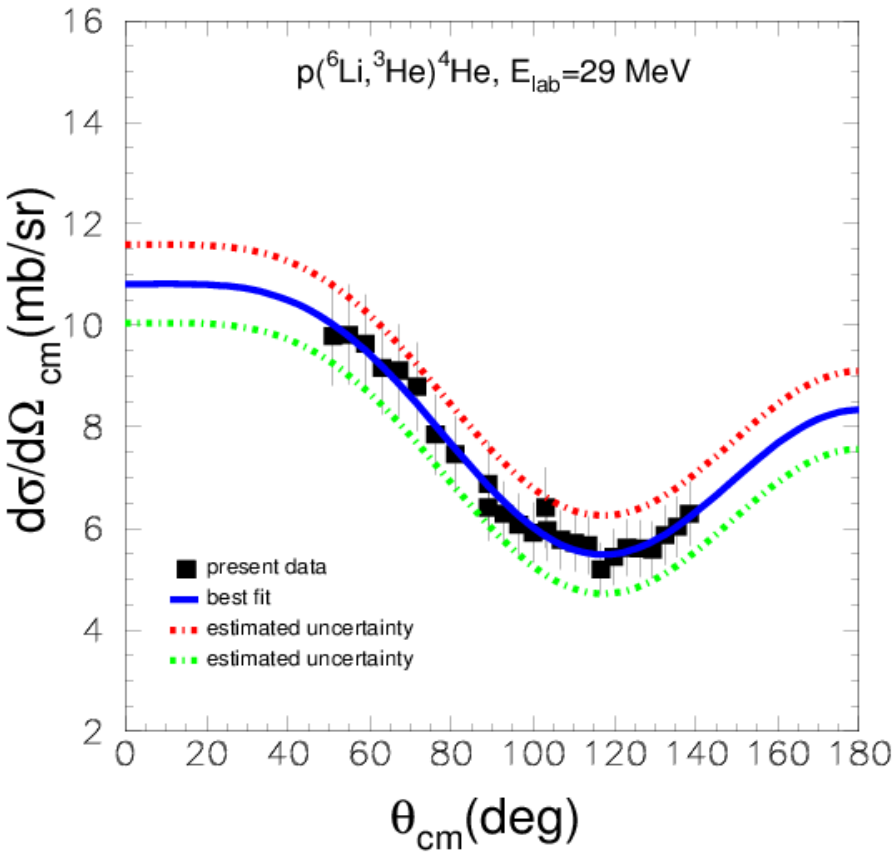

FIG. 3.17: Angular distribution data for the reaction $^{6}Li + p \rightarrow {}^{3}He + {}^{4}He$ at bombarding energy 29 MeV. The blue solid line represents the best fit to the data (fourth order Legendre polynomial fit), while the red and the green dotted-dashed lines define the uncertainty band for a 10% error to the reaction cross section -B_o term of the Legendre polynomials.

TABLE 3.11: Values of coefficients B_L in the expansion of the differential cross section in the center of mass frame into a series of Legendre polynomials $d\sigma/d\Omega = \sum_{l=0}^{l} B_l P_l (\cos\theta)$ at bombarding energy 29 MeV.

	Bo	B1	B2	B3	B4	B5	B6	$\sigma_r = 4\pi Bo$ (mb)
4 terms	7.6963	2.6744	1.8776	-1.4328				97
5 terms	7.4934	2.4400	1.1435	-1.6879	-0.5687			94
7 terms	7.5795	0.7995	1.6654	-4.0108	0.2813	-1.3325	0.8094	95

The reaction cross section is calculated according to the equation (3.3), where B_0 is the zero order coefficient from Legendre polynomials to which the data are fitted. The reaction cross section for the bombarding energy of 29 MeV is obtained by taking the mean value of the

reaction cross sections coming from the fits with 4 terms, 5 terms and 7 terms, while the standard deviation of the mean value is calculated according to the equation (3.4).

Therefore, the mean value of the reaction cross section, at bombarding energy 29 MeV, is 95 mb and the standard deviation of the mean value is 2 mb. This error is modified quadratically due to the statistical uncertainty (upper limit of 10%) of the measured differential cross sections.

3.2 Cross section of the reaction ^{6}Li + p → ^{4}He + ^{3}He

The differential cross sections, as it was described in chapters 3.1.1-3.1.4, are fitted to a sum of Legendre polynomials $d\sigma/d\Omega = \sum_{l=0}^{1} B_l P_l(\cos\theta)$ and the reaction cross sections are deduced as $\sigma = 4\pi B_0$. Different fits, depending on 4, 5 and 7 terms of Legendre polynomials, are performed for probing uncertainties due to the fit, and a reaction cross section is obtained for each fit. The final reaction cross section, is calculated as a mean of the values deduced during the various fits. The reaction cross sections and the standard deviations of the mean values are indicated in Table 3.12. It should be noted that the final associate uncertainty to the cross section will be deduced if we add in quadrature to the mean deviation the error due to the measurement uncertainty. An upper limit to this uncertainty was estimated to be 10%. Furthermore, the reaction cross sections as a function of energy between 2 to 5 MeV/u are displayed in Figure 3.18, and are compared with some sets of previous measurements [18-20, 23,24,27]. The present results clarify previous inconsistencies and combined with the Lin et al. data they possibly probe a broad new resonance at E_p=3.7 MeV. Except of the present reaction cross sections, the absorption cross sections σ_{CDCC} calculated by Prof. K. Rusek, and the cross sections for a compound production of ^{3}He and ^{4}He with the MECO code σ_{MECO} calculated by Dr. N. Nicolis, are presented in Table 3.12. It was found that the measured values exhaust most of the absorption cross section, indicating that the ^{6}Li + p → ^{4}He + ^{3}He reaction is the most prominent reaction in this energy range and it proceeds mostly via a compound mechanism.

TABLE 3.12: The mean value of the reaction cross sections and the standard deviations of the mean value , as well as the calculation for a compound production of ^{3}He and ^{4}He with the MECO code, σ_{MECO} and the absorption cross section (σ_{tot}- σ_{break}) via a CDCC calculation, σ_{CDCC} ,for bombarding energies 16 MeV, 20 MeV, 25 MeV and 29 MeV. The Q value of the reaction is Q=4.02 MeV.

E_{lab} (MeV)	$E_{c.m.}$(MeV)	E_p(MeV)	σ_r (mb)	σ_{MECO} (mb)	σ_{CDCC} (mb)
16	2.30	2.67	111±2	114	131
20	2.87	3.33	140±8	145	162
25	3.59	4.17	131±6	114	133
29	4.16	4.83	95±2	90	110

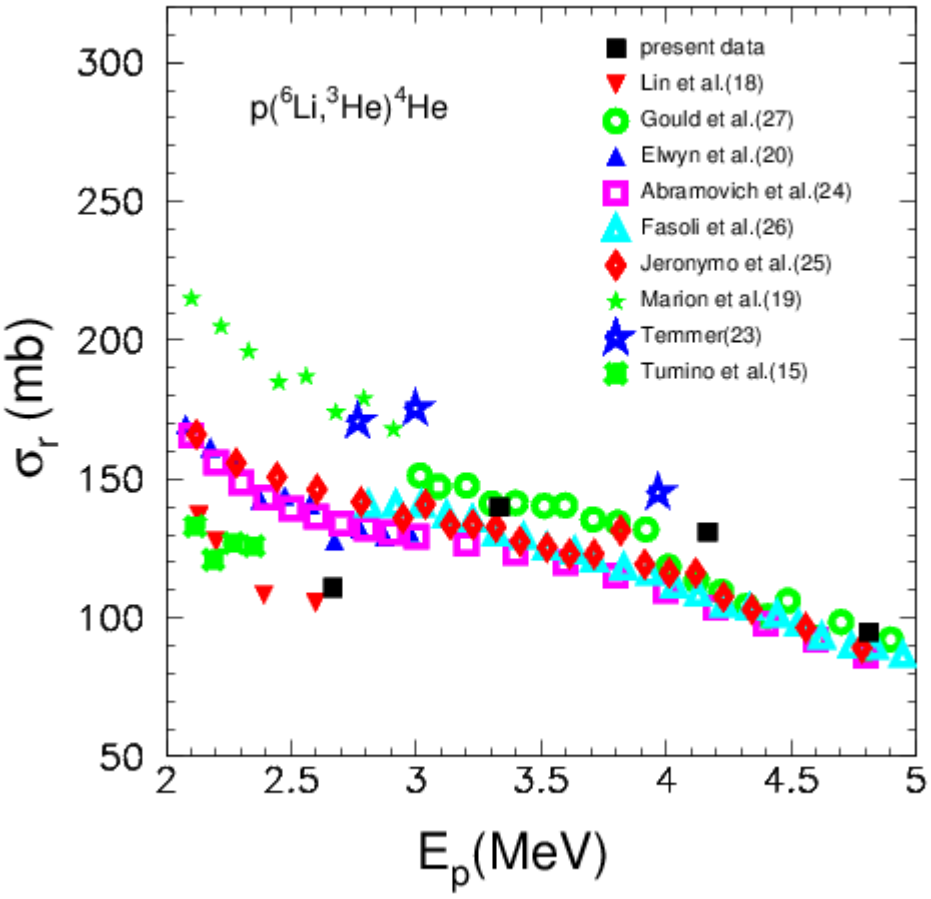

FIG. 3.18: Present reaction cross section measurements as a function of energy are designated with the boxes. Our values are compared with previous data from Refs. [18-20,23,24,27]. The data from the references [24,25] are not original experimental data, but evaluated ones.

3.3 Theoretical calculations

For the theoretical interpretation of the results, calculations in a Continuum Discretized Coupled Channel calculation framework (CDCC) were performed by Prof K. Rusek, Coupled Reaction Channel (CRC) were performed by Dr N. Keeley and compound calculations with the code MECO by Dr N. Nicolis. Some aspects of the calculations are given briefly below, pertinent in this work.

The absorption cross sections were determined previously and presented in Refs. [30,57]. That is the experimental data from the elastic scattering $^{6}Li + p \rightarrow {}^{6}Li + p$, were reproduced in a Continuum Discretized Coupled Channel calculation framework (CDCC) performed by Prof K. Rusek. In this respect, the total cross sections and the breakup cross sections were determined. The absorption cross sections were extracted as the differences between total reaction cross sections and breakup cross sections. The results are presented in table 3.12 and are compared with our experimental values and it is obvious that the presently measured reaction cross section exhaust most of the absorption cross section, indicating that the most prominent reaction in this energy range, is the one under study.

Further, Dr. N. Keeley carried out Coupled Reaction Channels (CRC) calculations for the $^{6}Li(p,{}^{3}He){}^{4}He$ reaction using the code FRESCO. The shape of these theoretical calculations is qualitatively similar to the shape of the angular distributions at the forward angles. They explain the broad peak which is centered at approximately $\theta_{c.m.}$=50 degrees and becomes more pronounced as the energy beam increases, indicating that there is a small contribution from direct mechanism. However, no quantitative results were obtained as it was found that the results were very sensitive to details of the input to the calculations, particularly the exit channel $^{3}He + {}^{4}He$ optical potential, which seems to be poorly known.

The compound nucleus decay was calculated with the equilibrium statistical model of nuclear reactions. For that purpose, the statistical model Monte-Carlo code MECO (Multisequential Evaporation COde) was employed by Dr N. G. Nicolis[43]. Angular distributions of the emitted particles were calculated using orbital angular momentum values from the transmission coefficient array, responsible for the decay under consideration and they were in a good agreement with the present results at the backward angles. This indicates the strong presence of the compound mechanism. In the same context reaction cross sections were extracted [43,57] and they are compared with the present reaction cross section in table 3.12. It was found that the $^{6}Li + p \rightarrow {}^{4}He + {}^{3}He$ reaction, which is the most prominent reaction in this energy range, proceeds mostly via a compound mechanism and the excellent agreement between the compound model calculations and the present data sets at the backward angles, support the inter consistency of all data recorded and analyzed in this experiment.

4. Summary and Conclusions

Angular distribution measurements were performed for the reaction ^{6}Li + p → ^{4}He + ^{3}He at energies 2.7, 3.3, 4.2 and 4.8 MeV/u at the Instituto Nazionali di Fisica Nucleare- Laboratori Nazionali del Sud in Catania (INFN-LNS), Italy. The ^{3}He and ^{4}He were both observed and they were well resolved via the ΔE-E technique, covering a wide angular range from $\theta_{c.m.}$ ~ 40° to 140°. In this respect differential cross sections were deduced at the above energies and were compared both with previous measurements and theoretical calculations. At higher energies the present data agreed well with previous measurements, while inconsistencies presented amongst previous data sets at 16 MeV, were partly clarified with the present results.

The comparison of experimental data and theory gave ground to useful conclusions for the reaction mechanism. At the backward angles the excellent agreement with theoretical calculations made by Dr. N. Nicolis with the code MECO, indicates the strong presence of the compound mechanism and precludes the validity of the Elwyn et al. [20] both in shape and intensity. However, comparing the theoretical predictions and the experimental data it is apparent a broad peak centered at approximately $\theta_{c.m.}$=50 degrees in disagreement with our compound calculations, which becomes more pronounced as the bombarding energy increases. This indicates an additional small contribution from direct mechanisms in addition to the compound one. The shape of the angular distribution at the forward angles was qualitatively similar to theoretical calculations made by Dr. N. Keeley with the code FRESCO in a coupled reaction channels (CRC) framework. However no quantitative results were obtained as it was found that the results were very sensitive to details of the input to the calculations, particularly the exit channel ^{3}He + ^{4}He optical potential, which seems to be poorly known.

The differential cross sections were finally fitted to a sum of Legendre polynomials $\sum_{l=0}^{1} B_l P_l(\cos(\theta))$ and the cross sections of the reaction were estimated according to the formula ($\sigma = 4\pi B_0$, where B_0 is the zero order Legendre coefficient). The present cross sections of the reaction were compared with some sets of previous excitation function measurements and they disclosed previous inconsistencies favoring the Lin et al. [18] results.

We should mention in that point, that in an excellent description of the elastic scattering channel of the reaction ^{6}Li+p in a Continuum Discretized Coupled Channel Calculation framework (CDCC) -calculations were performed by Prof. K. Rusek- absorption cross sections σ_{CDCC} were also extracted as the difference between the total cross section and the breakup cross section. These results were compared with our experimental values and it was found that the studied reaction exhausts almost all the absorption cross section indicating that the most prominent reaction in this energy range is the reaction ^{6}Li + p → ^{4}He + ^{3}He. Further, the excellent agreement of the compound model calculations with the data at backward angles, which take into account the above absorption cross sections extracted from the ^{6}Li + p elastic scattering channel support the inter consistency of all data recorded in the

LIPMAGNEX experiment which included measurements for elastic scattering and breakup with the MAGNEX Spectrometer and reaction measurements with the DINEX telescope.

Finally we should refer to the observation of a possible new resonance centered at E_p= 3.7 MeV.

References

[1] G.H. Miley, D. Driemeyer, Proceedings of the Review Meeting on Advanced-Fuel Fusion EPRIER-S36-SR (Electric Power Research Institute, Palo Alto-California, page 317, 1977).

[2] J.L. Hirshfied, Proceedings of the Review Meeting on Advanced-Fuel Fusion EPRIER-S36-SR (Electric Power Research Institute, Palo Alto-California, page 261, 1977).

[3] F.H. Southworth, Proceedings of the Review Meeting on Advanced-Fuel Fusion EPRIER-S36-SR (Electric Power Research Institute, Palo Alto-California, page 355, 1977).

[4] F.H. Southworth, Proceedings of the Review Meeting on Advanced-Fuel Fusion EPRIER-S36-SR (Electric Power Research Institute, Palo Alto-California, page 365, 1977).

[5] J.R. McNally, Jr., Proceedings of the Review Meeting on Advanced-Fuel Fusion EPRIER-S36-SR (Electric Power Research Institute, Palo Alto-California, page 197, 1977).

[6] J.L. Usher, J.R. Powell, S.Y. Hsieh, Proceedings of the Review Meeting on Advanced-Fuel Fusion EPRIER-S36-SR (Electric Power Research Institute, Palo Alto-California, page 69, 1977).

[7] J.A. Tombrello, Proceedings of the Review Meeting on Advanced-Fuel Fusion EPRIER-S36-SR (Electric Power Research Institute, Palo Alto-California, page 233, 1977).

[8] A.S. Blum, R.W. Moir, Proceedings of the Review Meeting on Advanced-Fuel Fusion EPRIER-S36-SR (Electric Power Research Institute, Palo Alto-California, page 83, 1977).

[9] J.A. Fillo, J.R. Powell, Proceedings of the Review Meeting on Advanced-Fuel Fusion EPRIER-S36-SR (Electric Power Research Institute, Palo Alto-California, page 57, 1977).

[10] J. R. MacNally, Nuclear Fusion 11, 187 (1971).

[11] B. W. Hooten and M. Ivanovich AERE Harwell Report No AERE-PR/NP18, 1972.

[12] C. Rolfs and W. S. Rodney W S Cauldrons in the Cosmos, Chicago, IL: University of Chicago Press, 1989.

[13] C. Rolfs and R. W. Kavanagh ; Nucl. Phys. **A 455**, 179(1986).

[14] J. Cruz, H. Luis, M. Fonseca, Z. Fulop, G. Gyurky, F. Raiola, M. Aliotta, K. U. Kettner, A. P. Jesus, J. P. Ribeiro, F. C. Barker, and C. Rolfs; Journal of Phys. **G 35**, 014004 (2008).

[15] A. Tumino, C. Spitaleri, L. Pappalardo, S. Cherubini, A. Del Zoppo, M. La Cognata, A. Musumarra, M.G. Pellegriti, R.G. Pizzone, A. Rinollo, S. Romano, and S. Typel; Nucl. Phys. **A 734**, 639 (2004).

[16] T. Shinozuka, Y. Tanaka and K. Sugihama, Nuclear Physics A326, 47, (1979).

[17] J. U. Kwon, J. C. Kim and B. N. Sung, Nuclear Physics A493, 112, (1989).

[18] Lin Chia-Shou, Hou Wan-Shou, Wen Min, Chou Jen-Chang; Nucl. Phys. **A 275**, 93 (1977).

[19] J. B. Marion, G. Weber, F. S. Mozer; Phys. Rev., **104**, 1402 (1956).

[20] A. J. Elwyn, R. E. Holland, C. N. Davids, L. Meyer-Schtzmeister, F. P. Mooring, and W. Ray, Jr.;Phys. Rev. **C 20**, 1984 (1979).

[21] G. P. Johnston and D. G. Sargood, Nucl. Phys. **A 224**, 349 (1974).

[22] A. Tumino, C. Spitareli, A. Di Pietro, P. Figuera, M. Lattuada, A. Musumarra, M. G. Pellegriti, R. G. Pizzone, S. Romano, C. Rolfs, S. Tudisco and S. Typel, Physical Review C 67, 065803, (2003).

[23] G. M. Temmer; Nuclear. Reaction Mechanisms Conference., Padua 1962, Italy, page 1013 (1962)

[24] S. N. Abramovich, B. Ja. Guzhovskij, V. A. Zherebcov, A. G. Zvenigorodskij ; Vop. At.Nauki i Tekhn., Ser.Yadernye Konstanty, 1984 Issue.4/58, 17 (1984)

[25] J. M. F. Jeronymo, G. S. Mani, A. Sadeghi, Nucl. Phys. **A 43**, 424 (1963).

[26] U. Fasoli, D. Toniolo and G. Zago, Phys. Lett. **B 8**, 127 (1964).

[27] C. R. Gould, R. O. Nelson, J. R. Williams, J. R. Boyce; Nuclear Science and Engineering, 55, 267 (1974).

[28] K. Schenk, M. Morike, G. Staudt, P. Turek, and D. Clement Phys. Lett. **52B**, 36 (1974).

[29] Michael F. Werby, M. B. Greenfield, K. W. Kemper, D. L. McShan and Steve Edwards, Physical Review C, 8, 1, (1973).

[30] V. Soukeras, A. Pakou, F. Cappuzzello, L. Acosta, C. Agodi, N. Alamanos, M. Bondi, D. Carbone, M. Cavallaro, A. Cunsolo, M. De Napoli, A. Di Pietro, J. P. Fernandez-Garcia P. Figuera, M. Fisichella, A. Foti, N. Keeley, G. Marquinez-Duran, I. Martel, M. Mazzocco, D. Nicolosi, D. Pierroutsakou, K. Rusek, O. Sgouros, E. Stiliaris, E. Strano, and D. Torresi; Physical Review. C 91, 057601, (2015).

[31] V. Soukeras, PhD thesis to appear 2016, University of Ioannina, Ioannina, Greece.

[32] A. Cunsolo, F. Cappuzzello, M. Cavallaro, A. Foti, A. Khouaja, S.E.A Orrigo, J.S. Winfield, L. Gasparini, G. Longo, T. Borello-Lewin, M.R.D Rodrigues, M.D.L. Barbosa, C. Nociforo and H. Petrascu; Eur. Phys. J. Special Topics 150, 343 (2007).

[33] A. Cunsolo, F. Cappuzzello, A. Foti, A. Lazzaro, A.L. Melita, C. Nociforo, V. Shchepunov and J.S. Winfield; NIM A 484, 56 (2002).

[34] A. Cunsolo, F. Cappuzzello, A. Foti, A. Lazzarro, A.L. Melita, C. Nociforo, V. Shchepunov and J.S. Winfield; NIM A 481, 48 (2002).

[35] Kenneth S. Krane, Introductory Nuclear Physics, John Wiley and Sons, New York, pages 378-431, 213-217 (1988).

[36] Samuel S. M. Wong, Introductory Nuclear Physics, Wiley- VCH Verlag GmbH & Co. KGaA, Weinheim, pages 280-286 (2004).

[37] G. R. Satchler, Introduction to nuclear reactions, Second Edition MacMillan Education LTD (1990).

[38] E. Gadioli and P. E. Hodgson, Pre-Equilibrium Nuclear Reactions, Clarendon Press, Oxford, pages 1-9, 97-182 (1992).

[39] Π. Α. Ασημακόπουλος, Εισαγωγή στην Πυρηνική Φυσική, Εκδόσεις Πανεπιστημίου Ιωαννίνων, 2η έκδοση, Ιωάννινα, σελίδες 259-272 (2005).

[40] A. J. Cole, Statistical Models for Nuclear Decay- From evaporation to vaporization, Institute of Physics Publishing, London, pages 111-138 (2000).

[41] Arthur Beiser, Concepts of Modern Physics, Sixth edition, McGraw-Hill Companies-International edition, pages 152-157, 359-363 (2003).

[42] Zerva Konstantina, PhD thesis, Optical potential and reaction mechanisms of weakly bound nuclei at near barrier energies, University of Ioannina, Ioannina- Greece, pages 9-14, (2013).

[43] N.G. Nicolis, Int. Jour. Mod. Phys. E17, 1541 (2008).

[44] V. F. Weiskopf, Phys. Rev. **52**, 195 (1937)

[45] M. A. Preston, Physics of the Nucleus, Addisson-Wesley Publishing Company (Reading Massachusetts, Palo Alto, London, 1962)

[46] Glenn F. Knoll, Radiation Detection and Measurement, third edition, John Wiley & Sons, New York, pages 353-403, (2000).

[47] W. R. Leo, Techniques for Nuclear and Particle Physics Experiments, second edition, Springer-Verlag, Berlin, pages 215-245 (1994).

[48] Marco Dragicevic, Master thesis: The new silicon strip detectors for the CMS Tracker Upgrade, University of technology, Vienna, pages 53-61 (2010).

[49] Victor Ratza, Master thesis: Development and test of a readout system for silicon strip detectors, Universidad Bonn, pages 17-22, (2012)

[50] E. Strano, A. Anastasio, M. Bettini, A. Boiano, C. Boiano, C. Cassese, L. Castellani, D. Corti, P. Di Meo, G. Galet, T. Glodariu, J. Grebosz, A. Gugleilmetti, M. La Commara, C. Manea, M. Mazzocco, P. Molini, M. Nicoletto, C. Parascadolo, L.Parascandolo, D. Pierroutsakou, G. Pontoriere, L. Roscilli, C. Signorini, F. Soramel, L. Stroe, M. Tessaro, N. Toniolo, D. Torresi, P. G. Zatti, Nuclear Instruments and Methods in Physics Research B 317, 657, (2013).

[51] G. Marquinéz- Durán, L. Acosta, R. Berjillos, J. A. Dueñas, J. A. Labrador, K. Rusek, A. M. Sanchéz- Benítez, I. Martel, Nuclear Instruments and Methods in Physics Research **A 755**, 69, (2014).

[52] G. Marquinéz- Durán, Master thesis: Dispersión Elástica del sistema ^{8}He + ^{208}Pb a energía E_{lab}= 22 MeV, Univeridad de Huelva, (2012).

[53] Lina Cekaite, Eivind Hoving, Havard H. Hauge, Nuclear Instruments and Methods in Physics Research A 527, 68, (2004).

[54] Claude Leroy and Pier Giorgio Rancoita, Silicon Solid State Devices and Radiation Detection, World Scientific Publishing CO, Singapore, pages 323, (2012).

[55] H. Park, H. J. Hyun, D. H. Kah, H. D Kang, H. J. Kim, Y. I Kim, Y. J. Kim and D. H Shim, Journal of the Korean Physical Society, 49, 4, 1401 (2006).

[56] Shin'ichiro Takeda, Tadayuki Takahashi, Shin Watanable, Hiroyasu Tajima, Takaaki Tanaka, Kazuhiro Nakazawa and Yasushi Fukazawa, Double Sided Silicon Strip detector for x-ray imaging, SPIE Newsroom, 10.1117/2.1200805.0889, (2008)

[57] Ch. Betsou, A. Pakou, F. Capuzzello, L. Acosta, C. Agodi, N. Alamanos, X. Aslanoglou, M. Bondi, D. Carbone, M. Cavallaro, A. Cunsolo, M. De Napoli, A. Di Pietro, J. P. Fernández-García, P. Figuera, M.Fisichella, A. Foti, N. Keeley, G. Marquinez-Duran, I. Martel, M. Mazzocco, N.G. Nicolis, D. Nicolosi, D. Pierroutsakou, K. Rusek, O. Sgouros, V. Soukeras, E. Stilliaris, E. Strano and D. Torresi, EPJA **A 51**: 86, (2015).

[58] Application Software group, Computer and Networks Division, CERN Program Library, PAW-Physics Analysis Workstation, CERN, Geneva, (1995).

[59] V. I. Zagrebaev et al, OM code of NRV, http://nrv.jinr.ru/nrv.

[60] O. B. Tarasov, D. Bazin, **NIM B.266**, 4657 (2008) .

[61] R.A. Broglia, A. Winther, Heavy Ion Reactions, Vol. I: Elastic and Inelastic Reactions, Benjamin Cummings, Redwood City, CA, (1981).

[62] J. B. Ball, Kinematics II: a no relativistic kinematics FORTRAN program to aid analysis of nuclear reaction angular distribution data, OAK RIDGE NATIONAL LABORATORY, page 24, (1962).

[63] J. B. Marion and F. C. Young, Nuclear Reaction Analysis- Graphs and tables, North- Holland publishing company- Amsterdam and Interscience Publishers- a division of John Wiley & Sons, INC.- New York, pages 140-142, (1968).

Appendix

A. Error calculation of solid angle Ω.

The solid angle is given according to the formula:

$$\Omega = \frac{N}{\Phi * D * \sigma_{Ruth.}}$$

where:

N are the number of counts, Φ is the flux of the beam, D are the scattering centers of gold, and $\sigma_{Ruth.}$ is the Rutherford cross section.

So the error of the solid angle is given by the relation:

$$\sigma_{\Omega} = \left[\left(\frac{\partial \Omega}{\partial N} * \sigma_N \right)^2 + \left(\frac{\partial \Omega}{\partial \sigma_{Ruth.}} * \sigma_{\sigma_{Ruth.}} \right)^2 + \left(\frac{\partial \Omega}{\partial \Phi} * \sigma_{\Phi} \right)^2 + \left(\frac{\partial \Omega}{\partial D} * \sigma_D \right)^2 \right]^{1/2} =$$

$$= \left[\left(\frac{1}{\Phi * D * \sigma_{Ruth.}} * \sigma_N \right)^2 + \left(-\frac{N}{\sigma_{Ruth.}^2 * \Phi * D} * \sigma_{\sigma_{Ruth.}} \right)^2 + \left(-\frac{N}{\Phi^2 * \sigma_{Ruth.} * D} * \sigma_{\Phi} \right)^2 + \left(-\frac{N}{D^2 * \sigma_{Ruth.} * \Phi} * \sigma_D \right)^2 \right]^{1/2} =$$

$$= \left(\frac{\sigma_N^2}{\sigma_{Ruth.}^2 * \Phi^2 * D^2} + \frac{N^2 * \sigma_{\Phi}^2}{\Phi^4 * \sigma_{Ruth.}^2 * D^2} + \frac{N^2 * \sigma_D^2}{D^4 * \sigma_{Ruth.}^2 * \Phi^2} \right)^{1/2} =$$

$$= \left[\frac{1}{\sigma_{Ruth.}^2 * \Phi^2 * D^2} * \left(\sigma_N^2 + \frac{N^2 * \sigma_{\Phi}^2}{\Phi^2} + \frac{N^2 * \sigma_D^2}{D^2} \right) \right]^{1/2} = \frac{1}{\sigma_{Ruth.} * \Phi * D} * \left(\sigma_N^2 + \frac{N^2 * \sigma_{\Phi}^2}{\Phi^2} + \frac{N^2 * \sigma_D^2}{D^2} \right)^{1/2}$$

However, the statistical error, the error in the estimation of the thickness of the target and the error in the flux of the beam are:

$$\sigma_N = \sqrt{N}\ ,\ \sigma_D = 0.05 * D,\ \sigma_{\Phi} = 0.05 * \Phi$$

Therefore,

$$\sigma_{\Omega} = \frac{1}{\sigma_{Ruth.} * \Phi * D} * \left(N + \frac{N^2 * \sigma_{\Phi}^2}{\Phi^2} + \frac{N^2 * \sigma_{D}^2}{D^2} \right)^{1/2} =$$

$$= \frac{1}{\sigma_{Ruth.} * \Phi * D} * \left(N + \frac{N^2 * (0.05 * \Phi)^2}{\Phi^2} + \frac{N^2 * (0.05 * D)^2}{D^2} \right)^{1/2} =$$

$$= \frac{1}{\sigma_{Ruth.} * \Phi * D} * \left(N + 2.5 * 10^{-3} * N^2 + 2.5 * 10^{-3} * N^2 \right)^{1/2} =$$

$$= \frac{1}{\sigma_{Ruth.} * \Phi * D} * \left(N + 5 * 10^{-3} * N^2 \right)^{1/2} \Rightarrow$$

$$\Rightarrow \quad \sigma_{\Omega} = \frac{1}{\sigma_{Ruth.} * \Phi * D} * \left(N + 0.005 * N^2 \right)^{1/2}$$

B. Calculation of Coulomb barrier

The Coulomb barrier is calculated via the Broglia program [61] written in C language:

```
#include<stdio.h>
#include<math.h>


double z1,z2,a1,a2,r1,r2,rf,rlab,cv1lab,cv1cm,cv2lab,cv2cm,ro;

int main(void){

printf("give the z1,z2,a1,a2,ro\n",z1,z2,a1,a2,ro);
scanf("%lf %lf %lf %lf %lf",&z1,&z2,&a1,&a2,&ro);

r1=ro*(pow(a1,0.333)+pow(a2,0.333));

r2=1.07*(pow(a1,0.333)+pow(a2,0.333))+2.72;

rlab=(a1+a2)/a2 ;
rf=1-0.63/r2;

cv1lab=1.44*z1*z2*rlab/r1;
cv1cm=1.44*z1*z2/r1;



cv2lab=rf*1.44*z1*z2*rlab/r2;
cv2cm=rf*1.44*z1*z2/r2;


printf(" coulomb barrier at lab: %lf   \n",cv1lab);
printf(" coulomb barrier at cm: %lf   \n",cv1cm);

printf("coulomb barrier according to Broglia at lab:%lf \n",cv2lab);
printf("coulomb barrier according to Broglia at cm:%lf \n",cv2cm);


return 0;
}
```

C. Transformation of the differential cross section from the laboratory system into the center of mass system.

The differential cross section is transformed from the laboratory system into the c.m. system, via the below code written in C language, which is based in references [62-63]. For the reaction product ^{3}He, the angles in the centre of mass system are obtained via the $\theta_{c.m.}=180 + \varphi$, where φ is the transformed angle in the c.m., presented by the code. For the reaction product ^{4}He, the angles in the c.m. system are obtained via the $\theta_{c.m.}=-\varphi$, where φ is the transformed angle in the c.m. presented by the code.

```
#include<stdio.h>
#include<math.h>

#define PI 3.14159265

int main(void){

int i,j;
double thetalab[16],thetacm1[16],thetalabrad[16],a[16],tetragono[16],riza[16],piliko[16],thetacm1rad[16],slab[16],scm[16];
double sinthetalabrad[16],costhetalabrad[16],m1,m2,m3,m4,Q,Elab,Eicm,g,arithmitis[16],paronomastis[16];

FILE *fp;

fp=fopen("data.txt","r");

for(i=0;i<16;i++){

fscanf(fp,"%lf %lf",&thetalab[i],&slab[i]);
}

fclose(fp);

printf("give m1,m2,m3,m4,Q,Elab \n");
scanf("%lf %lf %lf %lf %lf %lf", &m1,&m2,&m3,&m4,&Q,&Elab);

Eicm=(m2/(m1+m2))*Elab;

g=sqrt((m1*m3*(m3+m4)*Eicm)/(m2*m4*(m1+m2)*(Eicm+Q)));


FILE *out;

out=fopen("dataout.txt","w");
fprintf(out,"thetalab  thetacm  crosssection(lab)  crosssection(cm) \n");
for(j=0;j<16;j++){
```

```
thetalabrad[j]=(PI*thetalab[j])/180;

a[j]=tan(thetalabrad[j]);
tetragono[j]=pow(a[j],2);
riza[j]=sqrt(4+4*tetragono[j]*(1-pow(g,2)));
piliko[j]=(-2*g*tetragono[j]+riza[j])/(2*(tetragono[j]+1));


thetacm1rad[j]=acos(piliko[j]);
thetacm1[j]=thetacm1rad[j]*180/PI;

sinthetalabrad[j]=sin(thetalabrad[j]);
costhetalabrad[j]=cos(thetalabrad[j]);


arithmitis[j]=sqrt(1-(pow(g,2)*pow(sinthetalabrad[j],2)));
paronomastis[j]=pow((g*costhetalabrad[j]+arithmitis[j]),2);
scm[j]=(arithmitis[j]*slab[j])/paronomastis[j];


fprintf(out,"%.2f %.2f %.2f %.2f \n",thetalab[j],3.14-thetacm1[j],slab[j],scm[j]);

}

fclose(out);

return 0;
}
```

D. TABLES

Table T.3.1.a: Data for calculation of differential cross section at bombarding energy 16 MeV

	$\theta_{lab}(^{\circ})$	$\theta_{cm}(^{\circ})$	N (counts)	error N (counts)	Ω(sr)	error Ω(sr)	$\frac{d\sigma}{d\Omega}lab\left(mb/sr\right)$	$\frac{d\sigma}{d\Omega}cm\left(mb/sr\right)$	$\Delta\left(\frac{d\sigma}{d\Omega}cm\left(mb/sr\right)\right)$	error %
^{4}He	16.38	44.95	8612	93	0.00145	0.00010	66.33	9.28	0.93	10.02
^{4}He	17.54	48.25	10138	101	0.00169	0.00012	66.84	9.36	0.94	10.04
^{4}He	18.70	51.65	10584	103	0.00176	0.00012	66.96	9.39	0.94	10.01
^{4}He	19.86	55.05	11607	108	0.00181	0.00013	71.46	10.03	1.01	10.07
^{4}He	21.02	58.45	11460	107	0.00185	0.00013	69.16	9.71	0.98	10.09
^{4}He	22.18	61.95	11410	107	0.00186	0.00013	68.32	9.59	0.96	10.01
^{4}He	23.34	65.55	10946	105	0.00193	0.00014	63.19	8.86	0.89	10.05
^{4}He	24.50	69.15	10804	104	0.00196	0.00014	61.44	8.59	0.86	10.01
^{4}He	25.66	72.95	11893	109	0.00197	0.00014	67.44	9.39	0.94	10.01
^{4}He	26.82	76.75	11606	108	0.00199	0.00014	64.96	8.98	0.90	10.02
^{4}He	27.98	80.75	11948	109	0.00202	0.00014	66.14	9.05	0.91	10.06
^{4}He	29.14	84.85	11156	106	0.00202	0.00014	61.54	8.29	0.84	10.13
^{4}He	30.30	89.15	10458	102	0.00208	0.00015	56.24	7.41	0.75	10.12
^{4}He	31.46	93.75	11236	106	0.00207	0.00015	60.49	7.69	0.78	10.14

Table T.3.1.b: Data for calculation of differential cross section at bombarding energy 16 MeV

	$\theta_{lab}(^{\circ})$	$\theta_{cm}(^{\circ})$	N (counts)	error N (counts)	Ω(sr)	error Ω(sr)	$\frac{d\sigma}{d\Omega}lab\left(mb/sr\right)$	$\frac{d\sigma}{d\Omega}cm\left(mb/sr\right)$	$\Delta\left(\frac{d\sigma}{d\Omega}cm\left(mb/sr\right)\right)$	error %
^{3}He	33.78	101.3	4435	67	0.00149	0.00011	33.26	7.50	0.76	10.13
^{3}He	32.62	104.1	5904	77	0.00206	0.00015	31.98	7.14	0.72	10.08
^{3}He	31.46	107.0	6309	79	0.00207	0.00015	33.97	7.51	0.76	10.12
^{3}He	30.30	109.8	6265	79	0.00208	0.00015	33.69	7.38	0.75	10.16
^{3}He	29.14	112.6	6353	80	0.00202	0.00014	35.05	7.61	0.77	10.12
^{3}He	27.98	115.4	6309	79	0.00202	0.00014	34.93	7.51	0.76	10.12
^{3}He	26.82	118.2	6692	82	0.00199	0.00014	37.45	7.98	0.81	10.15
^{3}He	25.66	121.0	6605	81	0.00197	0.00014	37.46	7.92	0.80	10.10
^{3}He	24.50	123.7	6441	80	0.00196	0.00014	36.63	7.68	0.78	10.15
^{3}He	23.34	126.5	6394	80	0.00193	0.00014	36.91	7.68	0.77	10.03
^{3}He	22.18	129.2	6854	83	0.00186	0.00013	41.04	8.47	0.85	10.04
^{3}He	21.02	131.9	6990	84	0.00185	0.00013	42.18	8.65	0.87	10.06
^{3}He	19.86	134.6	7021	84	0.00181	0.00013	43.23	8.80	0.89	10.11
^{3}He	18.70	137.3	7325	86	0.00176	0.00013	46.34	9.38	0.95	10.13
^{3}He	17.54	140.0	7131	84	0.00169	0.00012	47.02	9.46	0.95	10.04
^{3}He	16.38	142.7	6696	82	0.00145	0.00010	51.58	10.32	1.04	10.08

Table T.3.2.a: Data for calculation of differential cross section at bombarding energy 20 MeV

	$\theta_{lab}(^{\circ})$	$\theta_{cm}(^{\circ})$	N (counts)	error N (counts)	Ω(sr)	error Ω(sr)	$\frac{d\sigma}{d\Omega}lab\left(mb/sr\right)$	$\frac{d\sigma}{d\Omega}cm\left(mb/sr\right)$	$\Delta\left(\frac{d\sigma}{d\Omega}cm\left(mb/sr\right)\right)$	error %
^{4}He	17.54	50.75	213966	463	0.00169	0.00012	98.95	12.55	1.26	10.04
^{4}He	18.70	54.35	226407	476	0.00176	0.00012	100.48	12.73	1.27	9.98
^{4}He	19.86	57.95	218353	467	0.00181	0.00013	94.30	11.92	1.19	9.98
^{4}He	21.02	61.65	235804	486	0.00185	0.00013	99.82	12.58	1.26	10.2
^{4}He	22.18	65.45	215325	464	0.00186	0.00013	90.44	11.34	1.14	9.98
^{4}He	23.34	69.35	210666	459	0.00193	0.00014	85.30	10.62	1.06	9.98
^{4}He	24.50	73.35	211927	460	0.00196	0.00014	84.54	10.42	1.04	9.98
^{4}He	25.66	77.45	221505	471	0.00197	0.00014	88.11	10.71	1.07	9.99
^{4}He	26.82	81.85	246064	496	0.00199	0.00014	96.61	11.51	1.15	9.99
^{4}He	27.98	86.35	253575	504	0.00202	0.00014	98.47	11.39	1.14	10.01
^{4}He	29.14	91.25	239099	489	0.00202	0.00014	92.52	10.25	1.03	10.05
^{4}He	30.30	96.65	259460	509	0.00208	0.00015	97.87	10.12	1.02	10.08
^{4}He	31.46	102.85	267098	517	0.00207	0.00015	100.87	9.22	0.93	10.09

Table T.3.2.b: Data for calculation of differential cross section at bombarding energy 20 MeV

	$\theta_{lab}(^{\circ})$	$\theta_{cm}(^{\circ})$	N (counts)	error N (counts)	Ω(sr)	error Ω(sr)	$\frac{d\sigma}{d\Omega}lab\left(mb/sr\right)$	$\frac{d\sigma}{d\Omega}cm\left(mb/sr\right)$	$\Delta\left(\frac{d\sigma}{d\Omega}cm\left(mb/sr\right)\right)$	error %
^{3}He	33.78	97.05	86620	294	0.00149	0.00011	45.57	9.27	0.93	10.03
^{3}He	32.62	100.15	118100	344	0.00206	0.00015	44.87	9.07	0.91	10.03
^{3}He	31.46	103.25	119000	345	0.00207	0.00015	44.94	9.02	0.91	10.09
^{3}He	30.30	106.35	118800	345	0.00208	0.00015	44.81	8.94	0.90	10.07
^{3}He	29.14	109.35	118900	345	0.00202	0.00014	46.01	9.11	0.91	9.99
^{3}He	27.98	112.35	118100	343	0.00202	0.00014	45.86	9.01	0.90	9.99
^{3}He	26.82	115.25	118900	345	0.00199	0.00014	46.68	9.11	0.91	9.99
^{3}He	25.66	118.25	117900	343	0.00197	0.00014	46.90	9.09	0.91	10.01
^{3}He	24.50	121.15	118900	345	0.00196	0.00014	47.43	9.13	0.91	9.97
^{3}He	23.34	124.05	120600	347	0.00193	0.00014	48.83	9.34	0.94	10.06
^{3}He	22.18	126.85	125400	354	0.00186	0.00013	52.67	10.00	1.00	10.00
^{3}He	21.02	129.75	124500	353	0.00185	0.00013	52.70	9.95	1.00	10.05
^{3}He	19.86	132.55	128100	358	0.00181	0.00013	55.32	10.38	1.04	10.02
^{3}He	18.70	135.35	130800	362	0.00176	0.00013	58.05	10.83	1.08	9.97
^{3}He	17.54	138.25	131400	362	0.00169	0.00012	60.77	11.28	1.13	10.02
^{3}He	16.38	141.05	118500	344	0.00145	0.00010	64.02	11.82	1.18	9.98

Table T.3.3.a: Data for calculation of differential cross section at bombarding energy 25 MeV

	$\theta_{lab}(^{\circ})$	$\theta_{cm}(^{\circ})$	N (counts)	error N (counts)	Ω(sr)	error Ω(sr)	$\frac{d\sigma}{d\Omega}lab\left(mb/sr\right)$	$\frac{d\sigma}{d\Omega}cm\left(mb/sr\right)$	$\Delta\left(\frac{d\sigma}{d\Omega}cm\left(mb/sr\right)\right)$	error %
^{4}He	16.38	49.55	61500	248	0.00145	0.00010	103.10	11.93	1.19	9.97
^{4}He	18.70	57.15	80825	284	0.00176	0.00012	111.30	12.78	1.28	10.02
^{4}He	19.86	61.05	82910	288	0.00181	0.00013	111.11	12.67	1.27	10.02
^{4}He	21.02	65.05	79960	283	0.00185	0.00013	105.03	11.88	1.19	10.02
^{4}He	22.18	69.25	88547	299	0.00186	0.00013	115.40	12.91	1.29	9.99
^{4}He	23.34	73.45	82447	287	0.00193	0.00014	103.59	11.41	1.14	9.99
^{4}He	24.50	77.95	90980	302	0.00196	0.00014	112.61	12.13	1.22	10.06
^{4}He	25.66	82.65	95300	309	0.00197	0.00014	117.63	12.29	1.23	10.01
^{4}He	26.82	87.75	96080	310	0.00199	0.00014	117.05	11.70	1.17	10.00
^{4}He	27.98	93.35	93500	306	0.00202	0.00014	112.66	10.50	1.05	10.00
^{4}He	29.14	99.75	87630	296	0.00202	0.00014	105.22	8.68	0.87	10.02

Table T.3.3.b: Data for calculation of differential cross section at bombarding energy 25 MeV

	$\theta_{lab}(^{\circ})$	$\theta_{cm}(^{\circ})$	N (counts)	error N (counts)	Ω(sr)	error Ω(sr)	$\frac{d\sigma}{d\Omega}lab\left(mb/sr\right)$	$\frac{d\sigma}{d\Omega}cm\left(mb/sr\right)$	$\Delta\left(\frac{d\sigma}{d\Omega}cm\left(mb/sr\right)\right)$	Error %
^{3}He	33.78	92.35	29430	172	0.00149	0.00011	48.04	8.73	0.88	10.08
^{3}He	32.62	95.85	41420	204	0.00206	0.00015	48.84	8.88	0.89	10.02
^{3}He	31.46	99.25	41290	203	0.00207	0.00015	48.39	8.79	0.88	10.01
^{3}He	30.30	102.6	40240	201	0.00208	0.00015	47.10	8.53	0.86	10.08
^{3}He	29.14	105.9	37910	195	0.00202	0.00014	45.52	8.21	0.82	9.99
^{3}He	27.98	109.1	38800	197	0.00202	0.00014	46.75	8.40	0.84	10.00
^{3}He	26.82	112.3	38580	196	0.00199	0.00014	47.00	8.41	0.84	9.99
^{3}He	25.66	115.4	38220	195	0.00197	0.00014	47.17	8.40	0.84	10.00
^{3}He	24.50	118.5	38140	195	0.00196	0.00014	47.21	8.36	0.84	10.05
^{3}He	23.34	121.6	35520	189	0.00193	0.00014	44.63	7.86	0.79	10.05
^{3}He	22.18	124.6	38290	196	0.00186	0.00013	49.90	8.74	0.88	10.07
^{3}He	21.02	127.6	38700	197	0.00185	0.00013	50.83	8.86	0.89	10.05
^{3}He	19.86	130.6	37560	194	0.00181	0.00013	50.33	8.73	0.88	10.08
^{3}He	18.70	133.6	37550	194	0.00176	0.00013	51.71	8.93	0.89	9.97
^{3}He	17.54	136.5	38290	196	0.00169	0.00012	54.95	9.44	0.95	10.06
^{3}He	16.38	139.5	33090	182	0.00145	0.0001	55.48	9.49	0.95	10.01

Table T.3.4.a: Data for calculation of differential cross section at bombarding energy 29 MeV

	$\theta_{lab}(^{\circ})$	$\theta_{cm}(^{\circ})$	N (counts)	Error N(counts)	Ω(sr)	error Ω(sr)	$\frac{d\sigma}{d\Omega}lab\left(mb/sr\right)$	$\frac{d\sigma}{d\Omega}cm\left(mb/sr\right)$	$\Delta\left(\frac{d\sigma}{d\Omega}cm\left(mb/sr\right)\right)$	Error %
^{4}He	16.38	50.95	115270	340	0.00145	0.00010	89.66	9.79	0.98	10.01
^{4}He	17.54	54.85	135687	368	0.00169	0.00012	90.34	9.82	0.98	9.98
^{4}He	18.70	58.85	139868	374	0.00176	0.00012	89.36	9.64	0.97	10.06
^{4}He	19.86	62.95	137777	371	0.00181	0.00013	85.66	9.16	0.92	10.04
^{4}He	21.02	67.15	141688	376	0.00185	0.00013	86.35	9.11	0.91	9.99
^{4}He	22.18	71.55	140120	374	0.00186	0.00013	84.73	8.79	0.88	10.01
^{4}He	23.34	76.15	132735	364	0.00193	0.00014	77.38	7.85	0.79	10.06
^{4}He	24.50	81.05	132413	364	0.00196	0.00014	76.04	7.46	0.75	10.05
^{4}He	25.66	86.25	156814	396	0.00197	0.00014	89.80	8.40	0.84	10.00
^{4}He	26.82	91.95	108897	330	0.00199	0.00014	61.55	5.35	0.54	10.09
^{4}He	27.98	98.65	186901	432	0.00202	0.00014	104.49	7.98	0.80	10.02
^{4}He	29.14	107.45	154512	393	0.00202	0.00014	86.08	4.83	0.48	9.94

Table T.3.4.b: Data for calculation of differential cross section at bombarding energy 29 MeV

	$\theta_{lab}(^{\circ})$	$\theta_{cm}(^{\circ})$	N (counts)	error N(counts)	Ω(sr)	error Ω(sr)	$\frac{d\sigma}{d\Omega}lab\left(mb/sr\right)$	$\frac{d\sigma}{d\Omega}cm\left(mb/sr\right)$	$\Delta\left(\frac{d\sigma}{d\Omega}cm\left(mb/sr\right)\right)$	Error %
^{3}He	33.78	89.10	50390	224	0.00149	0.00011	38.17	6.41	0.65	10.14
^{3}He	32.62	92.87	67980	261	0.00206	0.00015	37.19	6.29	0.63	10.02
^{3}He	31.46	96.51	65890	257	0.00207	0.00015	35.82	6.08	0.61	10.03
^{3}He	30.30	100.05	64140	253	0.00208	0.00015	34.83	5.92	0.59	9.97
^{3}He	29.14	103.51	62930	251	0.00202	0.00014	35.06	5.96	0.60	10.07
^{3}He	27.98	106.89	61000	247	0.00202	0.00014	34.10	5.78	0.58	10.03
^{3}He	26.82	110.22	59840	245	0.00199	0.00014	33.82	5.72	0.57	9.97
^{3}He	25.66	113.49	58740	242	0.00197	0.00014	33.64	5.67	0.57	10.05
^{3}He	24.50	116.72	53920	232	0.00196	0.00014	30.97	5.20	0.52	10.00
^{3}He	23.34	119.90	55790	236	0.00193	0.00014	32.52	5.44	0.55	10.11
^{3}He	22.18	123.05	55780	236	0.00186	0.00013	33.73	5.62	0.56	9.96
^{3}He	21.02	126.17	55470	236	0.00185	0.00013	33.81	5.61	0.56	9.98
^{3}He	19.86	129.27	54290	233	0.00181	0.00013	33.75	5.58	0.56	10.04
^{3}He	18.70	132.33	55810	236	0.00176	0.00013	35.66	5.87	0.59	10.05
^{3}He	17.54	135.38	55270	235	0.00169	0.00012	36.80	6.03	0.60	9.95
^{3}He	16.38	138.41	49540	223	0.00145	0.0001	38.53	6.29	0.63	10.02

Table T.3.5 Predicted energies (energy loss on ΔE detector and the remaining energy on E detector) for bombarding energy 16 MeV.

		$E_{scattered}$ (MeV)				E_{loss} (MeV)				E_{remain}(MeV)			
		1st sol. of:		2nd sol. of:		1st sol. of:		2nd sol. of:		1st sol. of:		2nd sol. of:	
strip	θ_{lab}(°)	^{3}He	^{4}He	^{3}He	^{4}He	^{3}He	^{4}He	^{3}He	^{4}He	^{3}He	^{4}He	^{3}He	^{4}He
1	16.38	16.64	16.89	0.30	1.51	2.6560	3.2826	0	1.1468	13.931	13.541		
2	17.54	16.38	16.51	0.30	1.54	2.6949	3.3473	0	1.1784	13.631	13.095		
3	18.70	16.09	16.09	0.31	1.58	2.7362	3.4253	0	1.2212	13.299	12.595		
4	19.86	15.79	15.66	0.31	1.63	2.7810	3.5170	0	1.2750	12.953	12.072		
5	21.02	15.48	15.20	0.32	1.68	2.8301	3.6107	0	1.3284	12.592	11.516		
6	22.18	15.15	14.72	0.33	1.73	2.8854	3.7179	0	1.3815	12.205	10.926		
7	23.34	14.81	14.21	0.33	1.79	2.9446	3.8432	0	1.4457	11.805	10.287		
8	24.50	14.45	13.68	0.34	1.87	3.0102	3.9886	0	1.5318	11.377	9.610		
9	25.66	14.08	13.10	0.35	1.95	3.0803	4.1617	0	1.6172	10.932	8.853		
10	26.82	13.70	12.52	0.36	2.04	3.1613	4.3517	0.01	1.7134	10.472	8.078		
11	27.98	13.30	11.90	0.37	2.14	3.2484	4.5834	0.01	1.8195	9.983	7.224		
12	29.14	12.89	11.25	0.38	2.27	3.3479	4.8720	0.01	1.9581	9.470	6.278		
13	30.30	12.47	10.56	0.39	2.41	3.4565	5.2358	0.01	2.1076	8.939	5.218		
14	31.46	12.05	9.83	0.41	2.59	3.5707	5.7305	0.01	2.2978	8.403	3.987		
15	32.62	11.61	9.04	0.42	2.82	3.7108	6.4941	0.02	2.5414	7.819	2.424		
16	33.78	11.17	8.17	0.44	3.12	3.8604	7.9947	0.02	2.8556	7.225	0.040		

Table T.3.6 Predicted energies (energy loss on ΔE detector and the remaining energy on E detector) for bombarding energy 20 MeV.

		$E_{scattered}$ (MeV)				E_{loss} (MeV)				E_{remain}(MeV)			
		1st sol. of:		2nd sol. of:		1st sol. of:		2nd sol. of:		1st sol. of:		2nd sol. of:	
strip	θ_{lab}(°)	^{3}He	^{4}He	^{3}He	^{4}He	^{3}He	^{4}He	^{3}He	^{4}He	^{3}He	^{4}He	^{3}He	^{4}He
1	16.38	19.43	19.83	0.57	2.29	2.3308	2.8614	0	1.8316	17.025	16.877		
2	17.54	19.10	19.33	0.58	2.35	2.3660	2.9277	0	1.8972	16.658	16.308		
3	18.70	18.73	18.80	0.59	2.41	2.4041	2.9965	0	1.9623	16.248	15.706		
4	19.86	18.35	18.24	0.61	2.49	2.4455	3.0726	0.01	2.0488	15.825	15.066		
5	21.02	17.96	17.65	0.62	2.57	2.4921	3.1670	0.01	2.1351	15.387	14.380		
6	22.18	17.54	17.02	0.64	2.67	2.5438	3.2685	0.02	2.2433	14.912	13.643		
7	23.34	17.11	16.35	0.65	2.77	2.5974	3.3844	0.02	2.3507	14.426	12.853		
8	24.50	16.66	15.64	0.67	2.90	2.6584	3.5311	0.02	2.4903	13.913	11.992		
9	25.66	16.19	14.91	0.69	3.04	2.7272	3.6851	0.03	2.6400	13.371	11.101		
10	26.82	15.70	14.10	0.71	3.21	2.8009	3.8855	0.04	2.8120	12.804	10.084		
11	27.98	15.20	13.27	0.73	3.42	2.8836	4.1266	0.04	3.0442	12.217	9.006		
12	29.14	14.68	12.36	0.76	3.67	2.9751	4.4270	0.06	3.3085	11.602	7.784		
13	30.30	14.15	11.36	0.79	3.99	3.0775	4.8479	0.07	3.6452	10.965	6.353		
14	31.46	13.59	10.23	0.82	4.43	3.1931	5.4836	0.09	4.1038	10.286	4.570		
15	32.62	13.03	8.81	0.86	5.14	3.3244	6.9119	0.11	4.8459	9.588	1.700		
16	33.78	12.46		0.90		3.4712		0.14		8.865			

Table T.3.7 Predicted energies (energy loss on ΔE detector and the remaining energy on E detector) for bombarding energy 25 MeV.

		$E_{scattered}$ (MeV)				E_{loss} (MeV)				E_{remain}(MeV)			
		1st sol. of:		2nd sol. of:		1st sol. of:		2nd sol. of:		1st sol. of:		2nd sol. of:	
strip	θ_{lab}(°)	^{3}He	^{4}He	^{3}He	^{4}He	^{3}He	^{4}He	^{3}He	^{4}He	^{3}He	^{4}He	^{3}He	^{4}He
1	16.38	23.03	23.60	1.01	3.39	2.0219	2.4703	0.70	3.22	20.976	21.090		
2	17.54	22.59	22.97	1.03	3.48	2.0532	2.5275	0.72	3.31	20.504	20.402		
3	18.70	22.14	22.26	1.05	3.60	2.0885	2.5919	0.74	3.44	20.018	19.626		
4	19.86	21.65	21.53	1.07	3.72	2.1274	2.6660	0.76	3.56	19.488	18.820		
5	21.02	21.14	20.75	1.10	3.86	2.1683	2.7516	0.79	3.70	18.936	17.953		
6	22.18	20.61	19.92	1.12	4.02	2.2162	2.8440	0.82	3.86	18.357	17.029		
7	23.34	20.05	19.02	1.16	4.21	2.2666	2.9636	0.86	4.06	17.746	16.007		
8	24.50	19.47	18.06	1.19	4.43	2.3229	3.0918	0.89	4.28	17.108	14.916		
9	25.66	18.86	17.04	1.23	4.69	2.3869	3.2571	0.93	4.55	16.433	13.728		
10	26.82	18.23	15.92	1.27	5.02	2.4548	3.4586	0.97	4.88	15.733	12.403		
11	27.98	17.58	14.70	1.32	5.45	2.5344	3.7196	1.03	5.32	15.002	10.917		
12	29.14	16.90	13.30	1.37	6.02	2.6196	4.0965	1.08	5.90	14.235	9.1344		
13	30.30	16.21	11.52	1.43	6.95	2.7181	4.7378	1.15	6.84	13.444	6.7042		
14	31.46	15.48		1.50		2.8288		1.22		12.601			
15	32.62	14.74		1.57		2.9555		1.30		11.732			
16	33.78	13.99		1.66		3.0996		1.39		10.834			

Table T.3.8 Predicted energies (energy loss on ΔE detector and the remaining energy on E detector) for bombarding energy 29 MeV.

		$E_{scattered}$ (MeV)				E_{loss} (MeV)				E_{remain}(MeV)			
		1st sol. of:		2nd sol. of:		1st sol. of:		2nd sol. of:		1st sol. of:		2nd sol. of:	
strip	$\theta_{lab}(^\circ)$	^{3}He	^{4}He	^{3}He	^{4}He	^{3}He	^{4}He	^{3}He	^{4}He	^{3}He	^{4}He	^{3}He	^{4}He
1	16.38	25.71	26.41	1.37	4.26	1.8481	2.2544	1.004	4.1136	23.833	24.119		
2	17.54	25.21	25.65	1.40	4.39	1.8782	2.3075	1.1432	4.2458	23.302	23.305		
3	18.70	24.66	24.83	1.42	4.53	1.9127	2.3707	1.1637	4.3883	22.717	22.421		
4	19.86	24.09	23.96	1.46	4.70	1.9483	2.4390	1.2062	4.5615	22.110	21.481		
5	21.02	23.51	23.02	1.49	4.89	1.9883	2.5230	1.2376	4.7554	21.489	20.455		
6	22.18	22.87	22.02	1.54	5.12	2.0330	2.6145	1.2908	4.9866	20.803	19.362		
7	23.34	22.22	20.94	1.58	5.38	2.0822	2.7310	1.3325	5.2499	20.103	18.163		
8	24.50	21.53	19.76	1.63	5.70	2.1368	2.8649	1.3851	5.5752	19.357	16.847		
9	25.66	20.82	18.50	1.69	6.09	2.1971	3.0298	1.4484	5.9696	18.586	15.419		
10	26.82	20.07	17.10	1.75	6.59	2.2649	3.2479	1.5115	6.4749	17.766	13.797		
11	27.98	19.31	15.47	1.82	7.28	2.3399	3.5531	1.5858	7.1714	16.930	11.856		
12	29.14	18.50	13.38	1.90	8.42	2.4249	4.0724	1.6697	7.4347	16.033	9.2389		0.88
13	30.30	17.69		1.98		2.5213		1.7531		15.124			
14	31.46	16.84		2.08		2.6278		1.8580		14.165			
15	32.62	15.94		2.20		2.7573		1.9839		13.133			
16	33.78	15.04		2.34		2.9041		2.1294		12.084			

E. Error calculation of differential cross section.

The differential cross section is given according to the formula:

$$\frac{d\sigma}{d\Omega} = \frac{N}{\Omega * \Phi * D_{hyd.}}$$

where

N represents the number of counts

Ω is the solid angle

$D_{hyd.}$ are the scattering centers of hydrogen

Φ is the flux of the beam

So the error of the differential cross section is given by the relation:

$$\Delta\left(\frac{d\sigma}{d\Omega}\right) = \sqrt{\left(\frac{\partial\left(\frac{d\sigma}{d\Omega}\right)}{\partial N} * \sigma_N\right)^2 + \left(\frac{\partial\left(\frac{d\sigma}{d\Omega}\right)}{\partial \Omega} * \sigma_\Omega\right)^2 + \left(\frac{\partial\left(\frac{d\sigma}{d\Omega}\right)}{\partial \Phi} * \sigma_\Phi\right)^2 + \left(\frac{\partial\left(\frac{d\sigma}{d\Omega}\right)}{\partial D_{hyd.}} * \sigma_{D_{hyd.}}\right)^2} \Rightarrow$$

$$\Delta\left(\frac{d\sigma}{d\Omega}\right) = \sqrt{\left(\frac{1}{\Omega * \Phi * D_{hyd.}} * \sigma_N\right)^2 + \left(-\frac{1}{\Omega^2} * \frac{N}{\Phi * D_{hyd.}} * \sigma_\Omega\right)^2 + \left(-\frac{1}{\Phi^2} * \frac{N}{\Omega * D_{hyd.}} * \sigma_\Phi\right)^2 + \left(-\frac{1}{D_{hyd.}^2} * \frac{N}{\Omega * \Phi} * \sigma_{D_{hyd.}}\right)^2} =$$

$$= \sqrt{\left(\frac{1}{\Omega * \Phi * D_{hyd.}} * \sigma_N\right)^2 + \left(\frac{1}{\Omega^2} * \frac{N}{\Phi * D_{hyd.}} * \sigma_\Omega\right)^2 + \left(\frac{1}{\Phi^2} * \frac{N}{\Omega * D_{hyd.}} * \sigma_\Phi\right)^2 + \left(\frac{1}{D_{hyd.}^2} * \frac{N}{\Omega * \Phi} * \sigma_{D_{hyd.}}\right)^2}$$

However, the statistical error, the error in the estimation of the thickness of the target and the error of the flux of the beam are:

$$\sigma_N = \sqrt{N},\ \sigma_D = 0.05 * D,\ \sigma_\Phi = 0.05 * \Phi$$

Therefore,

$$\Delta\left(\frac{d\sigma}{d\Omega}\right) = \sqrt{\left(\frac{\sqrt{N}}{\Omega * \Phi * D_{hyd.}}\right)^2 + \left(\frac{N}{\Omega^2 * \Phi * D_{hyd.}} * \sigma_\Omega\right)^2 + \left(\frac{1}{\Phi^2} * \frac{N}{\Omega * D_{hyd.}} * 0.05 * \Phi\right)^2 + \left(\frac{1}{D_{hyd.}^2} * \frac{N}{\Omega * \Phi} * 0.05 * D_{hyd.}\right)^2} =$$

$$= \sqrt{\frac{N}{\left(\Omega * \Phi * D_{hyd.}\right)^2} + \left(\frac{N}{\Omega^2 * \Phi * D_{hyd.}} * \sigma_\Omega\right)^2 + \left(\frac{0.05 * N}{\Omega * \Phi * D_{hyd.}}\right)^2 + \left(\frac{0.05 * N}{\Omega * \Phi * D_{hyd.}}\right)^2} =$$

$$= \sqrt{\frac{N}{\left(\Omega * \Phi * D_{hyd.}\right)^2} + \left(\frac{N}{\Omega^2 * \Phi * D_{hyd.}} * \sigma_\Omega\right)^2 + 2 * \left(\frac{0.05 * N}{\Omega * \Phi * D_{hyd.}}\right)^2} \Rightarrow$$

$$\Delta\left(\frac{d\sigma}{d\Omega}\right) = \sqrt{\frac{N}{\left(\Omega * \Phi * D_{hyd.}\right)^2} + \left(\frac{N}{\Omega^2 * \Phi * D_{hyd.}} * \sigma_\Omega\right)^2 + 2 * \left(\frac{0.05 * N}{\Omega * \Phi * D_{hyd.}}\right)^2}$$